國立交通大學

材料科學與工程學系

博士論文

合成核殼鉑釕奈米顆粒及官能基化碳載體提升甲醇電化學氧化性能

Enhancement of Methanol Electro-oxidation via Core-shell PtRu Nanoparticles and Functionalized Carbon Supports

研究生：謝育淇

指導教授：吳樸偉 教授
李志甫 博士

中華民國一零一年七月

National Chiao Tung University

Department of Materials Science and Engineering

Ph.D. Dissertation

合成核殼鉑釕奈米顆粒及官能基化碳載體
提升甲醇電化學氧化性能

Enhancement of Methanol Electro-oxidation via Core-shell PtRu Nanoparticles and Functionalized Carbon Supports

Student: Yu-Chi Hsieh

Advisors: Prof. Pu-Wei Wu
Dr. Jyh-Fu Lee

July, 2012

合成核殼鉑釕奈米顆粒及官能基化碳載體提升甲醇電化學氧化性能

研究生：謝育淇　　Student: Yu-Chi Hsieh

指導教授：吳樸偉 教授　　Advisor: Prof. Pu-Wei Wu

李志甫 博士　　Dr. Jyh-Fu Lee

國立交通大學

材料科學與工程博士學位

博士論文

A Dissertation
Submitted to Department of Materials Science and Engineering
College of Engineering
National Chiao Tung University
in partial Fulfillment of the Requirements
for the Degree of Doctor Philosophy
in
Materials Science and Engineering

July 2012

Hsinchu, Taiwan, Republic of China

中華民國一百零一年七月

合成核殼鉑釕奈米顆粒及官能基化碳載體提升甲醇電化學氧化性能

研究生：謝育淇　　　　　　　　　　指導教授：吳樸偉 教授

李志甫 博士

國立交通大學

材料科學與工程學系

摘要

本研究探討提升電化學甲醇氧化之方法，分別從製備雙元 PtRu 核殼奈米顆粒觸媒及觸媒之碳載體官能基化著手，旨在開發更廉價耐用之直接甲醇燃料電池陽極觸媒。首先，採用脈衝式定電流電鍍不同大小和組成之鉑釕奈米合金顆粒在 XC-72R 碳載體上。脈衝式電鍍的結果顯示鉑釕合金的比例隨著脈衝式電鍍周期 (Duty Cycle) 有規律趨勢變化。藉由 XRD、TEM、ICP-MS 證明 PtRu(鉑釕)材料特性。利用循環伏安法(CV)和 Pt 金屬對氫離子吸脫附，鑑定 PtRu NPs 甲醇氧化的電化學行為。由 XPS 的結果分析得知 Ru 金屬的氧化態，可以推測出 Pt 及 Ru 有置換反應發生:脈衝式電鍍中，Ru 金屬在電流通入的時段(T_{on})有沉積在基材上，在電流停止的時間內(T_{off})則被溶解;在 T_{on} 及 T_{off} 的時間內， Pt 金屬則持續沉積。為了進一步了解置換反應的反應機制，利用 X 光吸收光譜(XAS)探討由碳材所支撐的 Ru(釕)奈米粒子，浸泡在不同 pH 環境下的 H_2PtCl_6(氯鉑酸)水溶液中時，Pt(鉑)離子與 Ru 金屬奈米粒子的置換反應機制，並且形成雙元合金 Pt 為殼層、Ru 為核心的奈米核殼結構。XAS 結果顯示，Pt 離子在不同 pH 環境下的擁有不同配位體種類及數量，這會影響 Pt 離子活性，進一步地決定奈米粒子殼層上 Ru 和 Pt 比例多寡與觸媒活性。電化學結果顯示在 pH=1 的 H_2PtCl_6 水溶液中所形成的雙合金核殼奈米粒子具有較低移除 CO 的電位以及穩定氧化 H_2 的催化效果，而在 pH=8 下，並沒有預期的表面雙合金產生，且奈米粒子有較差的 CO 移除以及氧化 H_2 的特性。最後在碳載體上，經由在含氧硫酸中 CV 掃描處理可破壞 Nafion ionomer 以快速製作含氧官

能基在碳載體表面上。離子色譜法測量經由 CV 掃描後硫酸根離子的殘留含量。拉曼分析結果顯示碳材結構在 CV 掃描處理後只有微量的改變，證明碳材未經破壞。XPS survey 分析結果也顯示出氟原子的成分比減少，是由於 Nafion 的降解所造成的原因，同時氧原子成份比也相對增加，官能基化電極相對於浸泡組電極，可增加 170%的鉑離子吸附含量。藉由 XRD、TEM、ICP-MS 證明 Pt 材料特性，並藉由電化學甲醇氧化行為證明了 Nafion 含氧官能基也可以有效地協助 Pt 氧化甲醇的能力。

Enhancement of Methanol Electro-oxidation via Core-shell PtRu Nanoparticles and Functionalized Carbon Supports

Student: Yu-Chi Hsieh
Advisors: Prof. Pu-Wei Wu
Dr. Jyh Fu Lee

Department of Materials Science and Engineering
National Chiao Tung University

Abstract

The objective for this research is to improve methanol electro-oxidation in direct methanol fuel cells via fabricating core-shell PtRu nanoparticles and functionalizing carbon supports simultaneously. First, galvanostatic deposition in rectangular pulses is employed to prepare PtRu nanoparticles on carbon cloths in various sizes and compositions. By adjusting duty cycle, we are able to control the surface composition of PtRu effectively. Material characterizations including XRD, TEM, XPS, and ICP-MS, as well as electrochemical analysis such as cyclic voltammetry and hydrogen desorption are carried out. We found that in a displacement reaction which Ru atoms are alternately deposited and dissolved during Ton and Toff, while Pt atoms are continuously deposited. To further investigate the extent of displacement reaction, we adopt XAS to explore the oxidation state and neighboring atoms for Pt and Ru in samples produced by immersing carbon-supported Ru nanoparticles in hexachloroplatinic acid solutions with pH of 1, 2.2 and 8, respectively. Spectra from XAS confirm that the pH value of hexachloroplatinic acidic solution determines the type of ligands complexing the Pt cations, and consequently affects the extent of displacement reaction and alloying degree of core-shell (Ru@Pt) nanoparticles. As a result, the samples from pH=1 bath reveal a desirable core-shell structure that displays a reduced onset potential in CO stripping and stable catalytic performance for the H_2 oxidation reaction, while the samples from pH=8 bath indicate formation of Pt clusters on the Ru surface that leads to poor CO stripping and lower H_2 oxidation performance. Lastly, we develop a facile electrochemical route to generate functional groups on the carbon surface via engaging the degradation of Nafion ionomer by multiple CV sweeps in oxygen-saturated H_2SO_4 electrolyte. Ion chromatography confirms the dissolution of sulfate anions upon CV scans. Raman analysis suggests a minor modification to carbon structure. XPS indicates a significant increase of oxygenated functional groups in conjunction with notable reduction in the fluorine content. The amount of the oxygenated functional groups is determined by curve-fitting of C1s spectra with known constituents. The functionalized electrode allows a 170% increment of Pt ion adsorption compared to that without functionalization. After electrochemical reductions, the functionalized electrode reveals significant improvements in electrocatalytic performance in methanol oxidation, which is attributed to the oxygenated functional groups that facilitate the oxidation of CO on Pt.

致謝

人生的際遇總是難以莫測，原以為完成碩士學位後，應不會再在學術殿堂裡追逐。在服兵役期間，站哨時、與同僚聊天時，滿腦子都是科學，發現自己還是熱衷于科學。因此，攻讀博士學位的緣由是單純熱愛科學的心與夢想。但若沒有上帝巧妙的安排，與主的帶領，我想我也不會順利進入這學術殿堂。感謝耶和華與主耶穌讓我經歷這豐富的人生過程。

首先感謝我的博士班指導教授們——吳樸偉教授與李志甫博士。在學術專業、人生路途、人際關係、生活處事上，您們有如學生的父親與兄長一般教導我，在這五年讓學生成長與成熟許多。首先我非常榮幸在吳樸偉老師的團隊下作研究，在研究路途上您給予學生很大的自由度，讓我盡情地享受我的科學夢，並且在關鍵時刻給予學生正確的方向與想法。您對學術的嚴謹態度、開放式的思考、邏輯性的推測還有學術道德的嚴格要求，都是學生在博士期間收穫最多的智慧。您的美式教學風格也常鼓勵學生們多接觸國際會議。在您的鼓勵下，學生有機會多次參加國際會議。2008 年在夏威夷電化學會議，學生有機會認識並接觸布魯克海文國家實驗室的 Dr. Adzic ，因此埋下在美國進修一年的種子。2010 年在拉斯維加斯電化學會議，學生更進一步地與 Dr. Jia X. Wang 討論在美國進修一年的計畫。2011 年學生在您的推薦下前往美國布魯克海文國家實驗室進修一年，在專業知識上學生收穫良多，都是老師您的功勞。求學期間與吳老師英文信件來往，老師您都是字句用心地教導學生的英文成為字字珠璣、優美的英文文章。在生活上，老師您也常常教導學生，不論是學術職業倫理上的關係應答，人際關係的進退還是豐富的生活經驗教導，都讓學生在人生和人格上更加成熟茁壯。同時也非常感謝我另一位指導教授，李志甫博士。您的帶領和教導，讓學生學習到專業的 X 光吸收光譜技術，並從中獲得許多科學啟發，因此在專業上使學生連續獲得兩屆同步輻中心的博士生培育計畫獎學金。李老師您對實驗的嚴謹態度與對分析數據的精準要求，讓學生在實際實驗上受益良多，因此在成果上使學生在同步輻射年會中連續兩屆獲得學生組的佳作。最後感謝李老師的寬宏大量，因學生的粗心常在實驗室與實驗站上搞得一團糟。古人說[一日為師，終生為父]，吳教授與李博士您們的教導，令學生受益一生，學生畢生難忘。

一起奮鬥的實驗夥伴們，感謝你們。最年長的張玉塵學長與周兆玲學姊，感謝你們提供了不少中科院的資源。尤其是疏水性碳布，只有中科院生產，實驗上的需求都靠你們了。謝謝你們常常帶我參觀中科院的環境生活，讓我認識了中華民國軍事研究最高單位的生活。回想起玉塵學長買的股票漲時，那一天就有免費的中餐，真是懷念啊。林勝結大哥與謝逸凡大哥，實驗室有你們這兩大支柱撐著，才可讓小弟我在實驗室胡搞瞎搞。感謝勝結大哥解決我生活上的許多疑難雜症，在新竹生活有任何問題找你就對啦!感謝逸凡大哥樂活的心態，讓我學習如何排解和舒緩壓力。逸凡大哥你總是帶著微笑面對事情，從你臉上沒有看到過憂愁，這正是我學習的地方。實驗室超級戰將黃苡叡學長與張雲閔學長，能認識你們是我的榮幸。你們對科學與工程的熱情，總是鼓勵著我，並且在不同的角度審查我們彼此的研究。感謝苡

叡學長你總是用工業界的角度與環境觀看並提醒我，學術必須要學以致用。至於張雲閔學長，我跟你的恩怨最長久了，在博士期間除了老師以外，我跟你生活共事最久，所以整個恩恩怨怨可以再寫個博士論文了，我想這就是同袍情誼。感謝你在 TEM 上熱情的幫忙；感謝你在學術研究上與我彼此激烈的爭辯討論，讓我們倆可以認真思考並維持自己的觀點；感謝你讓我知道學術並不是自己爽就好，總是會有不一樣的聲音；感謝你在生活上與研究上總是對我有個照應。實驗室老大陳境妤，感謝你細心負責實驗室的大小事務，以致於我這常常不負責公共事務的學長可以開心的作研究。你身上一步步扎實的學習與做事態度，讓我學習到按部就班，認真學習，就沒有學不會的地方。感謝你在拉曼、IR 光譜、XRD 儀器上的協助。感性的廖晨宏，從你專題生，一路看著你到現在都已博二了。看著你成長真是欣慰，感謝你全力以赴認真完成我們的實驗。感謝姚奕全在 HR-TEM 上熱情的協助。感謝王仁君，時常在新竹陪我聊天吃飯的對象，聽我訴說心中的苦悶。感謝詹丁山博士在 BL01C1 XAS 實驗上的熱情協助與教學。感謝包志文博士在 BL17C1 XAS 實驗上的熱情協助與教學。感謝謝承安與陳姿亘在 XAS 實作與分析軟體上的教學。感謝陳重守在 XPS 儀器上的幫忙。感謝陳偉達在美國一起共患難的支援和鼓勵。感謝劉怡玲在離子分析儀上的協助。許多細節未提到的學長同學們，蔣國章、車牧龍、彭俊彥、章詠湟、張修誠等等在此一起感謝。

碩士班學弟妹們，有了你們我的生活才精彩。首先感謝張立忠，在我博士最艱苦的時間出現，是個強而有力的夥伴。感謝你超強的英文能力，幫助我完成了許多任務。感謝你，我們一起完成了我博士論文中重要的一篇研究。你讓我知道宅男，也可以是很有品味的。接下來感謝郭哲瑋，在我在美國的期間，幫我完成在台灣的任務。謝謝你在美工上的幫助。感謝你任勞任怨地完成計畫的工作與研究。感謝你，讓我知道出國旅遊，可以很簡單的。感謝李依叡與陳詠民在研究計畫上，認真付出。感謝呂永錚在釕（Ru）前驅物上給我專業的建議。感謝邱于凡、蔡佳芬在專題研究上認真的學習與貢獻。感謝一起奮鬥畢業過程的學弟們，許議文、李孟翰、邱尊偉。感謝三位出國進修博士的優秀學弟蔡合成、賴俊翰、陸意德。蔡合成感謝你與我一起奮鬥博士資格考試的階段。感謝你願意與我分享你的生活與情感部份。賴俊翰感謝你，實驗室有你的地方就充滿了歡樂。陸意德感謝你，讓我看到一位熱愛書本到會忘了睡覺的人，也感謝你在 EQCM 上的協助。感謝葉耕余和李佳勳，在研究與友誼上熱情的相挺。感謝陳國豐，提供許多台積電專業的知識。實驗室的眾多學弟妹們，黃柏翰、林韋霖、林建程、梁雁汝、陳欣儀、傅宥閔、黃冠傑、陳琪、陳婉瑩、周亮余、黃筱琳、邱于凡、王儷曄、陳儷尹(大小粒魚丸)、陳致源、張詠策、梁茹夢、張濴方、陳柏均、張庭瑜、賴欣君、蔡致芳、林映眉、羅世儒等人，我在此感謝你們，博士班的生活有你們真好。

在美國精彩豐富的生活。首先感謝 Dr. Jia X. Wang 擔任我在美國的指導教授。Jia 在您的帶領下，讓我學習到專業的電化學知識，及要有遠見的目標與培養深厚專業知識的能力。更重要的是，你在繁忙工作的同時，又能兼顧好家庭生活，也讓我學習到對時間的有效管理。真的是非常感謝你，讓我有機會前往美國進修一年，見識到廣闊的世界。我也非常感謝 Dr. Radoslav Adzic，讓我加入您的團隊，從而接觸到頂尖優秀的人才。您的智慧是個百寶庫，遇到問題總是有答案與很多想法。雖然您已年邁七十，您對科學的求知慾與新鮮感猶如年輕人

一般。您溫和和藹的態度，讓我學習到作爲一位領導者的風範。我也非常感謝廖世軍教授，您待我如您兒子一般的照顧。您樂觀的態度、認真學習的精神，都是值得我學習的地方。我也非常喜歡和你聊有關中國的事務。感謝孟祥波博士，您也待我如您弟弟一般的照顧。謝謝您常鼓勵我要努力向上，鼓勵我快成家。謝謝您，我會努力盡快達成你的願望。感謝 Wei-Fu Chen 和 Chloe Wang 夫婦，讓我感受到，我人在美國也可以享受到台灣家庭的生活，謝謝你們的盛情款待與生活上的幫忙。感謝 Yun Cai, 在 Cu UPD 技術上的教學,還有生活上的協助，也很懷念你的美食。感謝楊莉君，一起在美國實習研究一年，並且互相鼓勵，一起遊玩的日子。感謝 YongMan Choi, 經常的鼓勵我，並相信主。感謝 Kotaro Sasaki，在 In-site XAS 上專業的教學。感謝 Miomir 和 Stoyan, 在實驗室安全細節上的教導。還有一群未提起的朋友們，謝謝你們讓我在美國的生活很精彩。

家庭是最後的堡壘。最感激的就是我的家人，阿嬤、爸爸、媽媽、翠菱、育婷，女友張宇。阿嬤您最疼我了，常常塞零用錢給我，謝謝您貼心的照顧，當孫子總是幸福的。爸，從念博士的第一天，您就告誡我說[不要整天待實驗室，要多出去追女孩子]。我知道我會努力完成您的願望，趕快娶妻生兒，謝謝您讓我知道家庭是最重要的。媽，謝謝您不論我發生什麼事，您總是最挺我的。謝謝您辛勞地為家裡的大小事務付出。翠菱，謝謝你平時細心地陪伴家人，使我可以從你身上獲得家人的需求。育婷，感謝你平時提供的一些潮流物品，讓我可以放鬆心情。你未來也好好努力加油!最後感謝我的女友張宇，謝謝你在我最後關鍵煎熬的日子裡，一直陪在我身旁，還經常鼓勵我，並相信我的能力。

感謝主!我相信這一切都是主的安排。

Table of Contents

List of Tables

List of Figures

Chapter 1 Introduction

1.1 Background

Fuel cells are of considerable interests as alternative energy-generating systems for sustainable future with reduced emission. To render the fuel cells commercially viable, it is necessary to reduce system cost and operation life time simultaneously[1, 2]. Unfortunately, conventional electrocatalysts are primarily based on precious metals and they tend to aggregate or break off during cell operations. Therefore, one particular aspect to overcome these obstacles is to fabricate electrocatalysts in desirable core-shell structures with reduced particle size, and establish uniform dispersion and solid anchoring onto suitable carbonaceous supports. In a core-shell arrangement, the inexpensive element can constitute the core while the expensive one can reside on the surface instead. In such way, the electrocatalytic activity for the shell element remains intact but the catalyst cost is expected to be reduced substantially[3-5]. Alternatively, it is suggested that the carbon surface can be deliberately functionalized so the anchoring sites for depositing ions can be increased, leading to larger catalyst loading and stronger bonding between the carbon support and active metal[6]. It is surmised that interaction like this could relieve catalyst loss or aggregation.

Among many materials investigated for fuel cell applications, the development of bimetallic PtRu nanoparticles has attracted substantial attention recently because the PtRu is not only an effective electrocatalyst for methanol oxidation reaction in direct methanol fuel cells (DMFCs) but also demonstrates impressive CO oxidation ability for reformate hydrogen fuel cells[7, 8]. In DMFCs, methanol electro-oxidation entails consecutive removal of hydrogen that leaves a CO strongly bonded to the Pt, resulting in a gradual loss of catalytic activity known as CO poisoning. For the reformate hydrogen fuel cells, there is often minute presence of residual CO in the hydrogen feeds so it becomes a concern once the Pt is employed for hydrogen oxidation at the anode. To alleviate the CO poisoning effect, the Ru is purposely alloyed with Pt because the Ru can either provide the oxygenated species for CO oxidation to CO_2 (known as bifunctional model) or alter the electronic structure of Pt so the CO-Pt bond is weakened significantly (known as ligand effect)[3, 9, 10].

To prepare PtRu nanoparticle, it is established that the electrochemical pulse electroplating method allows interrupted time for mass transport so better control over composition and morphology is possible over conventional galvanostatic or potentiostatic counterparts. For example, Tsai et al. (蔡春鴻教授) has employed the pulse deposition, with the addition of chemical additives, to prepare fine PtRu on carbon nanotube surface for enhanced catalytic actions[11]. In general, many electrochemical variables can be adjusted to attain desirable deposit properties (See Fig. 1.1 as follows). However, one of the drawbacks is that there are nucleation and growth occurring in each pulse so the deposits are known to reveal a wide size distribution of particle sizes. In addition, for PtRu the replenishment of individual cations depends on their respective concentrations and diffusion coefficients. As a result, this is likely to produce unnecessary variation in deposit composition in each pulse.

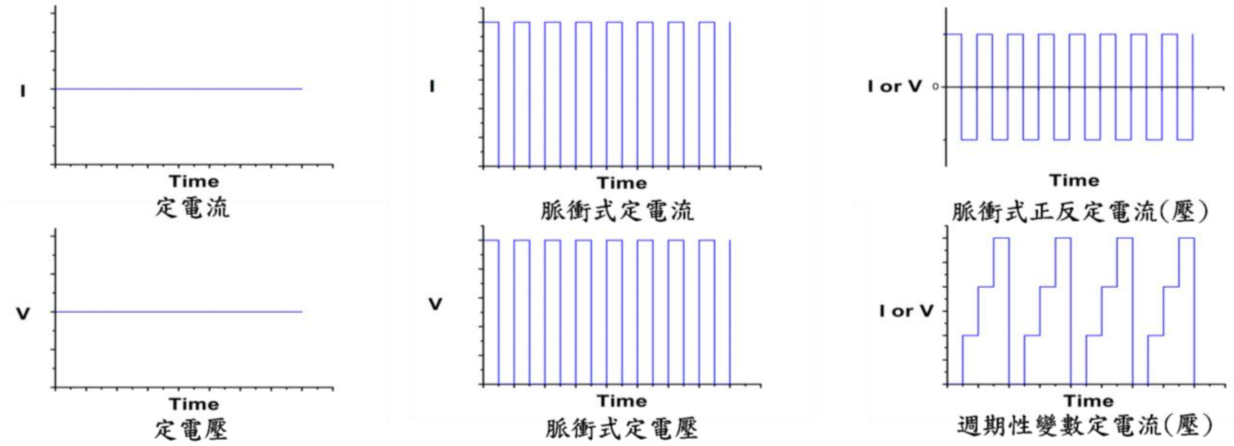

Figure 1.1 Possible operation modes for electrodeposition.

Recently, X-ray absorption spectroscopy (XAS) has been established as a powerful tool to elucidate the detailed arrangement for Pt and Ru in nanoparticulate forms[12, 13]. It is because with light source from NSRRC (National Synchrotron Radiation Research Center), any minute variation in the absorption coefficient can be diagnosed. For example, spectra of XANES (X-ray Absorption Near Edge Structure Spectroscopy) and EXAFS (Extended X-ray Absorption Fine Structure) are routinely used to determine the oxidation state, fractional d-electron density, atomic environment of the absorbing atom, as well as its short-range ordering and geometric arrangement. In this regard, with XAS, we can follow the formation mechanism of PtRu nanoparticles and analyze Pt and Ru for both deposit and solution states. Moreover, recent studies have adopted the in-situ XAS to characterize the surface rearrangement in PtRu nanoparticles during fuel cell operation (under polarizations) so better understanding over life time performance can be established[14, 15].

Another important factor affecting the performance of electrocatalysts is the catalyst supports. Amount many conductive materials, carbonaceous materials have been widely employed as the substrates for catalyst impregnations in room tempeaturare fuel cells[11, 16, 17]. It has been found that nanoparticulate PtRu are able to distribute uniformly, leading to reduced loading and better catalyst utilization[6]. Untreated carbon is usually hydrophobic that allows poor adsorption of catalyst precursors and active metals. After proper surface functionalizations to render a hydrophilic surface, the carbon is expected to adsorb more catalyst precursors for a larger amount of catalyst deposition. In literature, carbon functionalization involves anodization treatments in corrosive acids at moderate temperature. For example, Kangasniemi et al. imposed potentiostatic treatments on Vulcan XC72 (XC72) in 1 M H_2SO_4 solution, and observed a signficant oxidation for the anodizing voltage of 1.2 V for 16 h. The degree of surface functionalization also depends on the type of carbon because its surface area and microstructure differ considerably. After functionalization, surface oxidized groups such as phenols, carbonyls, carboxylic acids, ethers, quinones, and lactones have been identified[17]. The exact mechanism responsible for the formation of selective functional groups is contingent on the processing steps employed and the type of carbon.

Another route to functionalize carbons is via the chemical changes of polymeric binders. In electrode fabrications, Nafion ionomer is often added in mixture with carbon, serving not only as a binder but also conductive channels for proton transports. Therefore, it is expected that the Nafion ionomer would suffer from structural alteration and loss of sulfonic acid side chains if deliberate electrochemical treatments are imposed. Previously, extensive efforts have been devoted to understand the responsible mechanism for Nafion membrane degradation in different environments and factors including humidity, temperature, and oxygen concentration are found to be critical[18, 19]. According to Bruijn et al., hydroxyl (‧ OH) and peroxy (‧ OOH) radicals formed during fuel cell operations are able to attack polymer end groups that still contain residual terminal H-groups[20]. Further studies also indicate that the sulfonic acid side groups are more susceptible to radical attacks than poly(tetrafluoroethylene) backbone[21]. The broken species of Nafion ionomer contain free radicals that attach to the carbon which catalyze further carbon oxidation[22]. Presence of functionalized groups has been established to catalyze additional oxidized groups. Therefore, we realize that the intentional degradation of Nafion ionomer provides a facile route for carbon support functionalization. Fig. 1.2 depicts a schematic showing the formation of functionalized groups and adsorption of selective cations.

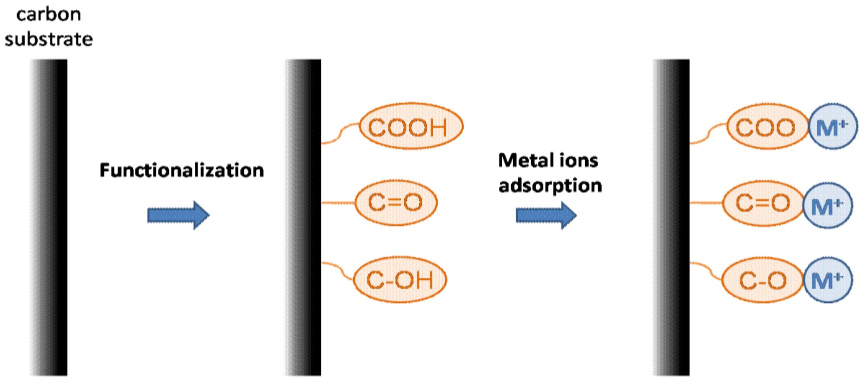

Figure 1.2 A schematic demonstration for the functional group formation and physical adsorption of selective cations.

An alternative route to manipulate the surface composition of PtRu is to take advantage of the displacement reaction. The displacement reaction is also known as redox-transmetallation reaction or spontaneous deposition, and it often occurs in multi-component systems with constituents revealing distinct values of redox potentials[23, 24]. In principle, when a binary deposit is in contact with their respective cations in electrolyte, the constituent of lower redox potential is dissolved from the deposit while the one with a higher redox potential is reduced from the electrolyte. Consequently, the deposit on the surface can be tailored for a desirable makeup which is different from that of bulk if the displacement reaction is carefully controlled. For PtRu, once the Ru is immersed in the electrolyte containing Pt cations, the Ru would undergo an oxidation reaction in conjunction with the reduction of Pt cations. Previously, Adzic et al. and Huang et al. **(黃炳照教授)** have adopted the displacement reaction to tailor core-shell nanoparticles with impressive results[12, 25].

1.2 Motivation

In this study, I attempt to prepare desirable PtRu core-shell nanoparticles for improved catalytic behaviors. In addition, I explore the functionalization of catalyst support in order to obtain a better life time performance. To realize the core-shell structured PtRu nanoparticles, I adopt galvanostatic pulse deposition. The surface composition of PtRu nanoparticles is controlled via the displacement reaction. To prolong life time activity, I carry out functionalization treatment to anchor electrocatalysts on the carbon support. In Chapter 2, more literature reviews are provided so that readers can be acquainted with our work.

Chapter 2 Literature Review

2.1 Anode electrocatalysts for direct methanol fuel cell

Fuel cells using hydrogen or methanol as fuels and oxygen or air as oxidants convert chemical energy in the fuels directly into useable electrical energy, and thus they are suitable as power sources for automobiles and portable electronics. In particular, using fuel cells in electric vehicles has been considered as a promising route to reduce energy consumption since they can generate electricity in a cleaner and more efficient way as compared to conventional gasoline-based engines. To date, there are many fuel cell systems competing for commercial viability. Among them, the direct methanol fuel cell (DMFC) has been studied extensively because of its simple fuel usage and feed strategies[26, 27] Comparing to hydrogen gas for other fuel cell systems, the DMFC uses methanol as the feedstock. Methanol is liquid and easy to be handled, stored, and transported. In addition, methanol is renewable and is of high energy density. Therefore using methanol as the fuel can simplify the entire fuel cell system.

So far, the most popular electrocatalyst for methanol electro-oxidation is Pt and its alloys. Methanol oxidation reaction (MOR) on the Pt metal involves several reaction steps including (1) methanol adsorption; (2) C-H bond activation (methanol dissociation); (3) water adsorption; (4) water activation; and (5) CO oxidation[28]. Previously, the detailed MOR mechanisms on the Pt have been investigated by in-situ Fourier transform infrared spectroscopy (FTIR) and electrochemical quartz crystal microbalance (EQCM)[29, 30], and they are discussed below at different potential regimes.

Electrochemical mechanism for the methanol oxidation reaction (MOR) on platinum (Pt) metal is composed of series of reaction steps including (1) methanol adsorption; (2) C-H bond activation (methanol dissociation); (3) water adsorption; (4) water activation; and (5) CO oxidation [28]. The detailed MOR mechanisms on Pt have been investigated by in situ Fourier transform infrared spectroscopy (FTIR) and electrochemical quartz crystal microbalance (EQCM)[29, 30] in different potential regions, explained as follows.

1) At potential region around 0.05V:

Methanol molecules dissociate and adsorb on the Pt surface by dehydrogenation and the subsequent formation of formyl (-CHO) and CO, as shown in Equation (2.1-2.2) and Figure 2.1.

$$4Pt + CH_3OH \rightarrow Pt\text{-}CHO + 3Pt\text{-}H \qquad (2.1)$$

$$Pt\text{-}CHO + Pt \rightarrow Pt\text{-}CO + Pt\text{-}H \qquad (2.2)$$

2) At potential region around 0.05V-0.2V:

The intermediate CO at Pt sites and the adsorbed H_2O molecules form formic acid $(HCOOH)_2$, as shown in Equation (2.3) and Figure 2.1.

$$2Pt\text{-}CO + 2Pt\text{-}OH_2 \rightarrow Pt_2\text{-}(HCOOH)_2 + 2Pt \qquad (2.3)$$

3) At potential region around 0.2V-0.6V:

$(HCOOH)_2$ is oxidized via two pathways as shown in Equation (2.4-2.5) and Figure 2.1

$$Pt_2\text{-}(HCOOH)_2 \rightarrow Pt\text{-}(CO_2) + Pt\text{-}COOH + 3H^+ + 3e^- \qquad (2.4)$$

$$Pt_2\text{-}(HCOOH)_2 \rightarrow 2Pt\text{-}(CO_2) + 4H^+ + 4e^- \qquad (2.5)$$

4) At high potential region (over 0.6V):

The adsorbed H_2O molecules on the Pt surface form the surface oxide Pt-OH, and consequently, the CO can be oxidized to CO_2 via the reaction between Pt-OH and Pt-CO, as shown in Equation (2.6-2.7) and Figure 2.1

$$Pt\text{-}OH_2 \rightarrow Pt\text{-}OH + H^+ + e^- \qquad (2.6)$$

$$Pt\text{-}CO + Pt\text{-}OH \rightarrow Pt\text{-}(CO_2) + Pt + H^+ + e^- \qquad (2.7)$$

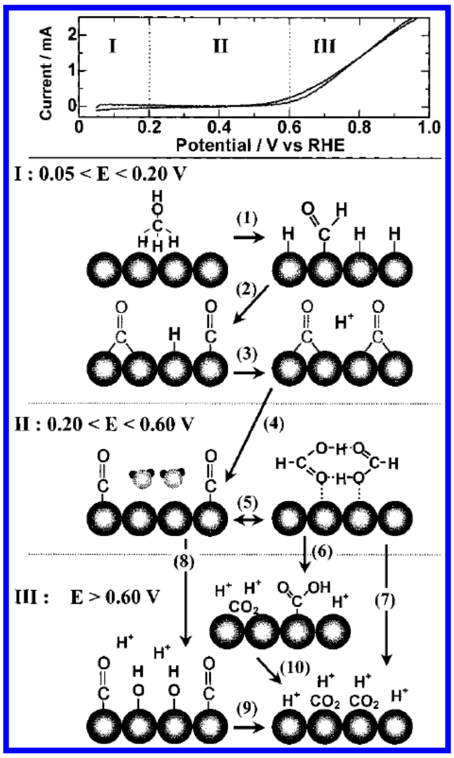

Figure 2.1 Schematic illustration of methanol oxidation on Pt surface in different potential regions, studied by FTIR and attenuated total reflection (ATR)[30].

From the above discussion of MOR mechanism on the Pt surface, we note that the Pt surface can form sufficient bonding with the adsorbed CO. However, the CO is difficult to desorb once it occupies the Pt surface. Therefore one rational solution is to add second or even third elements into the system for the purpose of promoting the oxidation of Pt-CO to Pt-CO_2. To suit this function, the PtRu catalyst is well known as a promising DMFC catalyst because it can easily remove CO from the Pt sites. The function of Ru can be explained by two mechanisms[31-43].

1) Bifunctional effect

In an aqueous solution, the H_2O molecules can adsorb onto the Ru surface and form Ru-OH at low potentials. And the CO adsorbed on neighboring Pt sites can be oxidatively removed by the reaction between Ru-OH and Pt-CO. Alloying Ru with Pt is able to increase the CO tolerance. The detailed reaction mechanisms are shown in Figure 2.2.

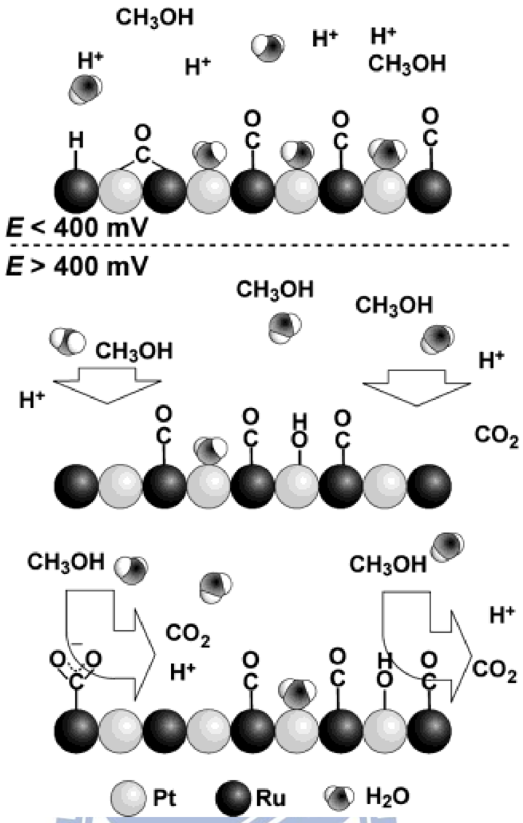

Figure 2.2 Schematic illustration of methanol oxidation on PtRu surface in different potential regions, studied by FTIR and ATR[44].

2) Ligand effect (electronic effect)

The second element added to the Pt-based catalysts will directly or indirectly modify the electronic structure of Pt, decrease the adsorption ability of CO on Pt, and consequently enhance the performance toward the MOR[45].

Usually the variables affecting the activities of PtRu electrocatalysts include particle size, the dispersion of nanoparticles on carbon supports, and etc. By further study of the atomic structure in bimetallic PtRu nanoparticles, it is found that different nanostructures such as core-shell structures or perfect alloying ones impose significant effects on the electrochemical behaviors of PtRu catalysts for the MOR[9, 37, 38, 42, 43, 46]. For example, Selim et al.[3] proposed that the in H_2 atmosphere with 1000 ppm CO, the effective CO oxidation to CO_2 can be catalyzed at 30 °C by

Ru@Pt core -shell nanostructured catalyst, which is superior as compared to 85 ℃ by commercial PtRu alloy nanocatalyst, at 93 ℃ by monometallic mixtures of Pt and Ru nanoparticles, and at 170 ℃ by pure Pt nanoparticles. Figure 2.3 illustrates the structures of these nanoparticles.

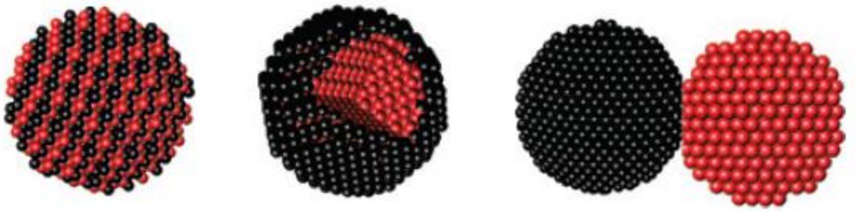

PtRu alloy Ru@Pt core-shell Linked monometallic nanoparticles

Figure 2.3 illustration structures of PtRu alloy, Ru@Pt core-shell, monometallic nanoparticles[3].

Huang et al. **(黃炳照教授)**[9, 25, 47]. have also studied the structural impact of PtRu catalysts on the anodic MOR currents by X-ray absorption spectroscopy (XAS). They found out that the MOR performances were enhanced with the increased P_{Ru} values.

$$P_{Ru} = N_{Ru-Pt}/(N_{Ru-Pt} + N_{Ru-Ru})$$

The P_{Ru} value represents the possibility of forming a heterostructure for Ru atoms with Pt atoms. The increased P_{Ru} suggests the increased N_{Ru-Pt} and the decreased N_{Ru-Ru}, and the more profound bifunctional effect of PtRu. And therefore the PtRu heterostructure can promote the performance toward MOR.

2.2 Platinum monolayer core-shell electrocatalysts

Further decreasing the Pt amount and enhancing the Pt utilization remain to be one major goal for the development of noble-metal-based catalysts in recent years. The Pt monolayer electrocatalysts developed by R.R. Adzic's group provide the ultra-low Pt content, the highest Pt utilization, and impressive activity[12, 48]. The Pt monolayer is prepared via a technique involving copper underpotential deposition (Cu UPD).

Cu UPD deposits one monolayer of copper on different electrically conductive substrates with higher reduction potentials than that of Cu. It entails the chemisorptions of copper atoms on the substrate at the underpotential with respect to the potential for Cu bulk deposition which occurs at a more positive potential than the thermodynamic potential for Cu deposition in the electrolytes. UPD is a surface-limited monolayer-deposition process and it can be performed with or without the coadsorption of anions in the electrolytes. Take the formation of Cu monolayer on Au (111) single crystal surface as an example[49, 50], there are two Cu UPD peaks on the Au (111) in $CuSO_4$ electrolyte (Fig. 2.4). After the first UPD peak around 0.2 V (vs. SCE) (Fig. 2.4), the commensurate $(\sqrt{3}\times\sqrt{3})R30^\circ$ Cu adlayer occupying the 3-fold hollow sites on Au (111) is formed with the coadsorption of Cu^{2+} cations and SO_4^{2-} anions, as shown in Fig. 2.5. In Fig. 2.5, the lowest layer is the Au (111) substrate, the middle layer is the Cu adlayer, and the top layer is the coadsorbed SO_4^{2-} anion overlayer. With additional UPD after the second UPD twin-peak around 0.05 V (vs. SCE) (Fig. 2.4), the Cu monolayer, i.e. the Cu-(1×1) structure is formed on Au (111), as shown in Fig. 2.6. The coadsobed SO_4^{2-} anions adopt an unchanged $(\sqrt{3}\times\sqrt{3})R30^\circ$ arrangement forming an overlayer on top of the two Cu adlayers with different arrangements. By controlling the potential, a complete Cu monolayer can be formed on the substrate.

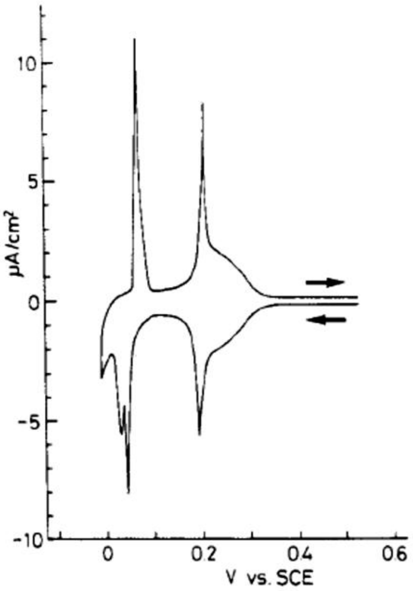

Figure 2.4 Cyclic voltammogram for the Au (111) single crystal electrode in 1 mM $CuSO_4$ with 0.05 M H_2SO_4. The sweep rate was 1 mV/s [49].

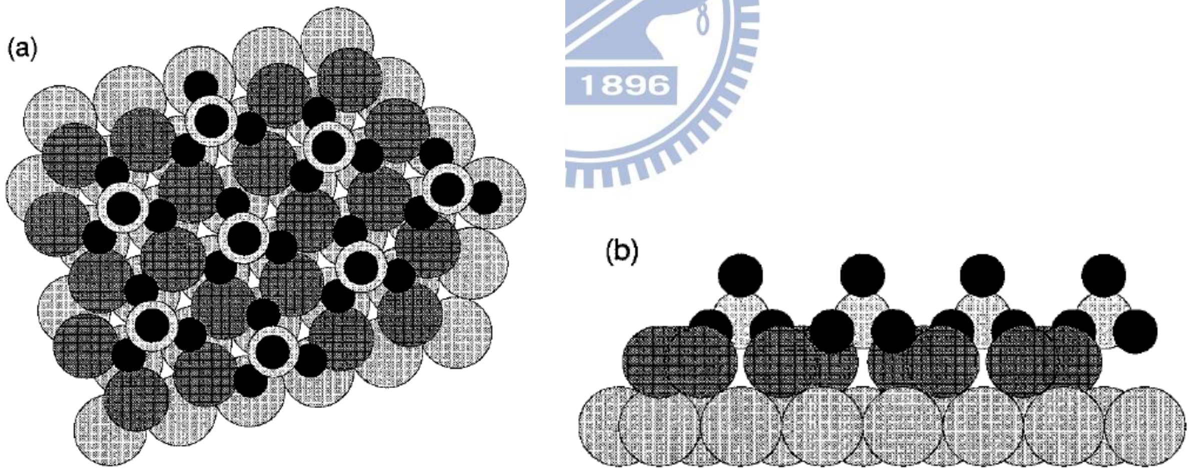

Figure 2.5 Interfacial structure of the Cu UPD on Au (111) single crystal surface after the first UPD peak[49]: (a) top view (b) side view.

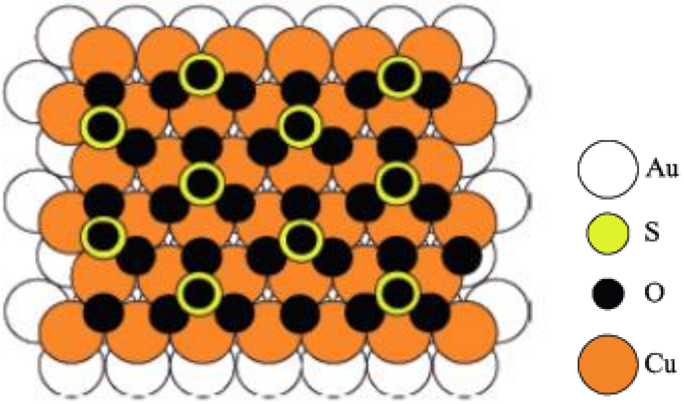

Figure 2.6 The top view of the Cu-(1×1) monolayer on Au (111) surface after the second UPD peak[50].

In the study of Adzic's group, the Cu monolayer adsorbed on different substrates is subsequently galvanically displaced with $PtCl_4^{2-}$ ions in order to place a Pt monolayer on the substrates. They have placed the Pt monolayer on different single crystal electrodes (Au, Pd, Ir, Ru and etc.) and studied the catalytic activities toward the oxygen reduction reaction (ORR), and their results are provided in Fig. 2.7. They have also developed a scale-up synthesis method based on Cu UPD to produce gram-quantity Pt monolayer catalysts[51]. The core-shell structure for the Pt monolayer on Pd nanoparticles, prepared by this scale-up Cu UPD synthesis method, is studied by the scanning transmission electron microscopy (STEM), high-angle annular dark field (HAADF) image, and the elemental line scan profile by the energy dispersive spectroscopy (EDS), as shown in Fig. 2.8. The Pt monolayer nanocatalysts supported on Pd cores exhibite enhanced and stable activities for the ORR at the cathode in fuel cells[52], as shown in Fig. 2.9.

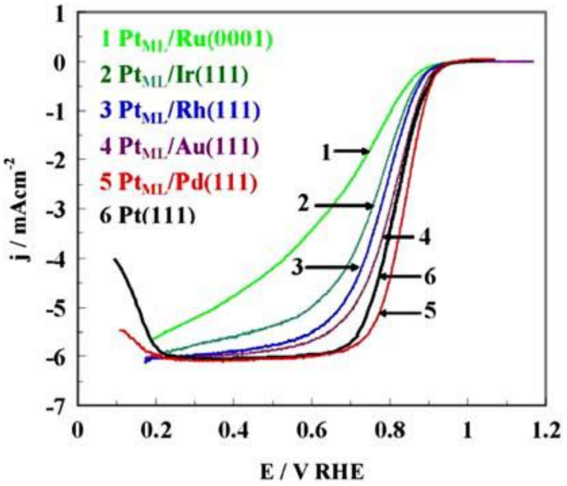

Figure 2.7 Polarization curves for the ORR on the Pt monolayer supported on different single crystal surfaces[53, 54].

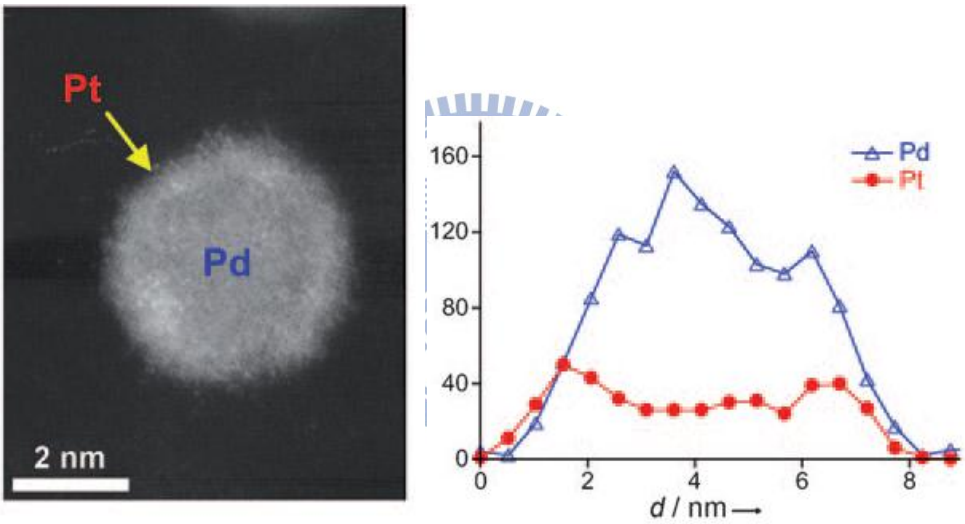

Figure 2.8 STEM HAADF image (left) and the EDS line scan profile (right) indicating the core-shell structure of the Pt monolayer catalyst on Pd nanoparticles[52].

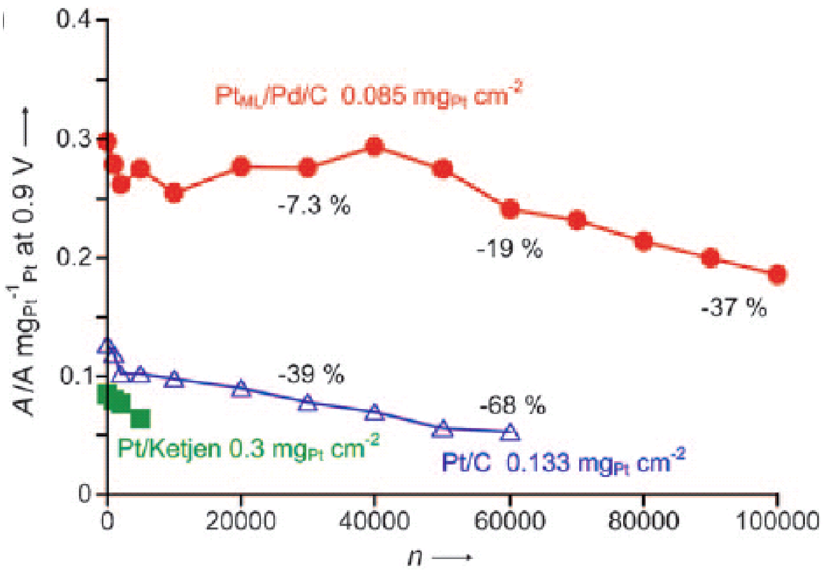

Figure 2.9 The Pt mass activities for the ORR as a function of the potential cycle number *n* during fuel cell testing for the Pt monolayer catalyst on Pd nanoparticles (red), compared to those for commercial Pt/C catalysts (green and blue). The potential cycles were square waves with a 30s dwell time at 0.7 and 0.9 V each (vs. RHE) at 80 °C[52].

The Pt monolayer catalysts prepared by the Cu UPD have also been applied as the anode catalyst in fuel cells. Pt reveal reasonable activities for hydrogen oxidation reaction (HOR), but suffers from undesirable CO tolerance. The CO exists either as an inevitable impurity in the H_2 gas feed produced by re-forming ethanol or hydrocarbons used as the fuel for the proton-exchange membrane H_2/O_2 fuel cells (PEMFC), or as the byproduct produced in the process of methanol oxidation reaction (MOR) for the direct methanol fuel cells (DMFC). The Pt monolayer catalysts on Ru nanoparticles exhibit higher CO tolerance for the HOR (Fig. 2.10) and more stable activity for MOR (Fig. 2.11). All these results in literatures suggest that the CO-tolerant ability for PtRu catalysts depends strongly on their geometrical structures and atomic distributions.

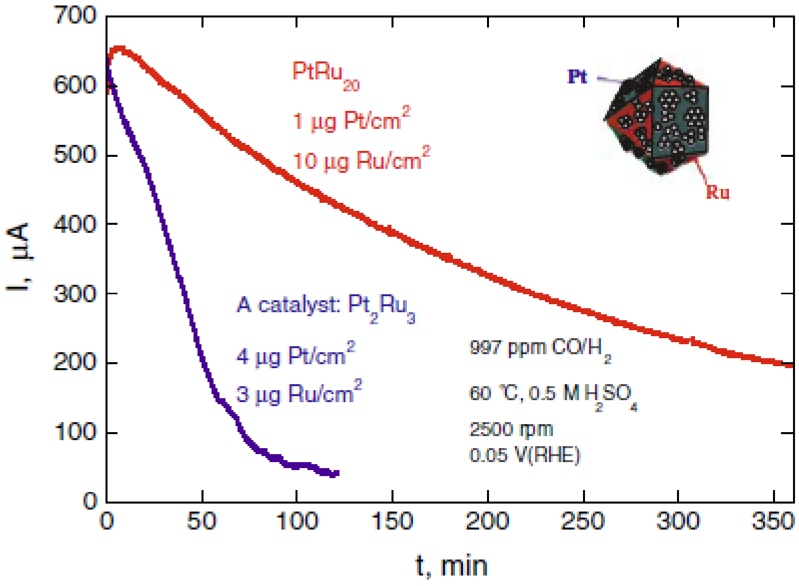

Figure 2.10 The structure for the Pt submonolayer catalyst on Ru core (the inset) $PtRu_{20}$ and its HOR behavior for the CO tolerance test, compared to that of a commercial Pt_2Ru_3 catalyst[4, 12, 55].

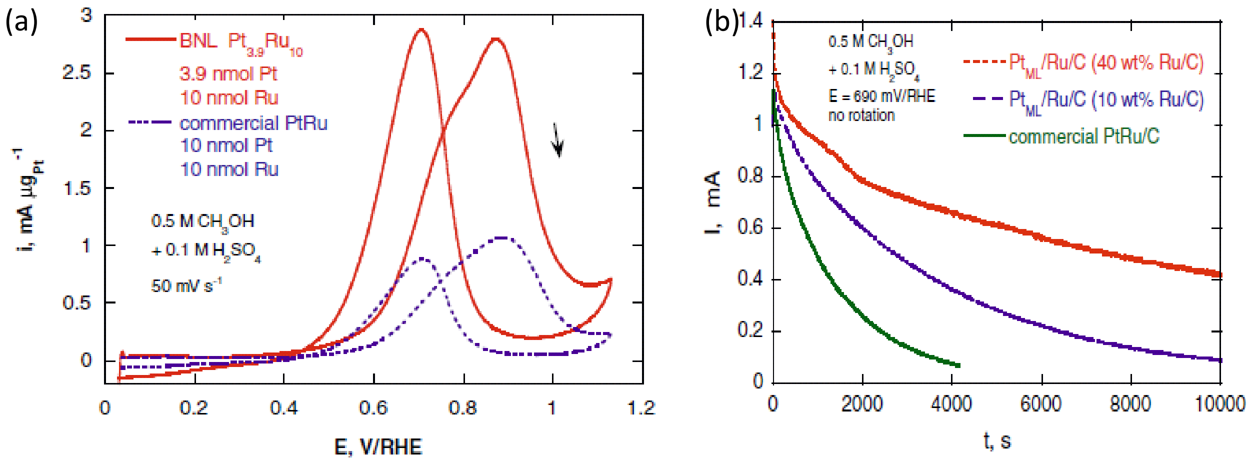

Figure 2.11 (a) Methanol-oxidation currents normalized by the total noble-metal mass, and (b) the chrono-potentiometric measurements at 0.69 V for the MOR, for the Pt monolayer catalyst on Ru nanoparticles, compared to that on the commercial PtRu catalyst[12].

2.3 Carbon based materials

2.3.1 Applications in fuel cells

Carbon-based materials display sufficient electrical conductivity, chemically inert structure, large surface area, porosity, and most importantly, inexpensive material cost. As a result, carbon demonstrates potential applications in many electrochemical fields such as capacitors and fuel cells. Nanostructured carbon materials exhibit enhanced electrical conductivity and chemical stability, and thus become rather promising for applications in electrochemical fields. For example, carbon nanotubes (CNTs) decorated with metal nanoparticles as catalysts have improved the performance of fuel cells. One primary reason is the extraordinary electrical conductivity of CNTs that can reduce unnecessary energy dissipation. The other secondary reason is that the special two-dimensional hexagonal structure of CNTs improves the dispersion uniformity and thus the utilization and catalytic activities of metal nanocatalysts. As shown in Fig. 2.12, PtRu nanoparticles decorated on CNTs exhibit a higher activity for the MOR than the commercial PtRu catalyst.

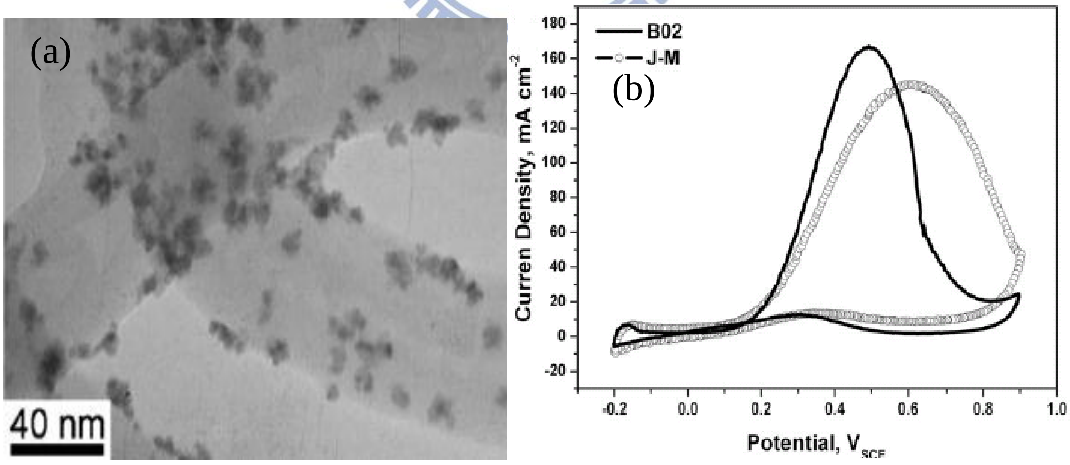

Figure 2.12 (a) TEM image of PtRu nanoparticles decorated on CNTs (sample B02). (b) Cyclic voltammograms for the MOR of PtRu nanoparticles on CNTs (B02) and commercial PtRu catalyst produced by Johnson Matthey (J-M), in N_2-saturated 0.5 M H_2SO_4 + 1 M CH_3OH electrolytes, 20 mV/s[56].

2.3.2 Surface functionalization

The catalytic activities for metal nanocatalysts supported on carbon-based materials are affected by the chemical properties of the carbon supports. First, most of the chemically-stable carbon structures are graphitic arrangements, in which carbon atoms are bound together by sp^2 hybrid bonds. This ring-like structure reveals a significant hydrophobicity. However, oxygen-containing functional groups can be generated on the carbon surface by the interaction between the defective sites on the carbon surface with unsaturated bonding and water molecules in aqueous solutions. Such hydrophilic oxygen-containing functional groups on the carbon surface have strong adsorption tendency for metal ions in precursor solutions and thus enables more loading of metal catalysts on carbon supports.[57] In addition, spontaneous deposition of metal precursors on the carbon supports can occur because of the driving force from the reduction potential difference between carbon and metal ions[58, 59], as shown in Fig. 2.13 (a). Furthermore, the oxygen-containing functional groups (-OH, C=O and COOH) on the carbon supports can also promote MOR behaviors for Pt nanocatalysts[58], as shown in Fig. 2.12 (b).

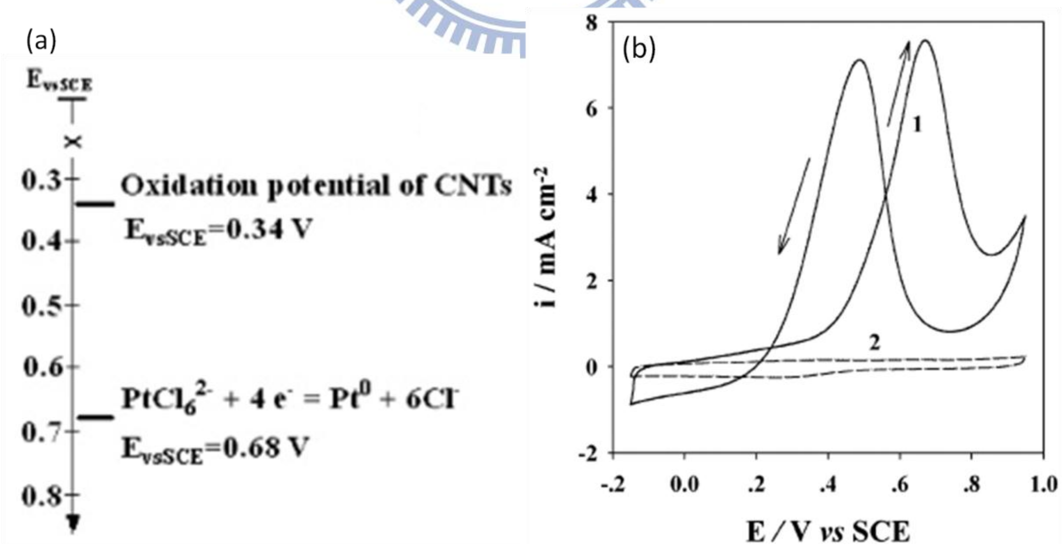

Figure 2.13 (a) The equilibrium potential diagram showing the potential difference between carbon (CNTs) and metal ions ($PtCl_6^{2-}$). (b) Polarization curves for the MOR on Pt nanocatalysts supported on CNTs with (line 1) and without (line 2) surface functionalization.[58]

2.4 Nafion ionomer

In the fuel cell, the solid polymer membrane acts as the proton conductor between the two electrodes allowing the rapid proton transport. The most commonly used solid electrolyte is Nafion ionomer (Dupont).

As shown in Fig. 2.14, Nafion consists of a strongly hydrophobic polytetrafluoroethylene (PTFE) backbone, and a strongly hydrophilic side chain ending with the sulphonic acid (SO_3H). Indeed, the –SO_3H group is ionically bonded, which makes the end of the side chain to be actually –SO_3^-. Due to the high hydrophilicity of the side chain, the regions around it will become hydrated via the absorption of large quantities of water. Protons are first gathered within these hydrated regions, and then they are mobile along the side chain because they are only weakly attracted by –SO_3^-, and they are eventually transported by the Nafion ionomer. This is how the Nafion ionomer works as the proton conductor[18, 19, 60, 61].

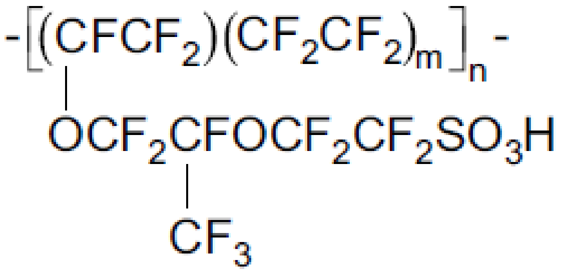

$$-[(CFCF_2)(CF_2CF_2)_m]_n- \quad | \; OCF_2CF(CF_3)OCF_2CF_2SO_3H$$

Figure 2.14 Example structure of a sulphonated fluoroethylene from Dupont[61].

Chapter 3 Enhancement of Methanol Electro-oxidaiton Performances via Core-Shell PtRu Nanoparticles Prepared by Pulse Current Deposition

3.1 Introduction

Development of clean and affordable energy has attracted considerable attention due to rising concerns over oil price and harmful CO_2 emission. Among the possible systems under study, the direct methanol fuel cell (DMFC) is recognized as a promising power source for applications in portable electronics and transportations.[1, 2] Because electro-oxidation of methanol is intrinsically slow, many materials have been investigated as electrocatalysts at the anode. They include alloys in binary, tertiary, and quaternary compositions such as PtRu, PtCo, PtRuCo, and PtRuNiZr.[27, 62-65] So far, the PtRu has appeared as the leading candidate with superb1 ectrocatalytic performance. It is because by alloying with Ru, the undesirable Pt poisoning by CO could be largely reduced. Mechanisms including bifunctional effect and ligand model are proposed to explain the contributory role of Ru while alloying with Pt.[66, 67] Moreover, the catalytic behaviors of PtRu depend greatly on its surface composition. For example, Richarz et al. prepared the Pt_xRu_{1-x} in various compositions and determined the $Pt_{0.5}Ru_{0.5}$ to possess the highest activity for methanol electro-oxidation.[32]

In practice, the PtRu is impregnated on appropriate carbon supports for an extended reaction interface. Conventional synthetic approaches for the PtRu-catalyzed electrodes entail techniques in chemical reduction and hydrogen annealing.[42, 68] These methods add substantial difficulties in controlling the locations and compositions of the resulting PtRu nanoparticles. In contrast, approaches involving electrochemical reductions are rather straightforward. Because the growths of PtRu nanoparticles are occurring selectively at the interface between electrode and electrolyte, the electrodeposition routes are recognized to produce electrodes with exceptional efficiencies in the catalyst utilization, albeit with moderate size distributions.[56, 69] Because the nuclei formation and growth are extremely sensitive to the overpotentials imposed, potentiostatic and galvanostatic depositions are known to produce distinct morphologies and compositions in the resulting PtRu nanoparticles. Between them, the galvanostatic deposition is suitable to prepare catalysts in a larger geometric area and better distributions, in addition to simpler operation setups.[38, 40, 70, 71]

In the galvanostatic depositions, the driving forces are imposed in manners of direct current or pulse current (pc). With a single variable in current density (J_a), the dc deposition is known to produce dendritic morphologies, because growths of the deposit are capped by the mass transport at a diffusion-limiting current.[72] In contrast, deposition in the pc mode allows independent adjustments of J_a, current on-time (T_{on}), and current off-time (T_{off}), offering more opportunities to obtain deposits with desirable attributes. As a result, many groups have employed pc depositions to fabricate electrocatalysts in Pt and PtRu.[38, 40, 70, 73-75] For example, Choi et al. reported notable advantages of pc deposition in particle sizes, adhesions, and uniform distributions.[73]

During the T_{off} in a pc deposition for binary alloys, differences in the redox potentials for the deposited metals often render a spontaneous galvanostatic displacement reaction in which the constituent of less positive redox potential dissolves from the deposit while the one with a higher redox potential is reduced from the electrolyte. A well-studied system is the CuNi alloy where detailed theoretic modeling and experimental results were discussed.[76-78] In this system, the Ni was alternately deposited and dissolved during T_{on} and T_{off}, while the Cu was deposited continuously. Hence, the ratio for the T_{on}/T_{off} played an important role in determining the resulting CuNi composition. So far, many groups have employed the displacement reaction to prepare substrates with unique surface layers.[23, 79-82] For instance, noble films of Au, Pd, and Pt were deposited on Ge substrates with reasonable adhesions.[79] In addition, Brankovic et al. have explored the spontaneous depositions of Pt on both singlecrystalline and nanoparticulate Ru surfaces.[34, 83, 84] In Ru single crystals, they believe the surface oxidations are responsible for the reduction of $PtCl_6^{2-}$ from the electrolyte. However, in the case of nanoparticles, partial dissolutions of Ru are likely to contribute to the $PtCl_6^{2-}$ reductions.

To date, many groups have employed pc deposition to fabricate PtRu nanoparticle and characterize their electrochemical performances.[38, 70, 72, 74, 75] However, none of them discussed the possible influences of displacement reaction in determining the resulting PtRu compositions. In this work, we investigate relevant variables to identify the effect of displacement reaction by carrying out careful analysis on the compositions and associated methanol electro-oxidation behaviors.

3.2 Experimental

Commercial carbon (XC-72R) on carbon cloth

A carbon cloth (E-TEK) is used as the starting substrate for the growth of PtRu. Prior to the PC deposition process, the carbon cloth is coated with an ink dispersion in which 5.0 mg Nafion solution (5.0 wt %) and 8.0 mg carbon powders (Vulcan XC-72R) are mixed in 5.0 mL 99.5 wt % ethanol for 30 min. The ink dispersion is deposited repeatedly on a 2×2 cm^2 carbon cloth which is kept at 80 ˚C atop a hotplate to evaporate the residual solvent. The weight of the coated electrode is 26.3 mg/cm^2. Subsequently, an electrochemical conditioning step is conducted by imposing five voltammetric scans on the coated carbon cloth at potentials between -0.2 and +1.1 V (vs. Ag/AgCl) at a scan rate of 50 mV/s in an electrolyte of 0.5 M H_2SO_4. The purpose for this treatment is to homogenize the coated carbon cloth and expose a larger effective surface area.

PtRu pulse current electroplating

The plating bath for the electrodeposition is formulated by mixing 99.9 wt % $RuCl_3$ (Sigma-Aldrich) and 97.0 wt % $NaNO_2$ (Showa) in an aqueous solution at 100 ˚C for 1.0 h, followed by dissolution of 99.9 wt % H_2PtCl_6. Afterward, the solution is cooled to room temperature with the addition of 97.0 wt % H_2SO_4 (Showa) to increase the conductivity of the electrolyte. The resulting concentrations for the H_2PtCl_6, $RuCl_3$, $NaNO_2$, and H_2SO_4 are 0.005, 0.005, 0.050, and 0.250 M, respectively. The solution is aged for several days to reach a steady state for the complex ions. In the PC depositions, rectangular pulses with independent parameters in T_{on}, T_{off}, and J_a are explored. Three sets of experiments are designed to elucidate the effect of displacement reaction. First, T_{on} of 50 ms and J_a of 50 mA/cm^2 are selected with the T_{off} varied between 100 and 600 ms. Second, T_{off} of 400 ms and J_a of 50 mA/cm^2 are chosen with the T_{on} varied between 25 and 400 ms. Lastly, we maintain the T_{on} and T_{off} at 50 and 400 ms, but adjust the J_a between 75 and 200 mA/cm^2. Throughout our experiments, the total coulombic charge is kept at 8.0 C/cm^2. Once the deposition is completed, the carbon cloth was removed and washed for subsequent methanol electro-oxidation characterizations.

Electrochemical analysis

The electrochemical measurements were conducted at 26℃ in a three-electrode arrangement using an EG&G 263A. First, to evaluate the electrochemical surface area (ECSA), the PtRu-catalyzed carbon cloths were subjected to cyclic voltammetric (CV) scans in the voltage range of -0.2 and 0.9 V in H_2SO_4 at a scan rate of 50 mV/s. The ECSA was estimated by the integrated charge in the hydrogen desorption region.[85, 86] Next, for catalytic abilities on the methanol electro-oxidation, multiple CV sweeps were performed in a potential range of -0.2 and 0.9 V at a scan rate of 20 mV/s in 500 mL of 0.5M H_2SO_4 and 1.0 M CH_3OH, The area for the working electrode was 1.0 cm^2. The Ag/AgCl and Pt foil (10 cm^2) were used as the reference and counter electrodes, respectively. The CV scan at the second cycle was used for comparison purposes.

Materials characterizations

For phase confirmation of the deposited PtRu nanoparticles, X-ray diffraction (XRD, Siemens D5000) with a Kα of 1.54 Å was employed. A transmission electron microscope (TEM, Philips Tecnai-20) was used to observe the morphologies and distributions for the PtRu nanoparticles. The average sizes and standard deviations of the PtRu nanoparticles were obtained by analyzing images from the TEM through software (Image-Pro Plus 6.0). Catalyst loadings of the PtRu after the pc depositions were determined by an inductively couple plasma mass spectrometry (ICP-MS, SCIEX ELAN 5000), where the samples were dissolved in a solution containing HCl, HNO_3, and HF at a 2:2:1 volume ratio. X-ray photoelectron spectroscopy (XPS, Thermo Microlab 350) was used to confirm the oxidative states of Ru in the PtRu nanoparticles.

3.3 Results and discussion

3.3.1 Various T_{off} for pulse electroplating

Previously, several reports have identified the nitroso compounds of Ru to be promising complexes as the Ru sources for PtRu electrodepositions.[31, 35, 36] When dissolved in an acidic electrolyte, a spontaneous Ru deposition was not observed in nitroso precursors as compared to the typical $RuCl_3$.[87] This contributed to a longer lifetime and minimal bath management. In addition, Gavrilov et al. indicated that the presence of nitroso ligands shifts Ru/Ru(III) redox potential to more positive values.[88] Therefore, with the selection of nitroso precursor, similar Pt:Ru ratios are expected to be obtained in both deposit and solution states. This is especially critical because previous studies using the $RuCl_3$ and $RuCl_5$ reported substantial Pt enrichments with respect to their concentration ratios in the electrolyte. Consequently, their fabrications of desirable PtRu compositions hinged on empirical determination entirely.

Our preparation steps of nitroso Ru precursor followed earlier documentation in which the dissolution of $RuCl_3$ in excess $NaNO_2$ at elevated temperatures was carried out.[89] The resulting complex was confirmed by Blake et al. to be $Ru(NO)(NO_2)_4(OH)^{2-}$.[90] However, in our electrolyte we also added H_2PtCl_6 after the formation of Ru nitroso complex. Because the molar ratio for Pt:Ru:$NaNO_2$ was 1:1:10, we surmise that the simultaneous presence of $PtCl_6^{2-}$ and $Pt(NO_2)_xCl_{6-x}^{2-}$ is likely. The color for the plating bath is in light yellow. This is in sharp contrast with the electrolytes of $RuCl_3$ and $RuCl_5$, which appear in dark brown.

For the pc depositions, intricate interactions between T_{on}, T_{off}, and J_a exert significant influences over the PtRu catalyst loadings, compositions, distributions, as well as particle sizes. Therefore, careful scrutiny in the plating variables would be necessary. In our first set of experiments, pc depositions were conducted at various T_{off}, while the T_{on} and J_a remained unchanged at 50 ms and 50 mA/cm^2, respectively. Because we maintained the total charge constant at 8.0 C/cm^2, the entire deposition process lasted approximately 4–35 min. Table 3.1 lists the experimental parameters as well as results from TEM and ICP-MS for the PtRu nanoparticles. As presented, the PtRu loadings were in the range of 67.6–128.5 μg/cm^2. Following faradaic law, the coulombic efficiencies were estimated at 1.8–3.6%. These reduced values are attributed to the parasitic hydrogen evolution occurring on the Pt surfaces. Currents from the capacitive charge and discharge were not expected to be substantial, as the effective working range for the capacitance component were less than 1.0 ms for T_{on} and T_{off}.[75] We observed a notable trend for the PtRu composition on different pulses. The ratio for the Pt in the PtRu nanoparticles increased considerably with a longer T_{off}. At the shortest T_{off} of 100 ms, we determined the composition to be $Pt_{52.7}Ru_{47.3}$. In contrast, at the largest T_{off} of 600 ms, the makeup was confirmed as $Pt_{83.4}Ru_{16.6}$.

Table 3.1. Results from materials characterizations on the PtRu nanoparticles with fixed values of T_{on} (50 ms), J_a (50 mA/cm^2), and total coulombic charge (8.0 C/cm^2).

T_{off} (ms)	Pt Loading (μg/cm^2)	Ru Loading (μg/cm^2)	Pt/Ru Atomic ratio	Total metal loading (μg/cm^2)	Average size (nm)	Standard deviation
100	62.5	28.9	52.8/47.2	91.4	7.2	5.6
200	89.8	38.7	54.6/45.4	128.5	12.9	8.7
300	64.0	21.0	61.2/38.8	85.0	6.6	5.4
400	52.4	15.2	64.1/35.9	67.6	4.1	2.8
500	78.5	11.5	77.9/22.1	90.0	6.3	4.7
600	100.8	10.4	83.4/16.6	111.2	11.3	9.4

TEM observations on the particles sizes indicated a slightly wider distribution as compared to those from conventional chemical reduction methods. For example, at a T_{off} of 200 ms, the PtRu nanoparticles were an average of 12.9 nm with a standard deviation of 8.7 nm. Moderate size distributions are typical, because the nucleation and growth took place during each individual pulse. A recent report by Bennett et al. also observed similar behaviors when they prepared Pt nanoparticles on diamond thin films.[91] Figure 3.1 provides the representative TEM images for the PtRu nanoparticles from T_{off} of 400 and 600 ms, respectively. The average size of the PtRu nanoparticles from the T_{off} of 400 ms was 4.1 nm, while the T_{off} of 600 ms revealed a somewhat larger size of 11.3 nm. These TEM images also indicated that the PtRu nanoparticles were dispersed uniformly on the carbon substrates with negligible aggregation.

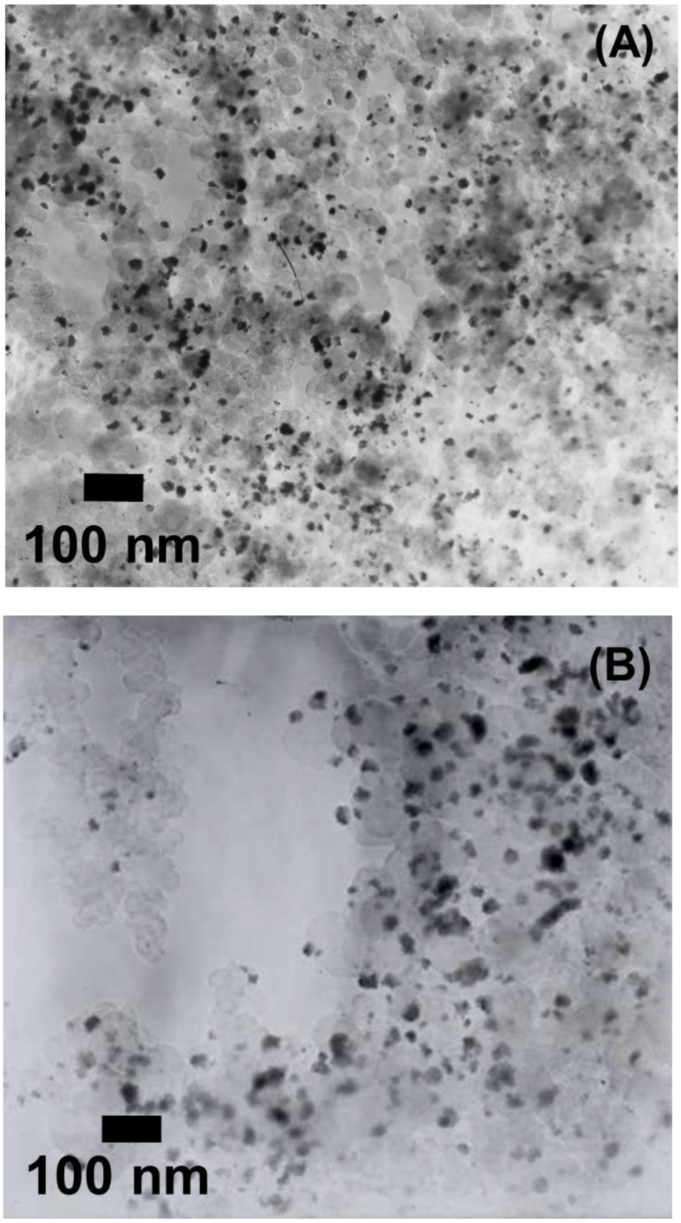

Figure 3.1. Representative TEM images for the PtRu nanoparticles with fixed values of T_{on} (50 ms), J_{a} (50 mA/cm^2), and coulombic charge (8.0 C/cm^2), as well as T_{off} of (A) 400 and (B) 600 ms.

Fig. 3.2 exhibits the CV profiles in mass activity for the PtRu catalyzed electrodes at various T_{off}. Critical information from the CV responses, including the onset potentials, peak current (i_{a}) and potential (V_{a}) at anodic scans, peak current (i_{c}) and potential (V_{c}) at cathodic scans, as well as values for ECSA, are listed in Table 3.2. For the samples with T_{off} in 100 and 200 ms, their CV curves revealed moderate current outputs. This is unexpected, because compositions for these two samples were $Pt_{52.8}Ru_{47.2}$ and $Pt_{54.6}Ru_{45.4}$, respectively. In contrast, the CV profiles of the remaining samples demonstrated obvious anodic signals with relatively reduced cathodic signals, suggesting considerable abilities for the methanol electro-oxidation. In addition, the onset potentials became smaller when the amount of Ru was increased, a fact that is consistent with what was reported in literature that alloying with Pt promotes methanol electro-oxidation. The ratio for the i_a/i_c indicates the capabilities to remove CO after methanol dehydrogenation. Among these samples, the one with T_{off} of 400 ms demonstrated the highest value. As expected, for the mass activities, the sample with T_{off} in 400 ms exhibited the highest value of 213 mA/mg_{Pt}. Moreover, the general trend for the ECSA was consistent with that of i_a, in which a larger ECSA is associated with a higher i_a.

Table 3.2. Electrochemical parameters from the CV scans in mass activity of the PtRu-Catalyzed carbon cloths with fixed values of T_{on} (50 ms), J_a (50 mA/cm^2), and total coulombic charge (8.0 C/cm^2).

T_{off} (ms)	Anodic scan		Cathodic scan		ECSA^e (cm^2/Pt mg)	i_a/i_c
	$V_a$$^{a)}$ (mV)	$i_a$$^{b)}$ (mA/mg $_{Pt}$)	$V_c$$^{c)}$ (mV)	$i_c$$^{d)}$ (mA/cm^2)		
100	516.3	52.5	NA	NA	251.0	NA
200	509.8	48.9	NA	NA	209.3	NA
300	521.2	116.5	387.5	NA	477.3	NA
400	560.4	213.8	360.0	0.7	751.4	304.6
500	558.7	133.4	448.6	51.1	286.0	2.61
600	541.6	119.8	407.0	50.1	152.5	2.39

a) potential at peak current density in anodic scan

b) peak mass activity in anodic scan

c) potential at peak current density in cathodic scan

d) peak mass activity in cathodic scan

e) ECSA from hydrogen desorption data

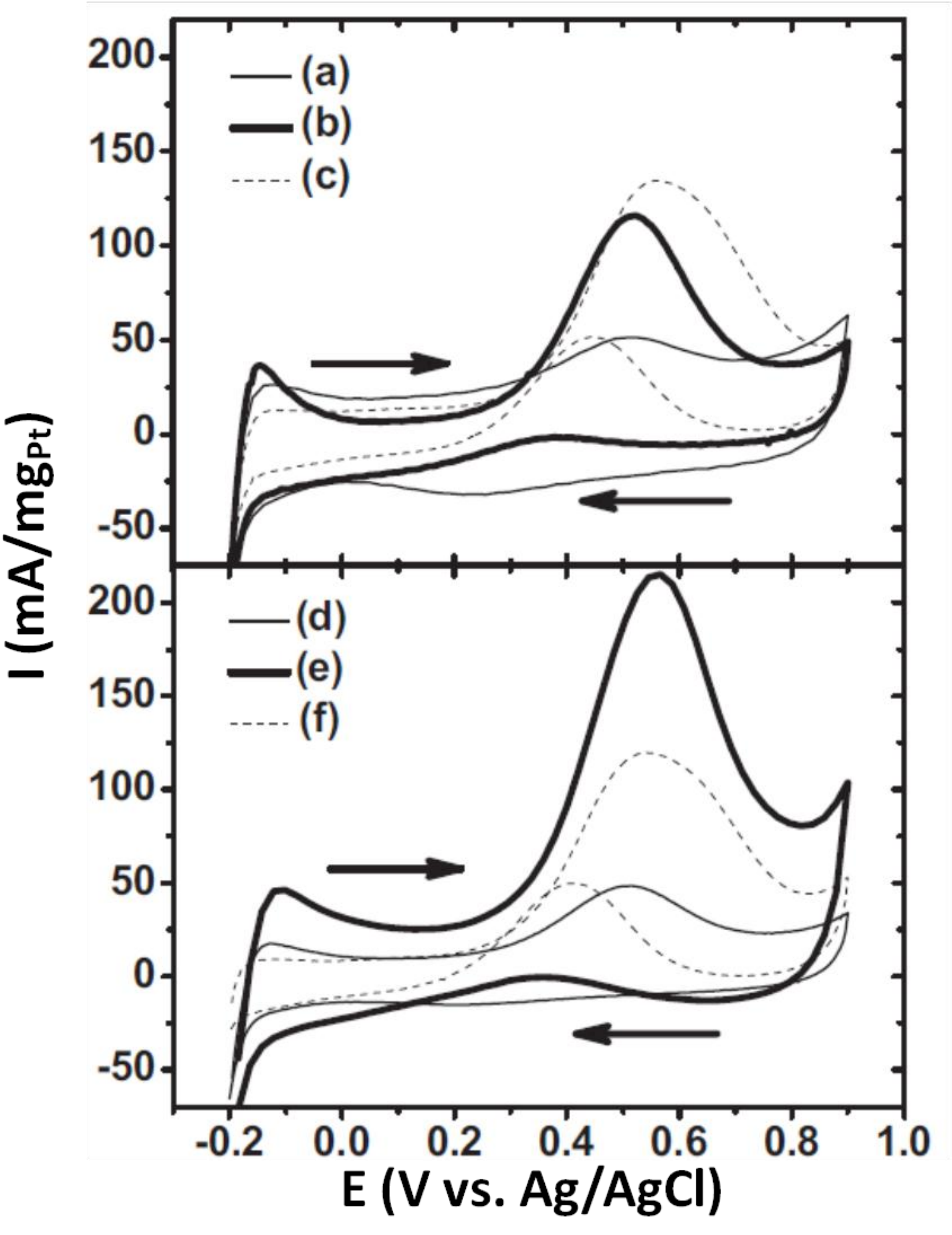

Figure 3.2. CV profiles in mass activity for the PtRu-catalyzed carbon cloths with fixed values of T_{on} (50 ms), J_a (50 mA/cm^2), and coulombic charge (8.0 C/cm^2), as well as T_{off} of (a) 100, (b) 300, (c) 500, (d) 200, (e) 400, and (f) 600 ms.

3.3.2 Various T_{on} for pulse electroplating

In our second set of experiments, the pc depositions were carried out at various T_{on} while the T_{off} and J_a were held at 400 ms and 50 mA/cm^2, respectively. Because we kept the total charge unchanged at 8.0 C/cm^2, the entire deposition process lasted approximately 2.6–45.0 min. Table 3.3 provides the experimental conditions as well as results from TEM and ICP-MS for the PtRu nanoparticles. As listed, the PtRu loadings were in the range of 67.6–128.8 μg/cm^2. Similarly, the coulombic efficiency was estimated at 1.8–2.6%. These values were in line with results obtained from our first set of experiments. An interesting trend was observed in which a longer T_{on} resulted in a lower amount of Pt in the PtRu nanoparticles. At the shortest T_{on} of 25 ms, we recorded the composition to be $Pt_{90.9}Ru_{9.1}$. In contrast, at the largest T_{on} of 400 ms, a composition of $Pt_{52.5}Ru_{47.5}$ was measured.

TEM observations on the PtRu nanoparticles confirmed a similar pattern in the size distributions. For example, at a T_{on} of 25 ms, we obtained the average size to be 6.7 nm with a standard deviation of 5.0 nm. At a larger T_{on} of 400 ms, the average size was 8.4 nm with a standard deviation of 7.4 nm. Representative TEM pictures from those two samples are provided in Fig. 3.3. Consistent with images in Fig. 3.1, the PtRu nanoparticles were deposited uniformly throughout the substrates without aggregation. Fig. 3.4 demonstrates the CV profiles in mass activity for the PtRu nanoparticles at various T_{on}. Relevant parameters from the CV responses are also provided in Table 3.4. Apparently, all the samples revealed obvious anodic peaks without notable cathodic peaks. They suggest the presence of reasonable catalytic behaviors for methanol electro-oxidation. As expected, the onset potentials and the peak potentials at the anodic scans became smaller with increasing Ru amounts. The sample with a T_{on} of 50 ms revealed the highest mass activities, reaching values at 213.8 mA/mg$_{Pt}$. Similarly, the trend of ECSA agreed with that of i_a, a fact we established in the previous set of experiments.

Table 3.3. Results from materials characterizations on the PtRu nanoparticles with fixed values of T_{off} (400 ms), J_a (50 mA/cm^2), and total coulombic charge (8.0 C/cm^2).

T_{on} (ms)	Pt Loading (μg/cm^2)	Ru Loading (μg/cm^2)	Pt/Ru Atomic ratio	Total metal loading (μg/cm^2)	Average size (nm)	Standard deviation
25	92.3	4.7	90.9/9.1	97.0	6.7	5.0
50	52.4	15.2	64.1/35.9	67.6	4.1	2.8
100	88.8	40.0	53.7/46.3	128.8	8.3	5.2
200	56.1	27.3	51.5/48.5	83.4	8.7	5.0
400	48.1	22.5	52.5/47.5	70.6	8.4	7.4

Table 3.4. Electrochemical parameters from the CV scans in mass activity of the PtRu-catalyzed carbon cloths with fixed values of T_{off} (400 ms), J_a (50 mA/cm^2), and total coulombic charge (8.0 C/cm^2).

T_{on} (ms)	Anodic scan		Cathodic scan		ECSA^{e} (cm^2/Pt mg)	i_a/i_c
	$V_a^{a)}$ (mV)	$i_a^{b)}$ (mA/mg $_{Pt}$)	$V_c^{c)}$ (mV)	$i_c^{d)}$ (mA/cm^2)		
25	565.1	66.3	433.1	12.7	105.0	5.20
50	560.4	213.8	360.0	0.7	751.4	304
100	540.0	81.2	NA	NA	188.9	NA
200	539.2	100.1	NA	NA	296.0	NA
400	518.0	108.7	NA	NA	130.4	NA

a) potential at peak current density in anodic scan

b) peak mass activity in anodic scan

c) potential at peak current density in cathodic scan

d) peak mass activity in cathodic scan

e) ECSA from hydrogen desorption data

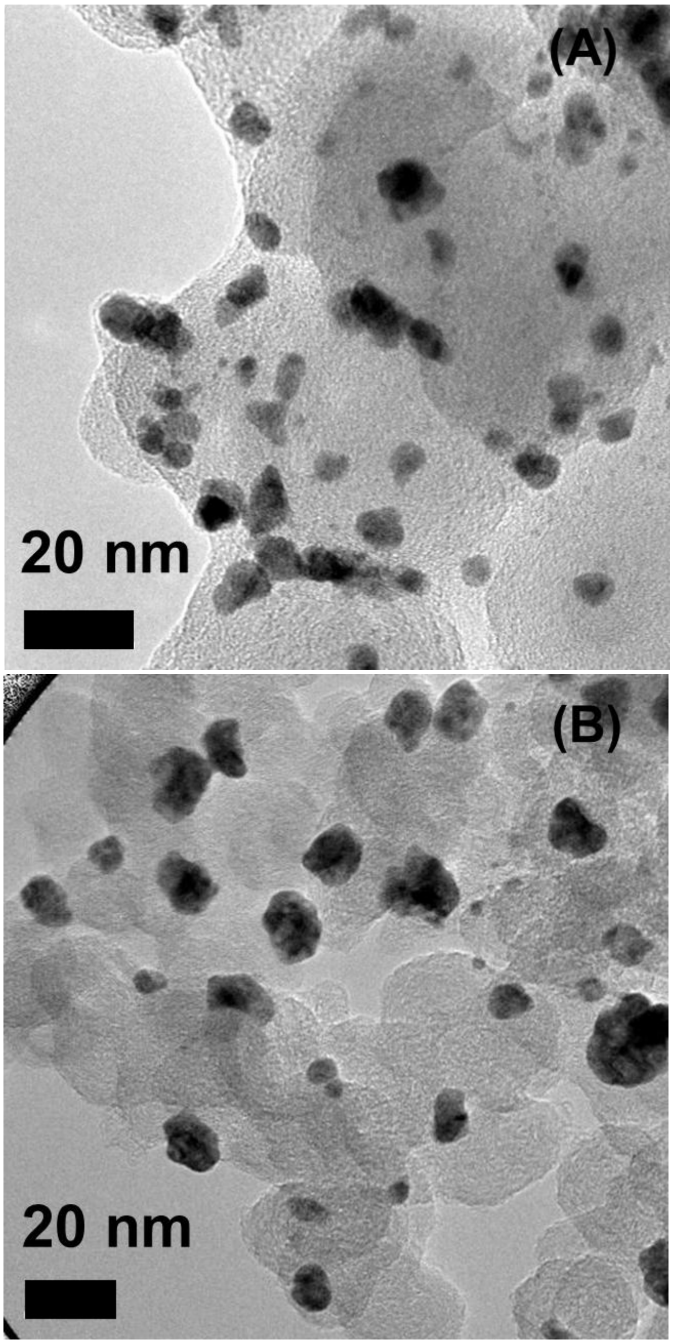

Figure 3.3. Representative TEM images for the PtRu nanoparticles with fixed values of T_{off} (400 ms), J_a (50 mA/cm^2), and coulombic charge (8.0 C/cm^2), as well as T_{on} of (A) 25 and (B) 400 ms.

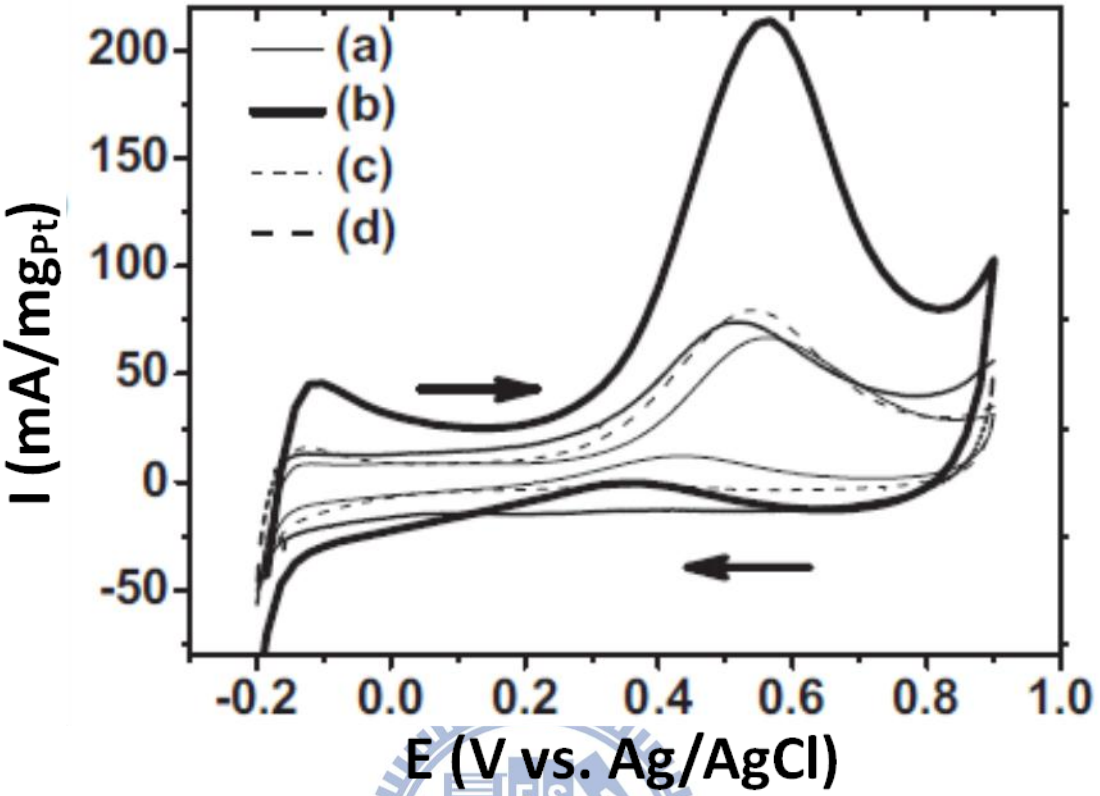

Figure 3.4. CV profiles in mass activity for the PtRu-catalyzed carbon cloths with fixed values of T_{off} (400 ms), J_a (50 mA/cm^2), and coulombic charge (8.0 C/cm^2), as well as T_{on} of (a) 25, (b) 50, (c) 100, and (d) 400 ms.

3.3.1 Duty Cycle for pulse electroplating

We realized that the duty cycle, defined as T_{on} /(T_{on} + T_{off}), would be an appropriate indicator to solicit further information on the composition variations over T_{on} and T_{off}. As defined, a higher duty cycle is closer to the dc deposition, while a lower one represents a longer stop time between pulses. Fig. 3.5 exhibits the ratio of Pt in the PtRu nanoparticles as a function of duty cycle from the data listed in Tables 3.1 and Tables 3.3. Remarkably, the Pt ratio increased rapidly as the duty cycle was reduced. This infers that a longer T_{off} renders a pronounced effect of Ru loss in the PtRu nanoparticles. At higher duty cycles, we reached a plateau, with the resulting composition approaching $Pt_{52}Ru_{48}$. These behaviors were expected, because the galvanostatic deposition from nitroso precursors of Pt and from these samples were rather consistent, indicating that the pc deposition was insensitive to the current densities under study once the T_{on} and T_{off} were determined. In addition, the catalyst loadings were in the range of 49.1–67.6 μg/cm^2, values that are in line with earlier results. Table 3.6 also lists the electrochemical characteristics for these samples.

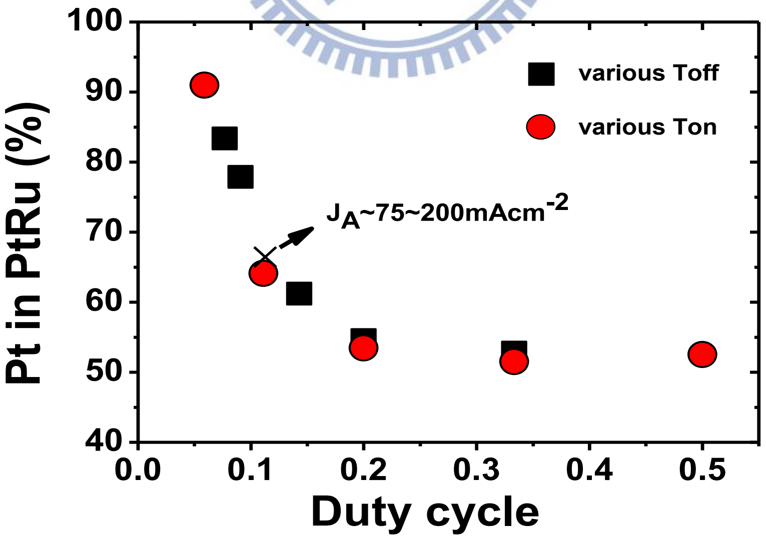

Figure 3.5. The effect of duty cycle on the Pt atomic ratio for the PtRu nanoparticles. Data are from Tables 3.1(■), 3.3 (○), and 3.5 (×).

Table 3.5. Results from materials characterizations on PtRu nanoparticles with fixed values of T_on (50 ms), T_off (400 ms), and total coulombic charge (8.0 C/cm^2).

J_a (mA/cm^2)	Pt Loading (μg/cm^2)	Ru Loading (μg/cm^2)	Pt/Ru Atomic ratio	Total metal loading (μg/cm^2)	Average size (nm)	Standard deviation
75	39.1	10.0	66.8/33.2	49.1	7.2	5.9
100	42.4	10.9	66.7/33.3	53.3	11.4	8.9
200	49.9	13.0	66.5/33.5	62.9	14.3	9.6

Table 3.6. Electrochemical parameters from the CV scans in mass activity of PtRu-catalyzed carbon cloths with fixed values of T_on (50 ms), T_off (400 ms), and total coulombic charge (8.0 C/cm^2).

J_a (mA/cm^2)	Anodic scan		Cathodic scan		ECSA[e] (cm^2/Pt mg)	$i_\mathrm{a}/i_\mathrm{c}$
	V_a a) (mV)	i_a b) (mA/mg $_\mathrm{Pt}$)	V_c c) (mV)	i_c d) (mA/cm^2)		
75	531.8	197.7	386.0	3.8	526.8	51.2
100	524.5	138.9	NA	NA	434.5	NA
200	487.0	37.4	NA	NA	243.4	NA

a) potential at peak current density in anodic scan

b) peak mass activity in anodic scan

c) potential at peak current density in cathodic scan

d) peak mass activity in cathodic scan

e) ECSA from hydrogen desorption data

To account for the apparent enrichment in the Pt at shorter duty cycles, we believe a displacement reaction was taking place where the Ru in the PtRu nanoparticles was preferentially dissolved while the Pt cations in the solution were reduced during T_off. This is attributed to the observed rise in the Pt ratio when the T_off was prolonged. The nature of displacement reaction could be supported by detailed XRD analysis on the PtRu nanoparticles to determine their lattice parameter. Fig. 3.6 exhibits the XRD patterns for the PtRu nanoparticles with T_off of 100, 400, and 600 ms, respectively. The complete parameters for their synthetic conditions are shown in Table 3.1.

Due to the interferences from carbon cloths, the XRD profiles were expectedly rough. Nevertheless, the signals from Pt(111), Pt(200), Pt(220), and carbon were identified. Because we did not observe the characteristic Ru peaks, we rationalize that alloying of Ru into the Pt lattice was successfully achieved. Moreover, because the atomic radius of Ru is smaller than that of Pt, substitution of Ru in the Pt unit cell results in the reduction of lattice parameters. This engenders a slight shift of diffraction peaks to larger angles. To minimize undesirable noises, we selected the signal from Pt(111), as shown in Fig. 3.7, to estimate the lattice parameter with the equation below

$$\mathrm{a} = \frac{\sqrt{3}\lambda_{k\alpha}}{2\ \sin\theta sin\theta_{max}} \qquad (3.1)$$

$$\mathrm{a} = a_0 - 0.124x_{Ru} \qquad (3.2)$$

where a is the lattice parameter, $\theta_{\max}$ is the peak position for Pt(111), and $\lambda_{k\alpha}$ is the wavelength of X-ray. The value for a could further be used to deduce the amount of alloyed Ru, as suggested by Antolini et al., in the following relation[92] where a0 is the standard lattice parameter from a bulk Pt (JCPDS: 870646) and x_{Ru} is the atomic Ru ratio in the alloyed state. The results from these estimations are presented in Table 3.7. As listed, we noticed that when the T_{off} was prolonged, the ratio for the alloyed Ru also decreased. This behavior is understandable, because when the displacement reaction was occurring (at larger T_{off}), the Ru on the surface were dissolved preferentially, leaving those buried inside (the alloyed Ru) intact. An alternative explanation for the Pt enrichment at shorter duty cycles is a cementation process. As proposed by Spendelow and Wieckowski, spontaneous deposition of Pt from electrolyte could proceed via the oxidation of Ru substrate.[93] In such a reaction, the Ru is not dissolved but exists in an oxidized state on the surface with metallic Pt deposited from the electrolyte. This model poses a drastic contrast with that of displacement reaction, where the Ru is dissolved. Therefore, we could identify the exact mechanism in our case simply by determining the oxidative states of Ru at different duty cycles.

Fig. 3.8(a) presents the XPS signals from Ru ($3p_{3/2}$) on samples of T_{off} in 100, 400, and 600 ms, respectively. The complete synthetic parameters can be obtained in Table 3.1. The selection of Ru ($3p_{3/2}$) instead of Ru ($3d_{5/2}$) was to avoid possible interference from that of C (1 s). As shown in the diagram, all the samples revealed rather broad profiles. The signals peaks were located at 462.2, 462.0, and 461.9 eV for samples of 100, 400, and 600 ms, respectively. Earlier, the peak for metallic Ru was documented at 461.1 eV, which was close to what we measured.[94] A slight deviation is expected, because there is a minor shift of Ru signals (less than 0.1 eV) in the PtRu from that of metallic Ru.[95] Nevertheless, our broad signals seem to suggest that Ru existed in multiple oxidative states. Furthermore, the XPS signal intensity decreased considerably with longer T_{off}, indicating that the amount of Ru, regardless of its oxidative states, decreases when the duty is reduced. This is consistent with our argument of steady Ru loss during T_{off}.

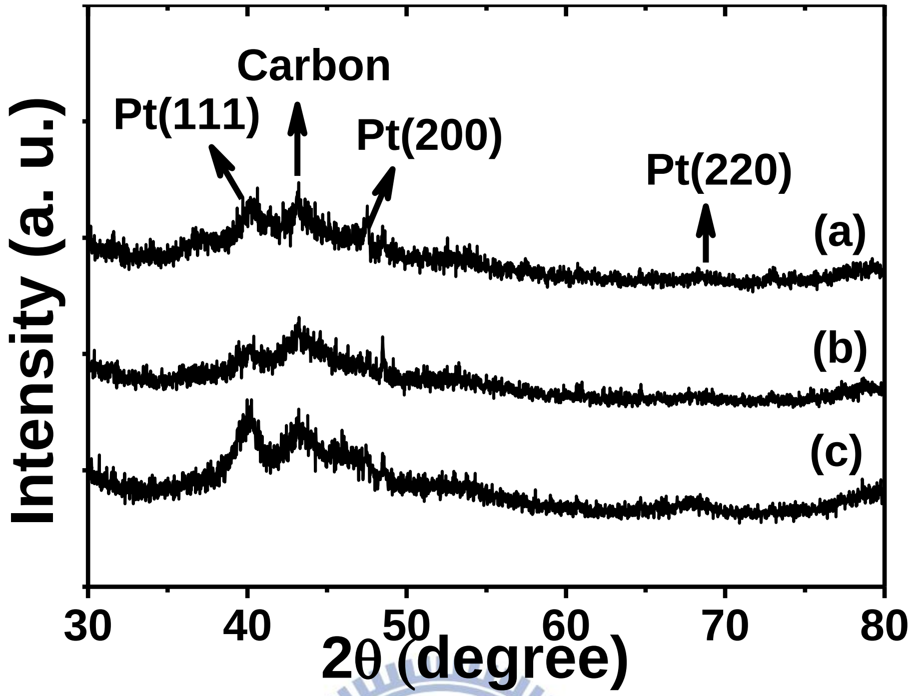

Figure 3.6. The XRD patterns for the PtRu nanoparticles with fixed values of T_{on} (50 ms), J_a (50 mA/cm^2), and coulombic charge (8.0 C/cm^2), as well as T_{off} of (a) 100, (b) 400, and (c) 600 ms.

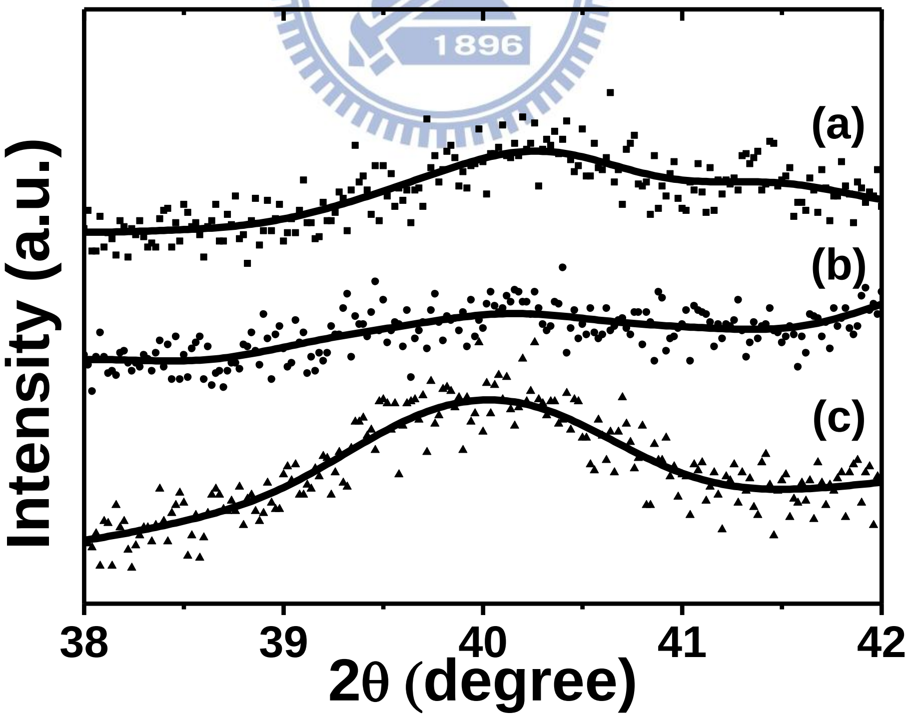

Figure. 3.7. XRD patterns from Fig. 3.6 with an enlarged range between 38 and 42° for lattice parameter determination.

Table 3.7. Lattice parameter and alloyed Ru for the PtRu nanoparticles with fixed values of T_{on} (50 ms), J_a (50 mA/cm^2), and coulombic charge (8.0 C/cm^2).

sample	Pt (111) peak (deg)	Lattice parameter *a* (Å)	X_{Ru} (%)	Pt/Ru atomic ratio[b]
TF100	40.21	3.879	33.9 ± 2	52.8/47.2
TF400	40.16	3.884	30.2 ± 2	64.1/35.9
TF600	39.97	3.902	15.9 ± 2	83.4/16.6
Pt[a]	39.79	3.920		

a) from JCPDS 870646

b) from ICP-Mass (as shown in Table 3.1)

In an acidic environment, we suspect the possible oxidation states of Ru are Ru^0, RuO_2, and $RuO_2 \cdot nH_2O$. To determine their relative ratios quantitatively, we carried out curve fitting using software (Thermo Avantage 3.20). The corresponding peaks for RuO_2, and $RuO_2 \cdot nH_2O$ were 462.2 and 463.8 eV, respectively.[93, 96] As shown in Fig. 3.8(b), we acquired a reasonable match for the observed XPS responses. The detailed fitting results are listed in Table 3.8. When the T_{off} was prolonged, we observed that the ratio for the metallic Ru increased, while the ratio for the $RuO_2 \cdot nH_2O$ decreased steadily. Interestingly, the ratio for the RuO_2 remained unchanged. Because the metallic Ru existed in the alloyed state buried inside the PtRu nanoparticles, the loss of Ru in the displacement reaction was likely from the $RuO_2 \cdot nH_2O$ on the surface.

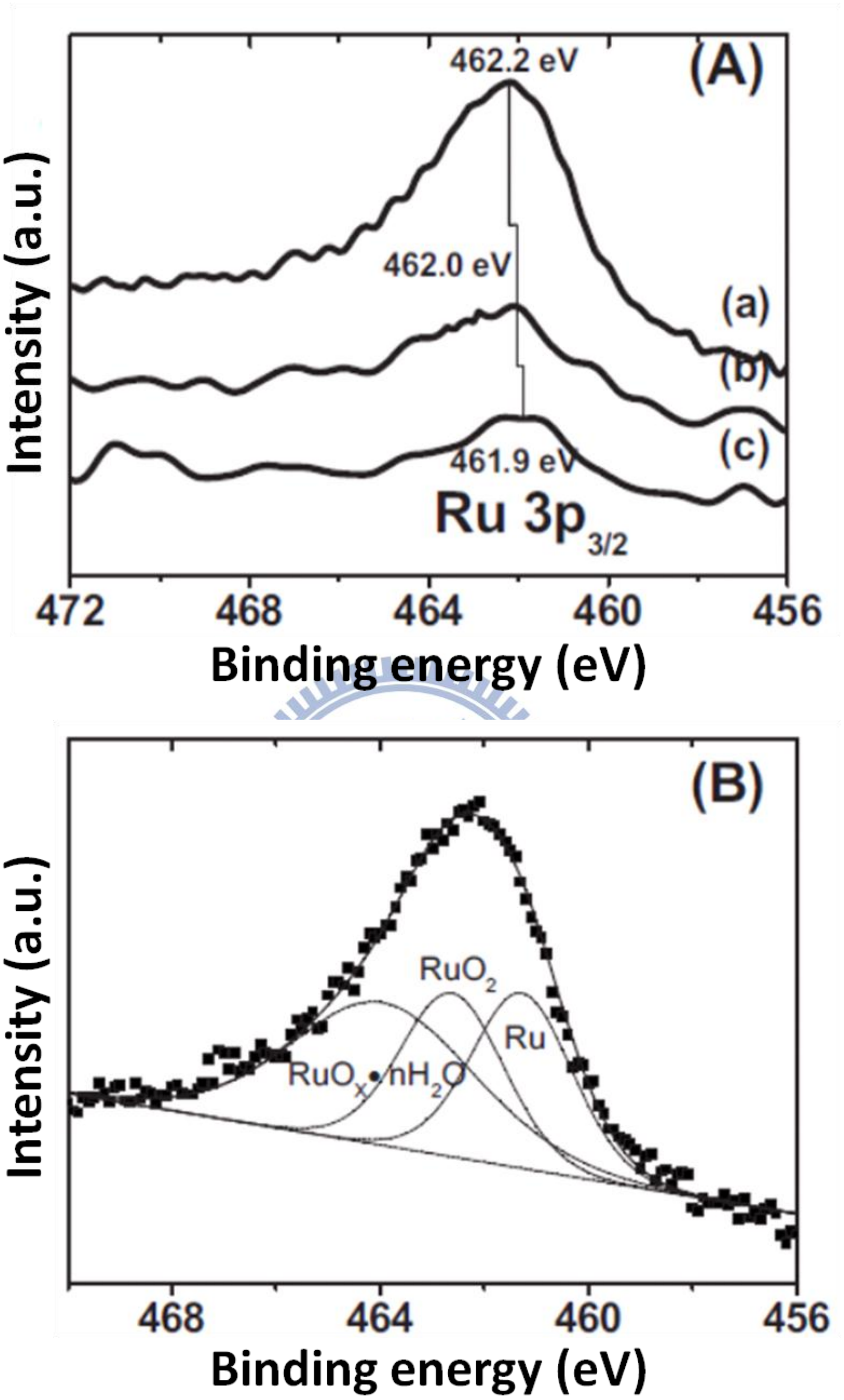

Figure 3.8. (A) XPS signals of Ru ($3p_{3/2}$) from PtRu nanoparticles with fixed values of T_{on} (50 ms), J_a (50 mA/cm^2), and coulombic charge (8.0 C/cm^2), as well as T_{off} in (a) 100, (b) 400, and (c) 600 ms. (B) The results of curve fitting using Ru^0, RuO_2, and $RuO_2 \cdot nH_2O$.

Table 3.8. Results from XPS and curve fitting of PtRu nanoparticles with fixed values of T_{on} (50 ms), J_a (50 mA/cm^2), and total coulombic charge (8.0 C/cm^2).

T_{off} (ms)	Binding energy[a] (eV)	Reference binding energy[b] (eV)	Suggested species	Ratio (%)
100	461.1	461.1	Ru	36.5
	462.6	462.2	RuO_2	33.9
	463.9	463.8	$RuO_2 \cdot nH_2O$	29.6
400	461.1	461.1	Ru	41.1
	462.4	462.2	RuO_2	34.5
	463.8	463.8	$RuO_2 \cdot nH_2O$	24.4
600	461.2	461.1	Ru	43.8
	462.4	462.2	RuO_2	36.4
	463.8	463.8	$RuO_2 \cdot nH_2O$	19.8

a) From XPS curve fitting

b) From Ref.[93, 94, 96]

3.3.4 X-ray absorption spectroscopy analysis

X-ray absorption spectroscopy (XAS) studies were carried out to investigate the atomic structures of PtRu nanoparticles with T_{off} of 100, 400 and 600 ms, respectively, and the samples were designated as TF100, TF400, and TF600, respectively. XAS spectra for the Pt $\mathrm{L_{III}}$-edge were obtained. Fig. 3.9(a) demonstrates the Pt $\mathrm{L_{III}}$-edge XANES and EXAFS spectra from PtRu nanoparticles with different T_{off}. The Pt $\mathrm{L_{III}}$-edge involves the energy associated with the electronic orbital transitions including $2p_{3/2} \rightarrow 5d_{5/2}$ and $2p_{3/2} \rightarrow 5d_{3/2}$, also known as the white line. In general, the white line intensity can be used to determine the oxidation state of Pt due to its relevance to the vacancy of the d-band orbitals such as $d_{5/2}$ and $d_{3/2}$. Usually a larger white line intensity indicates more vacant d-band orbitals, and consequently a higher oxidation state or a lower metallic state, and vice versa. The inset of Fig. 3.9(a) magnifies the white lines for our samples. It is noted that with a longer T_{off}, the metallic state of Pt inferred by the white line intensity of Pt $\mathrm{L_{III}}$-edge became higher. The TF600 sample with the longest T_{off} was the closest to the metallic state among all our samples. This agrees well with the Pt/Ru atomic ratios measured by ICP-MS (Table 3.9). The higher Pt/Ru atomic ratios in PtRu alloys indicated a lower alloying degree and hence a metallic state. The TF600 sample with the longest T_{off} revealed the highest Pt/Ru atomic ratios rendering the highest metallic state among our samples. It has been reported that the binding energy between Pt atoms with neighboring ones decreased in the PtRu alloy.[36] Because the Ru atoms incorporating in the Pt lattice substituted some Pt atoms while the overall crystalline structure remained as fcc structure, the binding energy for Pt was altered magnificently. This resulted in the observed white line increase for PtRu nanoparticles as compared to that of Pt foil.

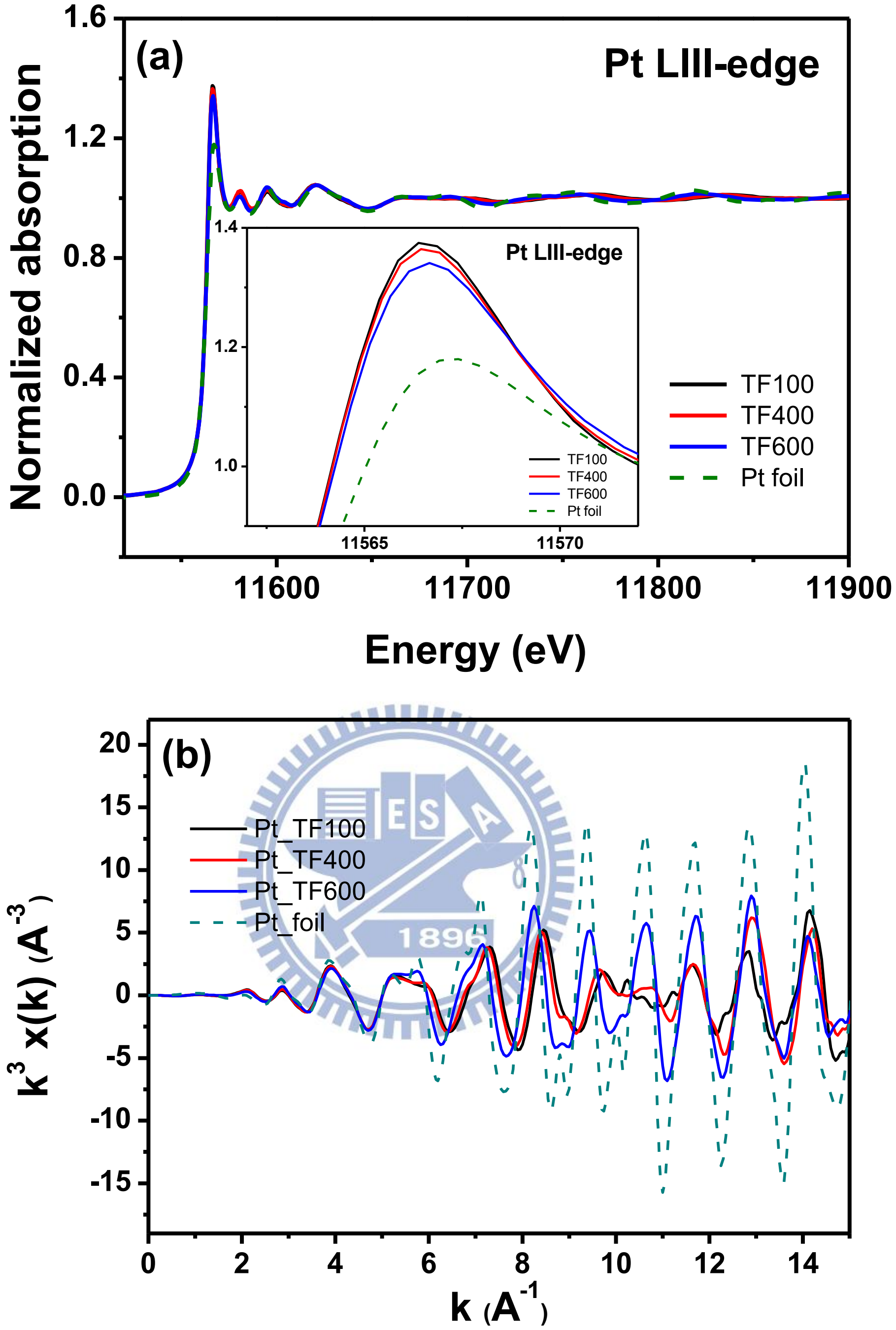

Figure 3.9 (a) The Pt L$_{\text{III}}$-edge XANES and EXAFS spectra and (b) the Pt L$_{\text{III}}$-edge k-space spectra for PtRu nanoparticles with different values of T_{off} (100, 400, and 600 ms) and fixed values of T_{on} (50 ms), J_{a} (50 mA/cm^2), and coulombic charge (8.0 C/cm^2), along with Pt foil serving as the reference in (b).

Fig. 3.9 (b) displays the Pt L_{III}-edge k-space spectra for three samples, along with Pt foil serving as the reference. The phases of oscillation, i.e. the spectrum shapes, for three samples from TF100 to TF600 with prolonged T_{off}, revealed more resemblance to that of Pt foil. This indicates that the number of Pt-Pt bond increased with longer T_{off}. On the other hand, the amplitudes of oscillation for all three samples were much smaller than that of Pt foil, suggesting that nanoparticles contained fewer atoms with low coordination numbers as opposed to that of Pt foil.

Fig. 3.10 (a) demonstrates the Ru K-edge XANES spectra from PtRu nanoparticles with different T_{off}. The Ru K-edge involves the ionization of electrons from the 1s orbital. The inflection points of absorption for the three samples all close to 22117 eV, slightly increase with the metallic state value of Ru metal. So the Ru K-edge XANES spectra alone couldn’t provide distinctive information about the oxidation state or metallic state of Ru in three samples under different pulse deposition conditions.

Fig. 3.10 (b) displays the Ru K-edge k-space spectra for our samples, along with Ru metal serving as the reference. The phases of oscillation for the samples TF100 and TF400 were rather similar to that of Ru metal. However, the phase of oscillation for sample TF600 obviously deviated from that of Ru metal. This indicates that with a longer T_{off}, Ru-Ru bond is broken due to Ru dissolution in displacement reaction, leading to a higher possibility for the remaining Ru atoms to be bonded with Pt atoms. Consequently, the sample TF600 with the longest T_{off} demonstrated a larger number of Ru—Pt bond than the other two samples. On the other hand, the amplitudes of oscillation for all three samples were notably smaller than that of Ru metal, suggesting that nanoparticles contained fewer atoms with low coordination numbers than bulk Ru metal.

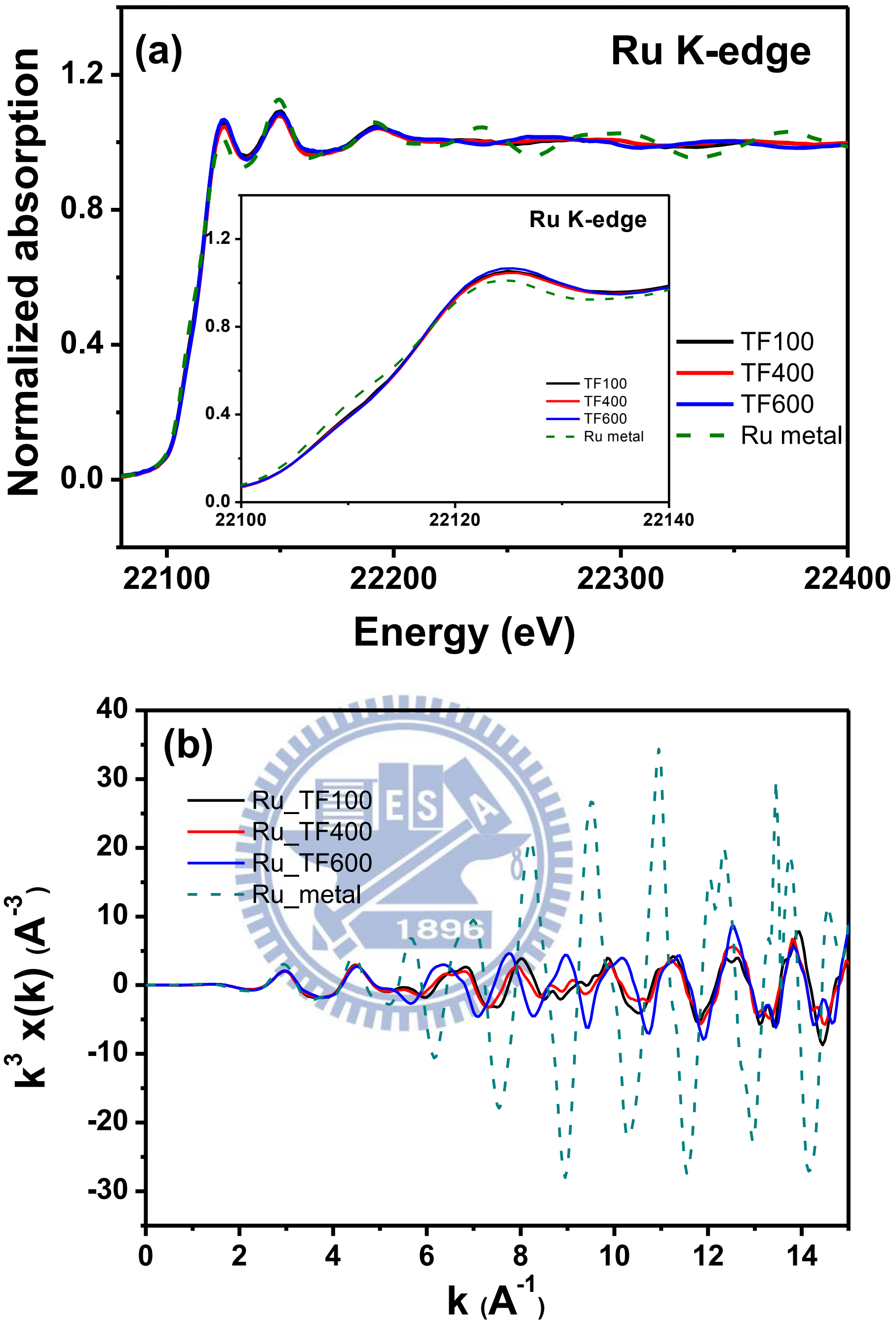

Figure 3.10 (a) The Ru K-edge XANES spectra and (b) the Pt K-edge k-space spectra for PtRu nanoparticles with different values of T_{off} (100, 400 and 600 ms) and fixed values of T_{on} (50 ms), J_a (50 mA/cm^2), and coulombic charge (8.0 C/cm^2), along with Ru metal serving as the reference in (b).

The k^3 weighted $\chi(k)$ data in k-space for the Pt L_{III}-edge (Fig. 3.9(b)) and Ru K-edge spectra (Fig. 3.10(b)) were Fourier-transformed to r-space. Fig. 3.11(a) shows the Pt L_{III}-edge Fourier-transformed EXAFS spectra. There were two obvious peaks for our samples. We surmised that the peak with a shorter bond distance (R) was associated with Pt-Ru bond, and the peak with a longer R was Pt-Pt bond, respectively. This is because at the first shell coordination with the Pt atom at the center, the Pt-Ru bond was reported to have a shorter bond distance than that of Pt-Pt bond[97, 98]. With a longer T_{off}, the amplitude of the peak associated with Pt-Ru bond became smaller and the amplitude of the peak associated with Pt-Pt bond became larger. This suggests that Pt atoms tended to form Pt-Pt bond rather than Pt-Ru bond after displacement reaction.

Fig. 3.11(b) shows the Ru K-edge Fourier-transformed EXAFS spectra. There were two notable peaks for our samples. We realized that the peak with a shorter bond distance (R) was associated with Ru-Ru bond, and the peak with a longer R was Ru-Pt bond, respectively. At the first shell coordination with the Ru atom at the center, the Ru-Ru bond was demonstrated to have a shorter bond distance than that of Ru-Pt bond[97, 98]. With a longer T_{off}, the amplitude for the peak associated with Ru-Ru bond became smaller and the amplitude for the peak associated with Ru-Pt bond became larger. This suggests that the Ru atoms tended to form Ru-Pt bond rather than Ru-Ru bond after displacement reaction. This fact is consistent with the result from Pt L_{III}-edge Fourier-transformed EXAFS spectra (Fig. 3.11(a)).

The EXAFS spectra (Fig. 3.11) in r-space were fitted by the data analysis package (Athena and Artemis) to analyze the coordination numbers between the center atom and the neighboring atoms. Fixed bond distances were employed for Pt-Ru bond ($R_{\text{Pt-Ru}} = 2.65$ A) and Pt-Pt bond ($R_{\text{Pt-Pt}} = 2.70$ A). The EXAFS fitting results are summarized in Table 3.9. The $N_{\text{Pt-Ru}}$ is the coordination number between the Pt center atom and the neighboring Ru atom. The P_{Pt} is the possibility for the Pt center atom to encounter a heterogeneous Ru atom. The equations for the calculation of P_{Pt} and P_{Ru} are as follows[99].

$$P_{Pt} = \frac{N_{Pt-Ru}}{\Sigma N_{Pt}} \qquad P_{Ru} = \frac{N_{Ru-Pt}}{\Sigma N_{Ru}}$$

Combining the spectra in k-space and r-space, and the fitting results, we conclude that in pulse current deposition, for Pt atoms at the center, with a longer $T_{\mathrm{off},}$ i.e. with a longer displacement reaction time, the Pt atomic ratio would become higher, the number for Pt-Pt bond would be larger and the number for Pt-Ru bond becomes smaller, and hence the possibility of P Pt is lower. On the other hand, for Ru atoms at the center, with a longer $T_{\mathrm{off},}$ i.e. with a longer displacement reaction time, the Ru atomic ratio would be lower, the number for Ru-Pt bond would become larger and the number for Ru-Ru bond would become smaller, and hence the possibility P_{Ru} is higher. In addition, during galvanic displacement reaction in pulse current electrodeposition, Pt ions react directly with Ru atoms, leading to effective deposition of Pt ions on the surface of nanoparticles and an increased numbers of Pt-Pt bond and Ru-Pt bond. While Ru atoms are oxidized to ions by releasing electrons and subsequently dissolve in electrolytes, leading to a decreased numbers of Ru-Ru bond and Pt-Ru bond. All these results strongly confirm that the displacement reaction between Ru atoms and Pt ions has occurred when the current was resting in pulse current electrodeposition.

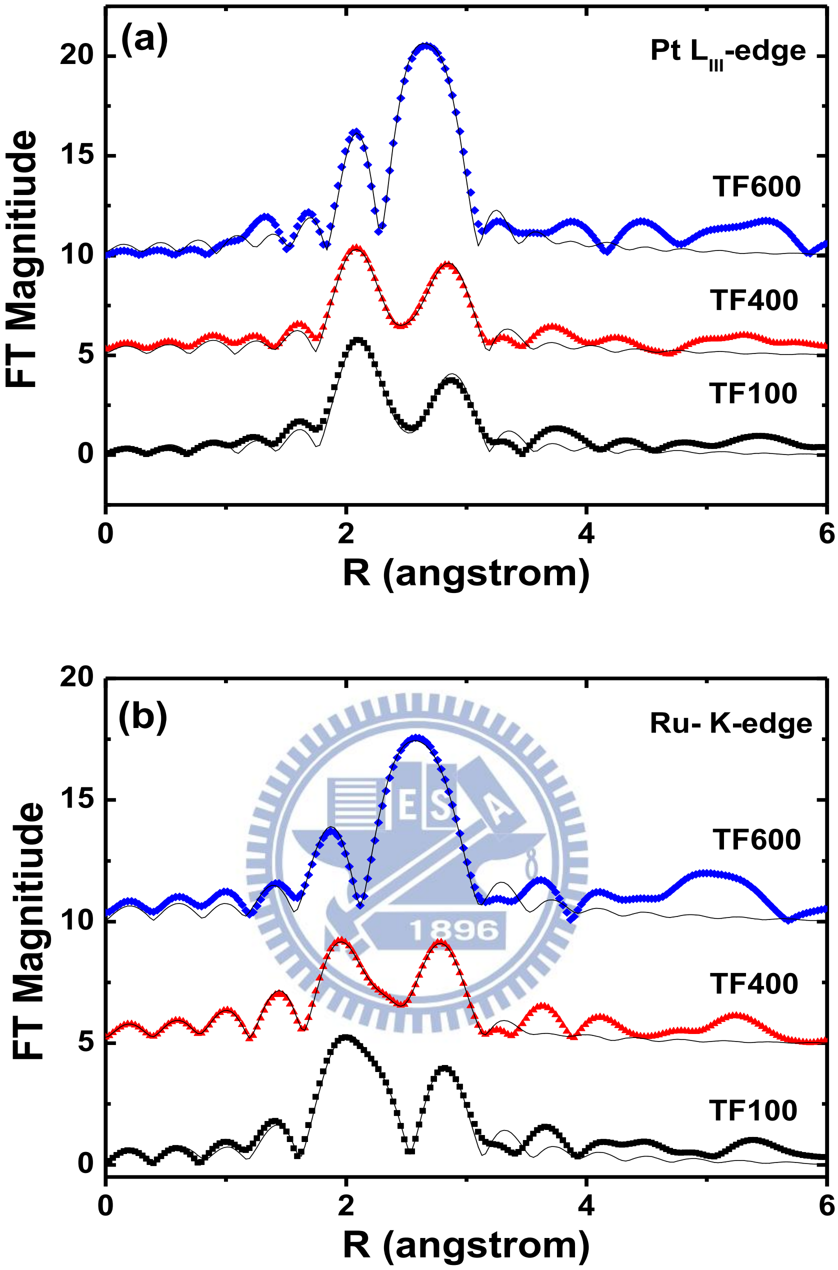

Figure 3.11 (a) The Pt L_{III}-edge and (b) the Ru K-edge Fourier-transformed EXAFS spectra for PtRu nanoparticles with different values T_{off} (100, 400 and 600 ms) and fixed values of T_{on} (50 ms), J_a (50 mA/cm^2) and coulombic charge (8.0 C/cm^2).

Table 3.9 EXAFS fitting parameters at Pt L_{III}-edge and at the Ru K-edge for PtRu nanoparticles with different values T_{off} (100, 400 and 600 ms) and fixed values of T_{on} (50 ms), J_a (50 mA/cm^2) and coulombic charge (8.0 C/cm^2).

	N_{Pt-Ru}	N_{Pt-Pt}	ΣN_{Pt}	N_{Ru-Pt}	N_{Ru-Ru}	ΣN_{Ru}	P_{Pt}	P_{Ru}	Pt (at%)	Ru (at%)
TF100	4.16	5.91	10.07	4.69	3.54	8.23	0.41	0.57	51.9	48.1
TF400	2.25	5.9	8.15	6.2	2.98	9.18	0.28	0.68	65.5	34.5
TF600	1.0	8.98	9.98	9.01	1.52	10.53	0.1	0.85	83.4	16.6

Furthermore, by comparing the values of ΣN_{Pt} and ΣN_{Ru} (Table 3.9), we can analyze the atomic distribution of bimetallic PtRu nanoparticles, and then determine which element was located at the core and which element was located in the shell. Ru atoms incorporating in the Pt lattice substituted some Pt atoms while the overall crystalline structure of PtRu nanoparticles remained the Pt-fcc structure. So the element with a larger total coordination number (ΣN) resided at the core, and the element with a smaller ΣN resided in the shell. Guided by this principle, we obtained the schematic diagrams for the cross sections of PtRu nanoparticles prepared by pulse current electrodeposition under different conditions (Fig. 3.12). For the sample TF100 with the short T_{off} and the high duty cycle, its ΣN_{Pt} was larger than ΣN_{Ru}, suggesting that the nanostructure was composed of the Ru-rich shell and the Pt-rich core. While for the sample TF600 with the long T_{off} and the low duty cycle, its ΣN_{Pt} was smaller than ΣN_{Ru}, suggesting that the nanostructure was composed of the Pt-rich shell and the Ru-rich core[99]. It is demonstrated that not only the elemental composition but also the atomic distribution of bimetallic PtRu nanoparticles can be effectively controlled and adjusted by the pulse current electrodeposition technique.

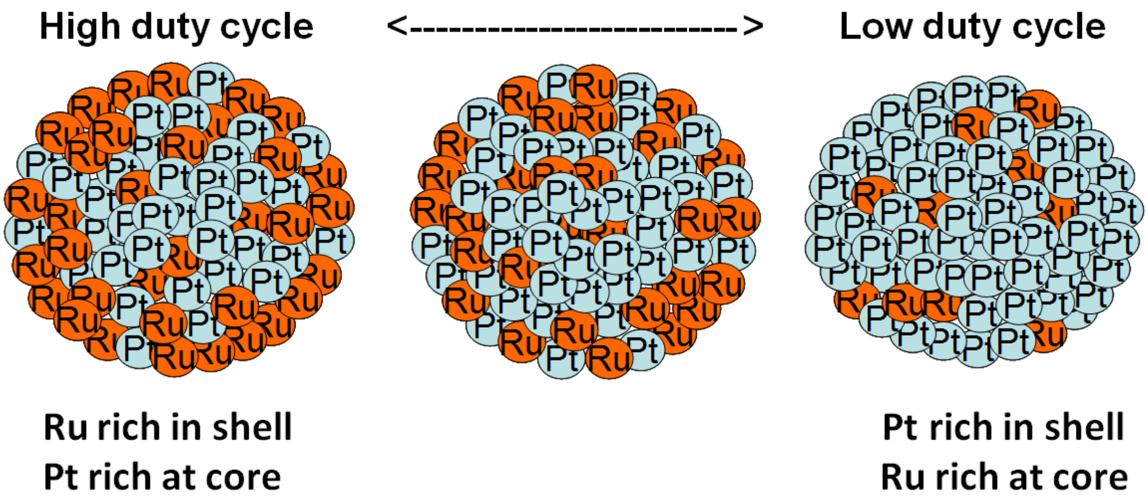

Figure 3.12 Schematic diagrams for cross sections of PtRu nanoparticles with different values T_{off} (100, 400 and 600 ms) and fixed values of T_{on} (50 ms), J_{a} (50 mA/cm^2) and coulombic charge (8.0 C/cm^2).

3.4 Conclusions

The pc depositions were employed to prepare PtRu nanoparticles on carbon cloths. Parameters including T_{on}, T_{off}, and J_{a} were explored to identify the optimized catalytic performances for methanol electro-oxidation. TEM images on the PtRu nanoparticles revealed a uniform distribution with moderate size variations. Measurements from ICP-MS indicated that a displacement reaction was occurring, resulting in the enrichment of Pt in the PtRu nanoparticles when the duty cycle was shortened. XRD analysis on the PtRu nanoparticles exhibited a slight shift of diffraction peaks, suggesting Ru was alloyed with Pt successfully. In addition, the alloyed Ru was found to decrease with reduced duty cycles. Analysis from XPS confirmed a steady loss of $RuO_2{\cdot}nH_2O$ from the particle surface when the T_{off} was prolonged. Furthermore, XANES and EXAFS analyses verified the occurrence of displacement reaction during T_{off} and suggested the structural evolution from Ru-rich shell to Pt-rich shell with diminished duty cycles. By the pulse current electrodeposition technique, the desired elemental composition and atomic distribution of PtRu nanoparticles were achievable and controllable.

Chapter 4 Investigation of Formation Mechanisms for PtRu Core-Shell Nanostructures during Galvanic Displacement by XAS and EQCM

4.1 Introduction

The development of bimetallic PtRu nanoparticles has received considerable attention recently because the PtRu is not only an effective electrocatalyst for methanol oxidation reaction (MOR) in direct methanol fuel cells (DMFCs) but also demonstrates impressive CO oxidation ability for reformate hydrogen fuel cells[8, 100, 101]. In DMFC, the oxidation of methanol entails consecutive removals of hydrogen that leaves a CO strongly bonded to the Pt, resulting in a gradual loss of MOR activity. This CO-induced performance degradation is known as CO poisoning which is particularly pronounced in Pt[102-106]. For the reformate hydrogen fuel cells, there is always minute presence of residual CO in the hydrogen feeds so it becomes a concern once the Pt is employed for hydrogen oxidation at the anode. To overcome the CO poisoning effect, the Ru is often alloyed with Pt to facilitate the oxidative removal of CO. It is realized that the Ru can either provide the oxygenated species for CO oxidation to CO_2 (bifunctional model) or alter the electronic structure of Pt so the CO-Pt bond strength is weakened considerably (ligand effect) [66, 67, 107]. In general, the catalytic performance of PtRu nanoparticles is determined by their size, morphology, crystallinity, composition, as well as the surface distribution of Pt and Ru. Since both Pt and Ru are precious metals, recent researches are steered toward the preparation of PtRu with reduced loading while still maintain desirable catalytic activities.

In general, the atomic arrangement of PtRu nanoparticles can be in alloy or core-shell (core@shell) structure, and both states reveal distinct catalytic performances and life time.[33, 43, 108] However, even in an alloyed PtRu there still exists considerable microsegregation on the surface composition so the Pt/Ru ratio on the surface is different from that of the core. For example, it is reported that the Ru has a larger heat of adsorption for O_2.[10, 109] Hence, under a O_2 heat treatment, the PtRu surface is enriched with Ru. On the contrary, the Pt exhibits a higher preference for H_2 and consequently a H_2 treatment engenders a Pt-rich surface instead.[10, 109] In contrast, the core-shell structure displays a well-defined regime for the respective core and shell components and the responsible mechanism for the CO oxidation involves the ligand model in which the shell element's electronic structure is altered by the core element underneath. In addition, because the catalytic shell element constitutes a relatively smaller amount as compared to the core element, the effective mass activity can be substantially increased.[4, 5, 110] Therefore, the material cost for electrocatalyst is expected to reduce greatly without compromising catalytic ability. To date, a variety of core-shell PtRu nanoparticles have been synthesized and evaluated with various successes. For instance, PtRu deposited on an inexpensive core such as PdCu@PtRu[5] and Co@PtRu[111] are reported with notable performance improvements. Alternatively, the Pt shell is deposited directly on a Ru core with thickness ranging from sub-monolayer to multiple layers forming a Ru@Pt structure.[34, 39, 97]

To fabricate Ru@Pt nanoparticles, the simplest synthetic scheme entails a displacement reaction which is also known in literature as redox-transmetalation reaction or spontaneous deposition.[25, 112] The displacement reaction often occurs in binary systems with constituents revealing distinct values of redox potentials. For example, CuNi, AgGe, and AuGe, have been demonstrated and their formation mechanisms are thoroughly discussed.[23, 76, 79] In principle, when a binary deposit is in contact with their respective cations in electrolyte, the constituent of less positive redox potential is dissolved from the deposit while the one with a higher redox potential is reduced from the electrolyte. Consequently, the deposit on the surface can be tailored for a desirable makeup which is likely different from that of bulk if the displacement reaction is carefully controlled. Since the Ru exhibits a higher redox potential than that of Pt, once the Ru is immersed in the electrolyte containing Pt cations, the Ru would undergo an oxidation reaction in conjunction with the reduction of Pt cations. Earlier, Brankovic et al. have studied the displacement reaction of $PtCl_6^{2-}$ on both single crystalline and nanoparticulate Ru.[24, 83, 84] They suggested that the driving force for the displacement reaction is the potential difference between the $PtCl_6^{2-}$ reduction and Ru^0 oxidation. In Ru single crystals, the Ru experiences a surface oxidation reaction forming $Ru(OH)_x$, or even a higher oxidized form. However, they pointed out that the redox potential for the corrosive dissolution of Ru is insufficient to reduce $PtCl_6^{2-}$, so they name this process a cementation reaction as well. In contrast, for Ru nanoparticles, both surface oxidation and corrosion dissolution are likely to provide necessary electrons for $PtCl_6^{2-}$ reduction.[24, 83, 84, 113] In addition to Ru, the nature of Pt on the PtRu nanoparticles is still under debate. From X-ray absorption spectroscopy (XAS), Manandhar et al. emphasized that the spontaneously-deposited Pt on the Ru core was Pt cations in intermediate oxidation states instead of metallic Pt.[24] However, similar XAS studies by Adzic et al. received different interpretations as they believed that the Pt exists in a metallic state and they attribute the observed d-band vacancy in Pt to the underlying Ru that alters the electronic structure of Pt above.[4]

Previously, Spieker et al. adopted the XAS to investigate the hydrolysis reaction of H_2PtCl_6 in an aqueous solution and identified the coordination environments of Pt cations in different pHs and Cl^- concentrations.[114] They determined that the $PtCl_6^{2-}$ is present only in an acidic solution with moderate excess of Cl^- or neutral solution with large excess of Cl^-. In contrast, the OH^- or H_2O would replace Cl^- as a complexing ligand in alkaline solution with reduced Cl^- content. It is rationalized that the type and number of ligands are critical in determining the activities for the cations. Therefore, any changeup in the number of H_2O, OH^-, and Cl^- ligand for the Pt cation is expected to affect its redox potential. Consequently, the extent of displacement reaction is likely varied once the Ru is immersed in $PtCl_6^{2-}$ solution at different pHs. This is a variable that is often overlooked by previous studies in PtRu displacement reaction.

In this work, we attempt to distinguish the effect of pH on the Pt complexes for Ru@Pt formation during the displacement reaction. The XAS is employed to provide a qualitative insight on the oxidation states and coordination environments for both Pt and Ru in electrolytes and Ru@Pt nanoparticles. Materials characterizations including XRD, TEM, and ICP-MS are conducted and correlated with results of CO oxidative ability and life time performance from electrochemical analysis.

4.2 Experimental

Functionalization of commercial carbon black Vulcan XC-72R

Functionalization of commercially available carbon black Vulcan XC-72R (XC72) was conducted by immersing the as-received XC72 in a solution of sulfuric acid (97 wt%) and nitric acid (61 wt%) at a 3:1 volume ratio for 1 h at 25˚C, followed by washing and drying at 80˚C to obtain dry powders. The purpose for this acid treatment was to improve the adhesion of chemically reduced Ru nanoparticles by providing suitable functional groups on the XC72 surface[6].

Fabrication of XC72-supported Ru nanoparticles

Ru nanoparticles were impregnated onto the functionalized XC72 via a chemical reduction method. First, 0.2 g $RuCl_3$ (99.9 wt%) and 0.8 g functionalized XC72 were mixed in excess de-ionized water to form a stable suspension. Subsequently, an appropriate amount of $NaBH_4$, serving as the reducing agent, was dissolved in de-ionized water and slowly added to the $RuCl_3$/XC72 mixture. At this stage, the Ru^{3+} was reduced to form Ru nanoparticles evenly supported on the XC72 matrix (designated as Ru/XC72). Afterward, the Ru/XC72 was filtered and washed by de-ionized water, followed by 80˚C drying in oven to remove residual solvent.

Sample preparation of Ru@Pt nanoparticles

To carry out the displacement reaction with Pt cations, the Ru/XC72 powders were deposited on a carbon cloth (CC) of 2×2 cm^2 which was employed as a substrate. We adopted an ink method in which the ink suspension was composed of 8 mg Ru/XC72, 5 mg PTFE (30 wt%), and 5 mL 99.5 wt% ethanol. The ink suspension was well-dispersed by ultrasonication for 30 min and was transferred to the CC atop a hot plate at 80˚C. After drying out residual solvent, the sample, designated as Ru/XC72/CC, was immersed in 5 mM aqueous solution of hexachloroplatinic acid (H_2PtCl_6; 99.9 wt%) at selective pH values. The intrinsic pH value for the 5 mM H_2PtCl_6 aqueous solution was 2.2, and it was adjusted to pH 1 by perchloric acid ($HClO_4$) and pH 8 by potassium hydroxide (KOH), respectively. The immersion lasted for 24 h at 40˚C, allowing sufficient replacement of Pt for Ru. The as-prepared samples were thoroughly rinsed with de-ionized water and were designated as “group A”. A second set of samples undergoing a hydrogen reduction treatment after the immersion in H_2PtCl_6 solution at identical pH conditions was labeled as “group B”. The hydrogen reduction was conducted with pure hydrogen at 80˚C for 2 h. Samples after the immersion in H_2PtCl_6 solution were designated as Ru@Pt/XC72/CC because the Pt cations were expected to deposit on the Ru nanoparticles forming a Ru core and Pt shell structure. For comparison purposes, we also immersed the Ru/XC72/CC in solutions of $HClO_4$ (pH 1), deionized water (pH 7), and KOH (pH 8) to evaluate the chemical stability of Ru/XC72/CC in those environments and the amount of Ru that was corrosively dissolved. A flow chart for the preparation steps involved is depicted in Fig. 4.1.

Materials characterizations

X-ray diffraction (XRD) patterns were obtained by Max Science-M18XHF KXY-8019-1 with a Cu K_α of 1.54 Å. The X-ray diffractogram was recorded at a scan rate of 4 degree/min for 2θ values between 30° and 90°. To distinguish the crystalline state of Ru@Pt, we also carried out XRD analysis for 2θ values between 36° and 41° at 0.5 degree/min. Transmission electron microscopy (TEM) was employed to observe the morphology for the as-prepared Ru and Ru@Pt nanoparticles using JEOL JEM-3000F with an accelerating voltage of 300 kV. The XC72-supported Ru and Ru@Pt nanoparticles were carefully removed from the CC after rinsing in ethanol followed by ultrasonication. We also obtained the PtRu ratio with an energy-dispersive X-ray spectroscopy (EDX) equipped on the TEM. The exact Pt and Ru amount for the Pt and Ru@Pt nanoparticles was determined by an inductively coupled plasma mass spectrometry (ICP-MS) where samples of

Ru/XC72/CC and Ru@Pt/XC72/CC were dissolved in a solution containing HCl, HNO_3, and HF of 2:2:1 volume ratio at 180˚C. In addition, we retrieved liquid samples from the H_2PtCl_6 solution after the displacement reaction to validate the concentration of remaining Pt and dissolved Ru cations.

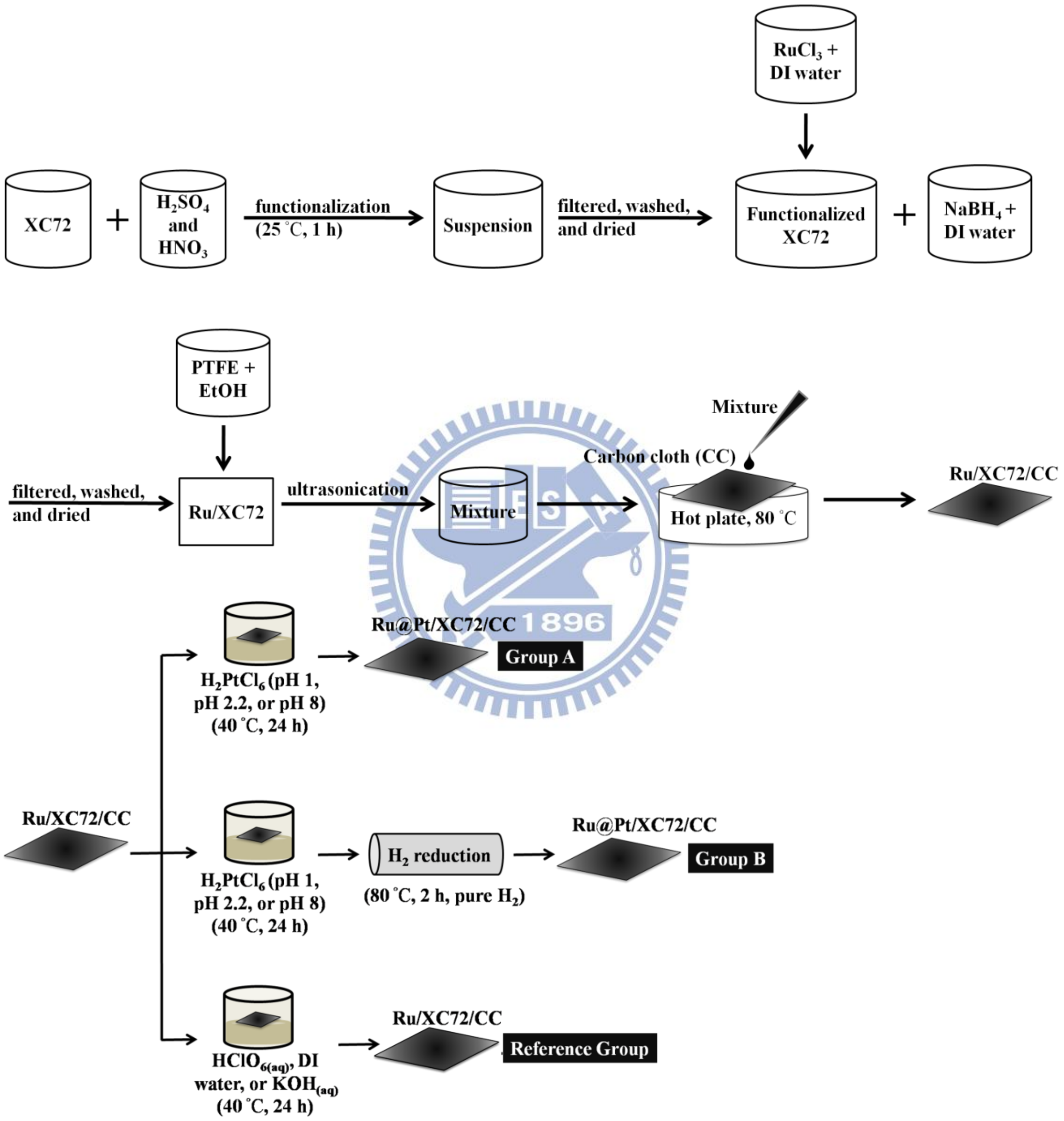

Figure 4.1 A flow chart for the processing steps involved to prepare samples of group A, group B and reference group

XAS measurements and analysis

X-ray absorption spectra (XAS) for the Pt L_{III}-edge (11,564 eV) and Ru K-edge (22,117 eV) were obtained at beamlines BL01C1 and BL17C1 of the Taiwan Light Source, National Synchrotron Radiation Research Center (NSRRC), Hsinchu, Taiwan. The storage ring energy was 1.5 GeV, and the stored current was in the range of 300-360 mA. A double Si(111) crystal monochromator was adopted for energy selection with a resolution $\Delta E/E$ better than 2×10^{-4} at both beamlines. Rh or Pt-coated mirrors were adopted to reject high-order harmonics, collimate (upstream) and refocus (downstream) the X-ray beam. The XAS measurements were conducted in a fluorescence detection mode at 25˚C. A Lytle fluorescence detector along with three gas-filled ionization chambers were used to measure the intensities of the X-ray fluorescence photons from the sample (I_f), incident beam (I_0), transmitted beam through the sample (I_t), and transmitted beam through the reference metal foil or powder (I_r). A Pt foil was served as a reference for Pt L_{III}-edge measurements and metallic Ru powder was used for Ru K-edge measurements.

Extended X-ray absorption fine structure (EXAFS) data analysis and fitting were processed by IFEFFIT 1.2.11c data analysis package (Athena, Artemis, and FEFF6)[115, 116]. In each scan, the recorded data were calibrated by aligning against the reference. After the calibration, they were averaged to achieve better signal quality. X-ray absorption near edge structure (XANES) spectra were acquired after normalization by Athena software. The EXAFS function was obtained by standard protocols including pre-edge and post-edge background subtraction, and normalization with respect to the edge jump. The detailed procedure has been reported elsewhere[117]. The resulting EXAFS function, $\chi(E)$, was transformed from the energy space to k-space. The value k refers to the photoelectron wave vector. At the high k-region of $\chi(k)$ data, multiplication by k^3 was adopted to compensate the damping of EXAFS oscillations. Next, the k^3 weighted $\chi(k)$ data were Fourier-transformed to r-space. Specific ranges in k-space for the Fourier transformation were selected from 3.32 to 12.74 Å^{-1} for the Pt L_{III}-edge and from 4.01 to 13.42 Å^{-1} for the Ru K-edge.

The EXAFS curve fitting in *r*-space was applied by a nonlinear least-square algorithm. In addition, the *r*-space ranges for the curve fitting were established without phase correction from 1.29 to 3.12 Å for Pt and from 1.32 to 2.73 Å for Ru. The structural parameters were fitted by Artemis with theoretical standards generated by FEFF6 code[118]. The fitted structural parameters included the coordination number (*N*), bond distance (*R*), Debye–Waller factor ($\Delta\sigma_j^2$), and inner potential shift (ΔE_0). Two assumptions were made in the EXAFS fitting for the H_2PtCl_6 solution. First, we assumed that the Pt cation (IV) complexes were octahedrally coordinated, which kept the sum of Pt-Cl and Pt-O coordination number at six for all complexes. Second, the difference in $\Delta\sigma_j^2$ for the Pt-Cl and Pt-O was assumed to be identical[114]. In addition, the amplitude reduction factor (S_0^2) for Ru was obtained by analyzing the reference Ru powder and found to be 0.79.

4.3 Results and discussion

4.3.1 Materials characterizations on Ru@Pt/XC72/CC

The XRD patterns are able to provide qualitative evidences for the PtRu displacement reaction since the Pt and Ru adopt distinctive lattices of fcc and hcp, and the alloying of a relatively larger Pt atom (1.35 Å) into Ru (1.3 Å) structure is expected to render a slight expansion in lattice parameter. Fig. 4.2(a) exhibits the XRD patterns for the XC72/CC, Ru/XC72, Ru/XC72/CC, and group A of Ru@Pt/XC72/CC from H_2PtCl_6 solution of pH 1, pH 2.2, and pH 8, respectively. As shown, the XC72/CC exhibited an amorphous background with a notable diffraction peak at 43.62°. This peak was also present for remaining samples in Fig. 4.2(a) and it is a characteristic carbon signal as evidenced by many studies.[119-122] For the Ru/XC72, the hcp phase of Ru was confirmed with relevant planes properly indexed. In addition, the XRD pattern suggested a polycrystalline structure with relative intensity consistent with that of JCPDS 06-0663. The observed stronger signals for the Ru/XC72 over those of Ru/XC72/CC were attributed to the sample preparation difference where a larger amount of Ru/XC72 was used for XRD measurement. For samples of Ru@Pt/XC72/CC, the only discernible diffraction peaks were (100) and (101) which were associated with the Ru lattice. Since the (101) overlapped with the background diffraction from the XC72 and CC, we repeated the XRD measurements at a slower scan rate around the (100) peak for comparison. The high-resolution XRD pattern for 36°-41° is displayed in Fig. 4.2(b). As shown, the Ru/XC72/CC revealed a (100) peak at 38.74°. For samples of pH 1, pH 2.2, and pH 8, the (100) peak was located at 38.7°, 38.5°, and 38.82°, respectively. The minor variation between these diffraction peaks was likely caused by poor crystallinity of Ru after displacement reaction as well as background noises from the XC72 and CC that compromised signal quality considerably. We believed that the possibility for PtRu alloying was rather remote as the displacement reaction took place at 40˚C and any interdiffusion between Pt and Ru was unlikely. Hence, the formation of core-shell Ru@Pt was presumed because from the standpoint of displacement reaction, the Pt was deposited upon removal of Ru and this dislocation process was occurring on the Ru surface exclusively. According to Alayoglu et al., for Ru@Pt nanoparticles with an approximately 1-2 monolayer-thick Pt shell, both hcp Ru and fcc Pt diffraction peaks were observed, albeit with considerable noises and reduced crystallinity.[108] In our case, unfortunately, the Pt signal was not identified form Fig. 4.2(b). Earlier, Manandhar and Kelber studied the spontaneous deposition of Pt on Ru(0001) single crystals by X-ray photoelectron spectroscopy and confirmed that the Pt was partially reduced as Pt(II) cations on the Ru surface.[24] Therefore, it is likely that the Pt might exist in an oxidized form instead of metallic one in our case after the displacement reaction.

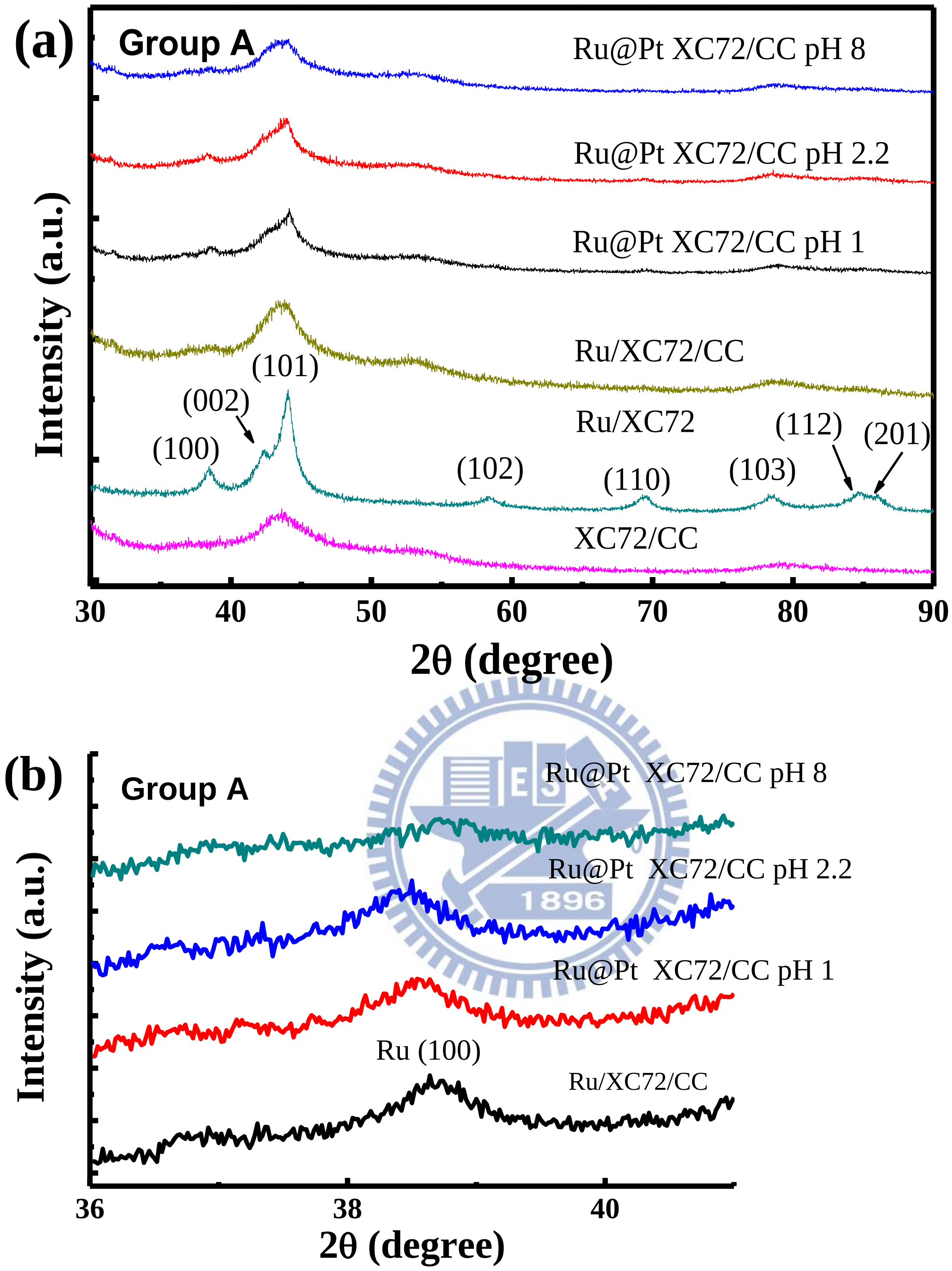

Figure 4.2. The XRD patterns for the XC72/CC, Ru/XC72, Ru/XC72/CC, and Ru@Pt/XC72/CC from group A of pH 1, pH 2.2, and pH 8 in scan range of (a) 30°–90° and (b) 36°–42°.

To validate our premise that the Pt was not present in metallic state after the displacement reaction, we carried out the hydrogen reduction treatment and Fig. 4.3(a) demonstrates the XRD patterns for Ru@Pt/XC72/CC from samples of group B. Similar to what we observed in Fig. 4.2(a), a broad diffraction peak was recorded around 44° which was attributed to the combined effects of XC72/CC and Ru (101). Fig. 4.3(b) provides the high-resolution XRD pattern for 36°-42°. For samples of pH 1, pH 2.2, and pH 8, the Ru (100) peak was located at 38.5°, 38.54°, and 38.62°, respectively. These peaks were orderly shifted to lower angles as compared to that of Ru/XC72/CC at 38.74°. This suggested a moderate alloying of Pt in Ru matrix after the hydrogen reduction treatment. In addition, the degree of alloying increased with baths at smaller pH value. Moreover, for samples of pH 2.2 and pH 8, there appeared a minor diffraction peak of Pt (111) at 39.48° corresponding to a fcc Pt with a lattice parameter of 3.95 Å. This value was slightly larger than the bulk Pt of 3.92 Å which was unexpected because the underlying Ru core is presumed to exert finite constrains for the Pt lattice above, causing it to shrink its lattice parameter slightly. However, we rationalized that the signals from CC and XC72 might interfere with diffraction responses from the Pt so the peak location might lose its fidelity. Nevertheless, we concluded that the Pt was present initially in some oxidized forms but transformed to metallic one after the hydrogen reduction treatment.

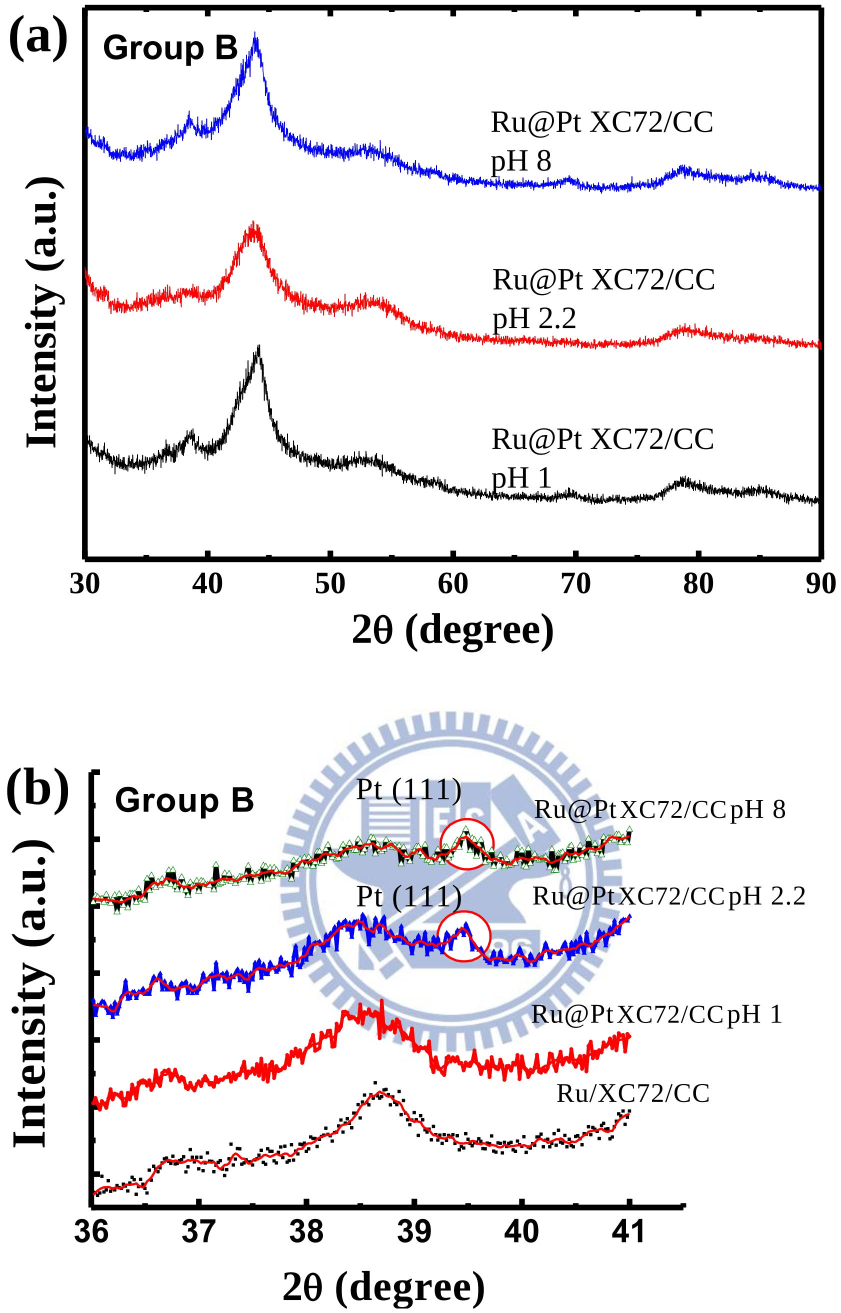

Figure 4.3. The XRD patterns for the Ru@Pt/XC72/CC from group B of pH 1, pH 2.2, and pH 8 in scan range of (a) 30°–90° and (b) 36°–42°.

The TEM images for Ru/XC72 and Ru@Pt/XC72 (group A) of pH 1, pH 2.2, and pH 8 are exhibited in Fig. 4.4. Also displayed in the insets are their respective pictures in high magnification. As shown in Fig. 4.4(a), the Ru nanoparticles were irregular but uniformly distributed in the XC72 support with an average size of 3.6 nm. The high-resolution image confirmed a polycrystalline structure for each individual particle. Interestingly, their sizes were slightly increased after the displacement reaction from the TEM images in Fig. 4.4(b-d). The average size for the Ru@Pt nanoparticles of pH 1, pH 2.2, and pH 8 was 4, 3.8, and 4.6 nm, respectively. However, their morphologies were similar to that of Fig. 4.4(a). This minute variation in sizes between each group suggested that the Ru nanoparticles were rather stable in various environments against corrosive dissolution. This behavior was not unexpected as Pourbaix diagram predicted similar behaviors. In addition, due to the coulombic balance during the displacement reaction, the loss of Ru introduces deposition of Pt that rendered the Ru@Pt at similar sizes Moreover, results from EDX, listed in Table 4.1, confirmed the presence of Pt after the displacement reaction. The bath of pH 1 revealed the largest amount of Pt, followed by pH 2.2 and pH 8, indicating that the acidic environment was favored for Pt deposition or adsorption. These results were consistent with the XRD patterns in Fig. 4.3(b) since at pH 1 and pH 2.2, some of the Pt were alloyed with Ru so a relatively larger amount of Pt was reasonably expected.

Table 4.1. EDX results on Ru@Pt/XC72 from group A of pH 1, pH 2.2, and pH 8.

	Ru (at%)	Pt (at%)
pH 1	88.92	11.08
pH 2.2	93.35	6.65
pH 8	96.62	3.38

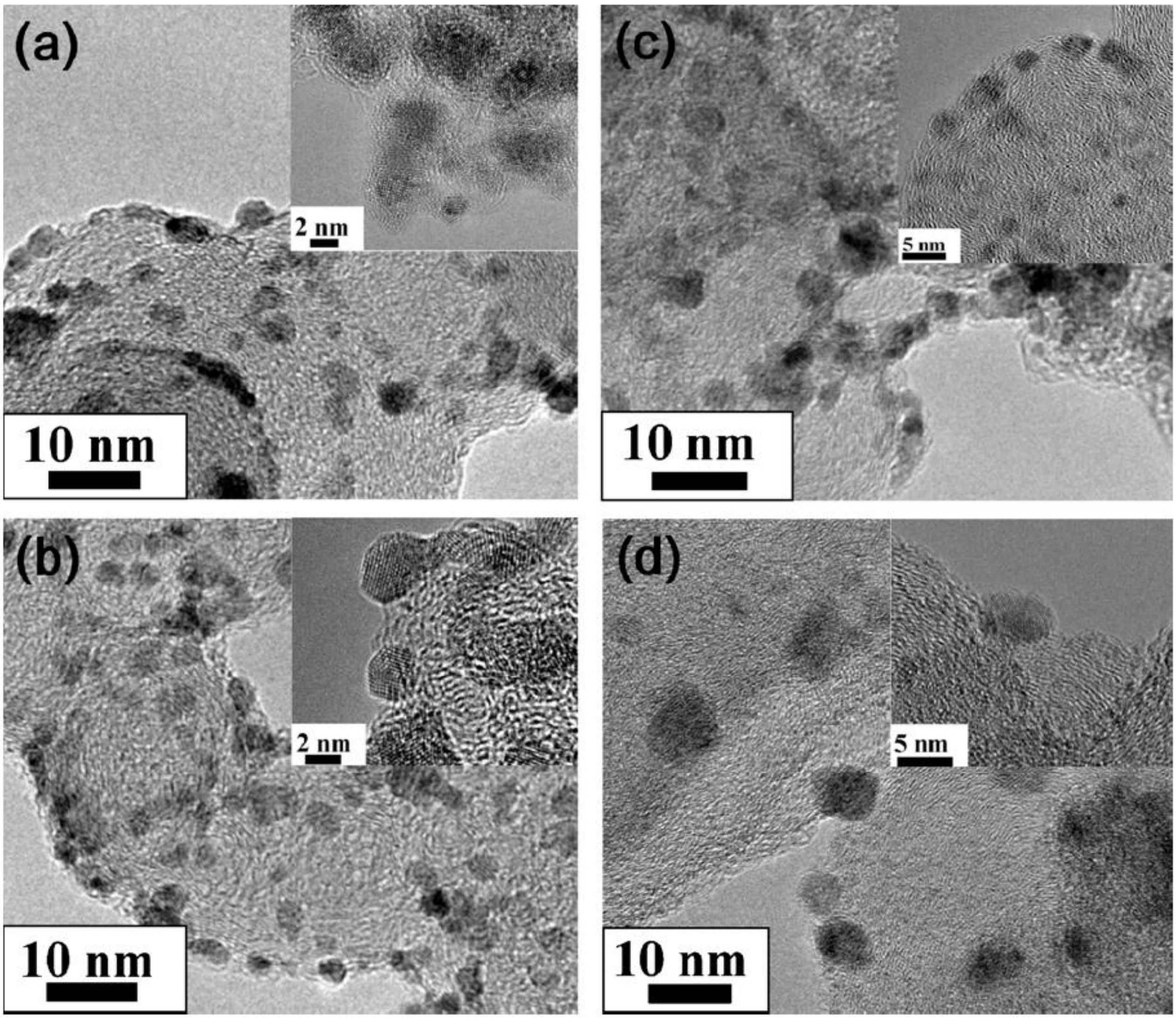

Figure 4.4. The TEM images for (a) Ru/XC72 and Ru@Pt/XC72/CC from group A of (b) pH 1, (c) pH 2.2, and (d) pH 8. The insets are their respective mages in high resolution.

Since the EDX results provided qualitative evidences at best, more accurate reading for the Pt and Ru amount after the displacement reaction was obtained via ICP-MS. Table 4.2 presents the ICP-MS results for the Ru@Pt/XC72 from group A of pH 1, pH 2.2, and pH 8, as well as their corresponding H_2PtCl_6 solution after the displacement reaction. As listed, the Pt loading was 1.26, 1.17, and 0.62 μmole for samples of pH 1, pH 2.2, and pH 8, respectively. Apparently, a lower pH bath allowed more Pt deposition or adsorption on the remaining Ru nanoparticles, a behavior consistent with EDX results in Table 4.1. Likewise, the Ru loading was 2.02, 2.94, and 4.86 μmole for samples of pH 1, pH 2.2, and pH 8, respectively. For the corresponding H_2PtCl_6 solution, the amount of residual Pt at various pH values agreed well with what we expected. In addition, the amount of Ru cations in the H_2PtCl_6 solution was proportional to the Ru loss in Ru@Pt nanoparticles. Obviously, considerable Ru dissolution in conjunction with Pt deposition was observed at a low pH bath. From Table 4.2, the composition for the Ru@Pt nanoparticles was $Pt_{38}Ru_{62}$, $Pt_{28}Ru_{72}$, and $Pt_{11}Ru_{89}$ for samples of pH 1, pH 2.2, and pH 8, respectively.

In order to remove possible effect of Ru corrosion encountered in the acidic electrolyte, we also obtained ICP-MS results from samples of Ru/XC72/CC immersed in aqueous solution of pH 1, pH 7, and pH 8 (reference group). Since the Pt cations were not present in the solution, the amount of Ru recorded in the solution was caused entirely by corrosive dissolution instead of displacement reaction. The Ru amount in pH 1, pH 7, and pH 8 bath was 0.31, 0.01, and 0.03 μmol, respectively. It can be seen that the Ru suffered from moderate corrosion in pH 1 bath but became relatively stable in pH 2 and pH 8 bath. Nevertheless, the amount of corrosive dissolution of pH 1 bath was still insufficient to account for the Ru content reported in Table 4.2. According to the Pourbaix diagram, the Ru is expected to be in a metallic state at 0 V for bath of pH 1, pH 2, and pH 8. Hence, we concluded that the observed displacement reaction was not driven by the corrosive dissolution of Ru but initiated by the difference in the redox potentials between the Ru and Pt complexes at different pH baths. According to Brankovic et al.[83], the driving force *(ΔU)* for the displacement reaction is the potential difference between the $[PtCl_6]^{2-}$ reduction and Ru oxidation as shown in equations below.

$$\Delta U = \Delta E_{Pt/PtCl_6^{2-}} - \Delta E_{Ru^0/Ru_{oxidized}} > 0 \tag{1}$$

$$\left[PtCl_6\right]^{2-} + 4e^- = Pt^0 + 6Cl^- \tag{2}$$

$$(\Delta E[V] \sim 0.74 + 0.015\log\left[PtCl_6\right]^{2-}) \tag{3}$$

$$Ru^0 + x(H_2O) = RuO_xH_y + (2x-y)H^+ + (2x-y)e^- \tag{4}$$

In addition, it is believed that the oxidative dissolution of Ru occurs at a potential more positive than the equilibrium potential of $Pt/[PtCl_6]^{2-}$ so it is unlikely to trigger the displacement reaction.[123]

Table 4.2. ICP-MS results on Ru@Pt/XC72/CC from group A of pH 1, pH 2.2, and pH 8, as well as their corresponding H_2PtCl_6 solution.

		Pt (μmol)	Ru (μmol)
Ru@Pt/XC72/CC	pH 1	1.26	2.02
	pH 2.2	1.17	2.94
	pH 8	0.62	4.86
H_2PtCl_6 solution	pH 1	20.01	1.88
	pH 2.2	21.61	1.37
	pH 8	22.57	0.05

4.3.2 XANES and EXAFS analysis

Since the activity for Pt complexes and their associated redox potentials are determined by the nature and number of ligands, the solution pH value therefore becomes very critical because the hydrolysis of Pt complexes is highly pH-dependant. The nature and number of ligand around the Pt cation in the electrolyte, as well as the oxidation state for Pt and Ru in the Ru@Pt nanoparticles can be inferred from XANES and EXAFS analysis. The Ru K-edge XANES spectra for the reference group (Ru/XC72/CC in pH 1, pH 2, and pH 8 solution) are demonstrated in Fig. 4.5, along with Ru and RuO_2 serving as the reference. The metallic Ru is established to have a K-edge absorption around 22,117 eV and its position is shifted to higher energy in oxidized state, as confirmed by the RuO_2. Spectra from the Ru/XC72/CC after immersing in $HClO_4$ (pH 1), de-ionized water (pH 7), and KOH (pH 8) suggested that some of the Ru existed in oxidized forms and their oxidation states were rather similar. However, the exact oxidation state was still unknown but its value was estimated between 0 and +4 as indicated by the absorption edge between Ru and RuO_2. According to literature, the Ru was prone to form surface oxide and hydroxide when it was immersing in a liquid electrolyte. Hence, presence of Ru in an oxidized state was not entirely unsupported.[124]

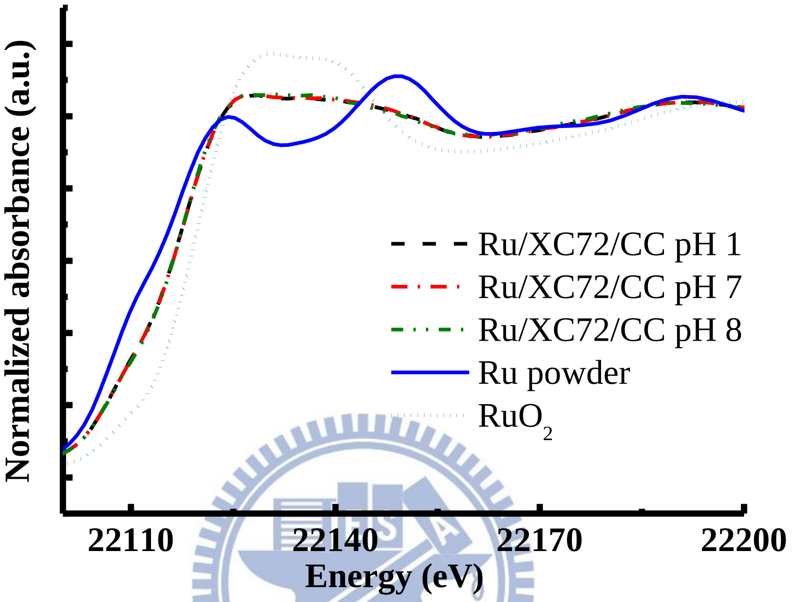

Figure 4.5. The Ru K-edge XANES spectra of Ru, RuO_2, and Ru/XC72/CC from reference group of pH 1, pH 7, and pH 8.

Fig. 4.6 exhibits the Ru K-edge XANES spectra for samples from group A and group B, respectively. In general, their spectra were similar to those obtained in Fig. 4.5. Hence, we concluded that the oxidation state of Ru remained unchanged regardless the electrolyte they encountered was $HClO_4$, KOH, or H_2PtCl_6. However, after further exploration, as shown in the inset of Fig. 4.6, it was found that the Ru from group A was slightly more oxidized than that in group B. This behavior was not unexpected as the samples from group B underwent a hydrogen reduction treatment leading to their reduced oxidized state. It is noted that from XRD in Fig. 4.2 and Fig. 4.3, the samples from group A and group B did not reveal the presence of RuO_x or $Ru(OH)_x$. However, in the XANES spectra, the Ru existed in an oxidized state anyway. We attributed this discrepancy to the sensitivity of XANES that took into consideration of both metallic Ru at the core and oxidized Ru on the surface. Besides, the oxidized Ru was likely amorphous that obscured the XRD signal.

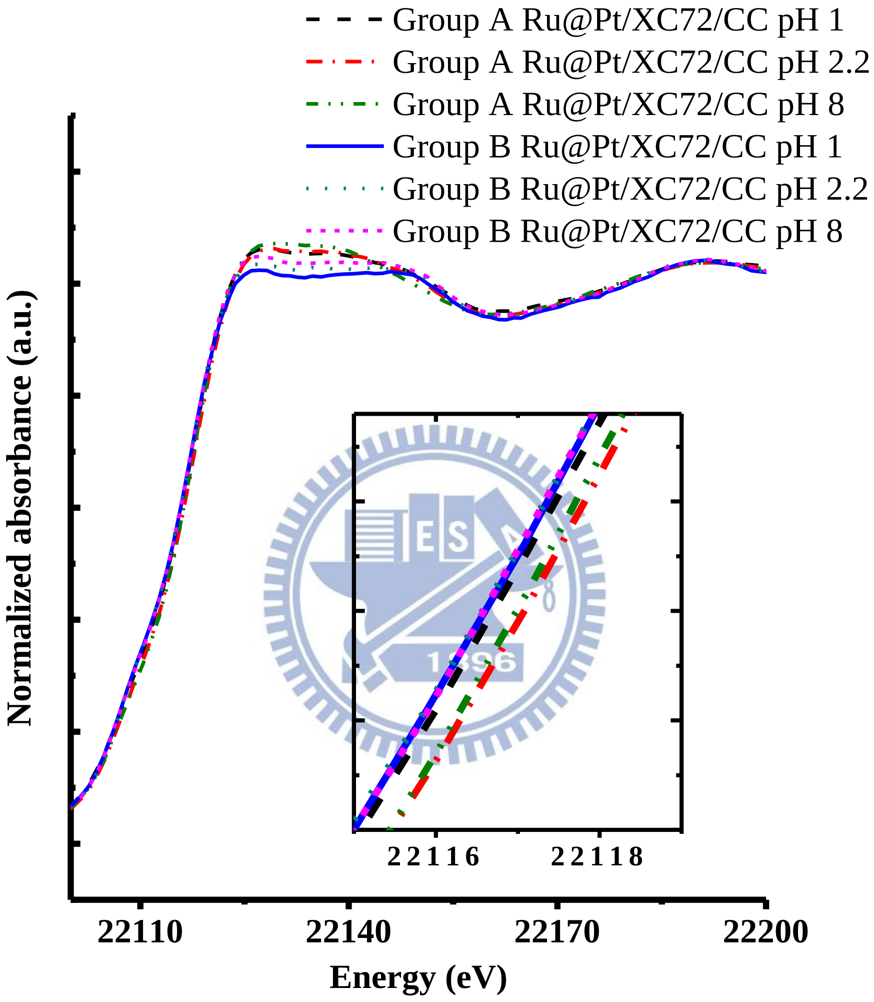

Figure 4.6. The Ru K-edge XANES spectra of Ru@Pt/XC72/CC from group A and group B.

Similarity in Fig. 4.5 and Fig. 4.6 confirmed that the Ru maintained an identical oxidation state with or without displacement reaction. Therefore, during displacement reaction, we believed that the oxidized Ru left the surface in the form of dissolved complexes and freshly-exposed Ru adopted a similar oxidation state. To confirm our premise, it is necessary to carry out XANES analysis on the electrolyte to verify the identity of dissolved Ru cations. Unfortunately, the Ru cations in the electrolyte after displacement reaction was so dilute that validation of their identity became rather difficult. From samples of group B, the oxidation state for Ru was not completely reduced to metallic form which suggested that the oxidized Ru state we observed was intrinsic to Ru after the Ru was exposed to electrolyte or ambient moisture.

The Ru K-edge Fourier-transformed EXAFS spectra for the reference group, group A, and group B are provided in Fig. 4.7. The peaks at 1.6 Å and 2.3 Å (without phase correction) were associated with Ru-O bond and Ru-Ru bond at the first shell coordination. The EXAFS fitting results are summarized in Table 4.3. For the reference group, the coordination number for Ru-O in all baths was around 2. This bonding between Ru and O was attributed to the formation of oxide or hydroxide on the Ru surface. On the other hand, the Ru-Ru coordination number was around 4-5, which was expected because earlier studies by Huang et al. reported a similar coordination number for Ru nanoparticles.[25] For the Ru@Pt/XC72/CC (sample of group A), we obtained a reduced Ru-O coordination number for pH 1 and pH 2.2 bath. On the other hand, the coordination number of Ru-Ru remained unchanged suggesting that the Ru core was likely intact. However, the EXAFS fitting did not reveal any Ru-Pt bond which excluded the possibility of Pt sitting next to Ru in the Ru@Pt nanoparticles. Nevertheless, once the hydrogen reduction treatment was imposed (as shown in group B), the Ru-Pt coordination number of 1.33, 1.08, and 0.82 was obtained for pH 1, pH 2.2, and pH 8 bath, respectively. At the same time, the number of Ru-O bond became smaller due to the hydrogen reduction treatment. Likewise, the Ru-Ru bond remained relatively unchanged because the Ru core was mostly unaffected. Based on previous work by Hu et al.[125], the Ru might form a Ru-O-Ru bonding near its surface. In our case, the bridged oxygen was likely to connect both Pt and Ru forming a Ru-O-Pt. As a result, the Ru-O-Pt was formed instead of Ru-Pt on the surface of Ru nanoparticles. Hence, it became reasonable that the Ru-Pt coordination was established as long as the bridged oxygen was removed during hydrogen reduction treatment.

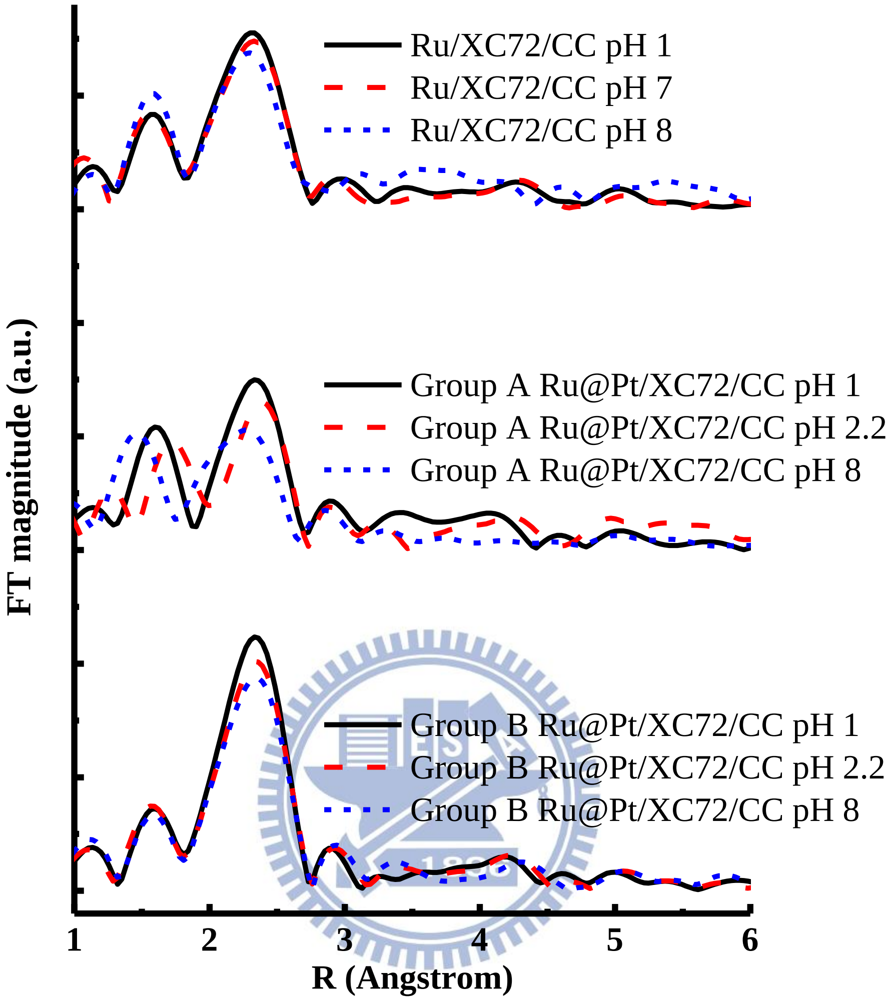

Figure 4.7. The Ru K-edge Fourier-transformed EXAFS spectra from Figs. 4.4 and 4.5.

Fig. 4.8 demonstrates the Pt L_{III}-edge XANES spectra for H_2PtCl_6 at pH 1, pH 2.2, and pH 8, respectively. Also shown is the XANES for Pt foil. The purpose for this measurement is to determine the nature of complexing ions for the Pt cations in different environments. From literature, electronic transitions from $2p_{3/2}$ to 5d is responsible for the Pt L_{III}-edge which is also known as white line.[126, 127] In general, the white line intensity is able to provide information on the oxidation state of Pt due to its relevance to the d-band vacancy. A larger white line intensity often infers more vacant d-band orbitals. From the XANES spectra, there appeared a high intensity white line for the Pt cations in H_2PtCl_6 solution at various pH values. These patterns were expected as the Pt cations were possibly present in Pt^{4+}. For the white line of Pt foil, its low intensity confirmed its metallic nature and its magnitude corresponded to the oxidation state of “0”.

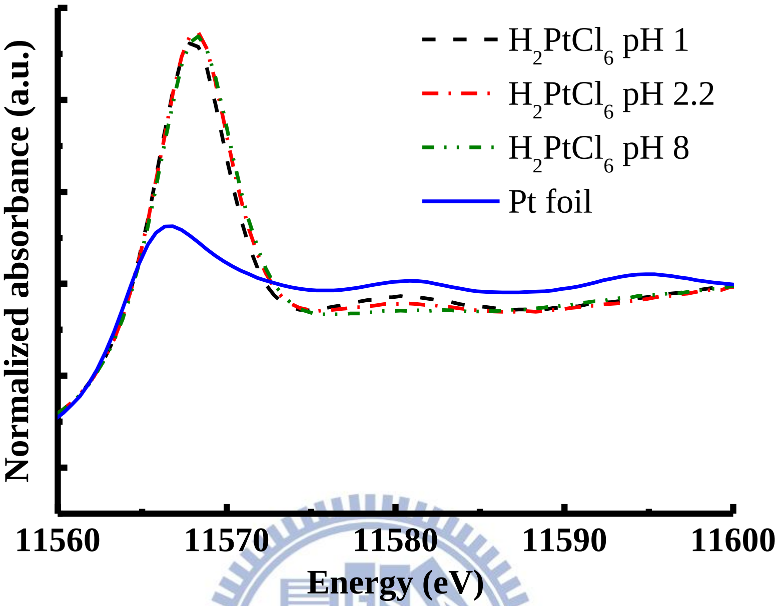

Figure 4.8. The Pt L_{III}-edge XANES spectra of Pt foil and H_2PtCl_6 solution of pH 1, pH 2.2, and pH 8.

Table 4.3. EXAFS fitting parameters at the Ru K-edge for Ru/XC72/CC and Ru@Pt/XC72/CC under various conditions.

		Path	Coordination number, N	Bond distance, R (Å)	Inner potential shift, ΔE_0 (eV)	Debye-Waller factor, $\Delta\sigma_j^2$ ($\times 10^{-3}$ Å^2)
Reference	pH 1	Ru-O	1.95	2.04	-5.45	5.43
		Ru-Ru	4.61	2.67	-9.92	7.29
	pH 7	Ru-O	1.99	2.04	-4.36	5.41
		Ru-Ru	5.00	2.67	-10.4	7.98
	pH 8	Ru-O	1.94	2.04	-6.15	3.32
		Ru-Ru	4.15	2.67	-12.05	7.45
Group A	pH 1	Ru-O	1.23	2.05	-0.55	0.13
		Ru-Ru	4.06	2.67	-7.35	7.02
	pH 2.2	Ru-O	1.33	2.07	-1.56	0.46
		Ru-Ru	4.28	2.68	-7.10	8.26
	pH 8	Ru-O	1.99	2.02	-7.46	1.78
		Ru-Ru	4.08	2.65	-12.88	7.03
Group B	pH 1	Ru-O	1.07	2.05	-6.54	4.23
		Ru-Ru	5.24	2.69	-3.71	6.70
		Ru-Pt	1.33	2.71	-9.44	5.91
	pH 2.2	Ru-O	1.36	2.05	-5.03	5.30
		Ru-Ru	5.12	2.69	-4.14	7.20
		Ru-Pt	1.08	2.70	-13.59	6.62
	pH 8	Ru-O	1.41	2.05	-0.47	6.96
		Ru-Ru	4.54	2.69	-3.62	6.91
		Ru-Pt	0.82	2.71	-8.24	5.64

For the identity of Pt atoms which were deposited onto Ru after the displacement reaction, the Pt L_{III}-edge XANES spectra in Fig. 4.9 can provide insightful information. In general, for samples from group A and group B, the XANES spectra clearly demonstrated a notable distinction in which signals from group A revealed a larger d-band vacancy than those from group B. This trend was expected as samples from group B underwent a hydrogen reduction treatment. For samples of group A, obviously the pH 8 sample revealed the largest d-band vacancy with its magnitude close to the H_2PtCl_6 solution in Fig. 4.9. This suggested that the Pt existed in +4 oxidation state on the Ru particle after the displacement reaction which inferred a physical adsorption process without involving the oxidation loss of Ru. In addition, for baths of pH 1 and pH 2, it appeared that the Pt still existed in the oxidized state albeit with a slightly reduced state. This trend was reversed from samples of group B in which the pH 8 sample demonstrated the lowest oxidative state with magnitude close to the metallic Pt foil shown in Fig. 4.8. However, the samples from pH 1 and pH 2.2 indicated that the Pt was present at a slightly oxidized state. We surmised that at pH 8 the Pt atoms clustered around themselves revealing a metallic behavior while at pH 1 and pH 2.2, the Pt atoms were intermixed with Ru forming a quasi-alloying state instead. Earlier, it was suggested by Sasaki et al. that in alloying of PtRu the Pt exhibits a larger d-band vacancy because its electronic structure is influenced by nearby Ru[4]. This might be another possible reason accountable for the recorded oxidized Pt in Fig. 4.9. An alternative explanation is that the RuOx is able to withdraw electrons partially from the Pt nearby leading to relatively stronger white line intensities.

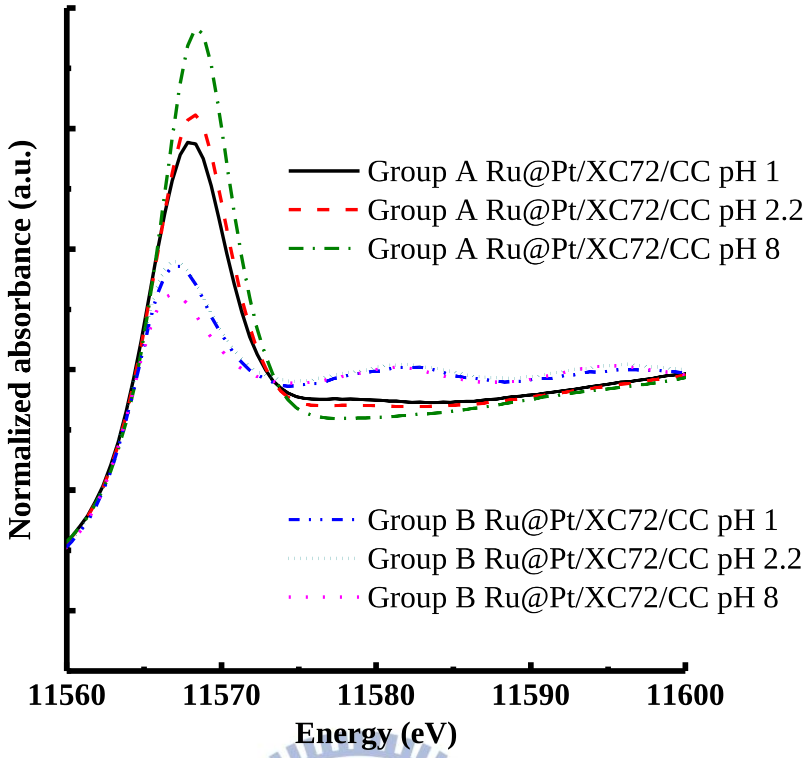

Figure 4.9. The Pt L_{III}-edge XANES spectra of Ru@Pt/XC72/CC from group A and group B.

The Fourier-transformed EXAFS spectra for H_2PtCl_6, group A, and group B are exhibited in Fig. 4.10. As shown, the peaks at 1.7 Å and 2.0 Å (without phase correction) were associated with the Pt-O bond and Pt-Cl bond at the first shell coordination, respectively. On the other hand, the peaks at 2.1 Å and 2.7 Å (without phase correction) corresponded to the Pt-Ru bond and Pt-Pt bond at the first shell coordination, respectively. The EXAFS fitting results are summarized in Table 4.4. In H_2PtCl_6 solution, the coordination number of Pt-O was 1.31, 1.65, and 3.58 for pH 1, pH 2.2, and pH 8 bath, respectively. In addition, the EXAFS results determined that the coordination number of Pt-Cl was 4.69, 4.35, and 2.42 for pH 1, pH 2.2, and pH 8 bath, respectively. Previously, Spieker et al., in their careful study of dilute H_2PtCl_6 acid with various pH values, observed that the chloride ion ligands associated with the Pt complexes can be exchanged by hydroxide ligand (OH) or aquo ligand (OH_2) due to the hydrolysis reaction.[114] Similar phenomena were observed in this work in which the EXAFS fitting for samples of different pHs indicated a significant ligand changeup between the Pt-Cl and Pt-O coordination number. In other words, the number of chloride ligands on the Pt complexes was reduced due to the hydrolysis reaction when the pH value was increased. The variation of Pt ligand species was believed to be responsible for the notable difference toward the behavior of displacement reaction.

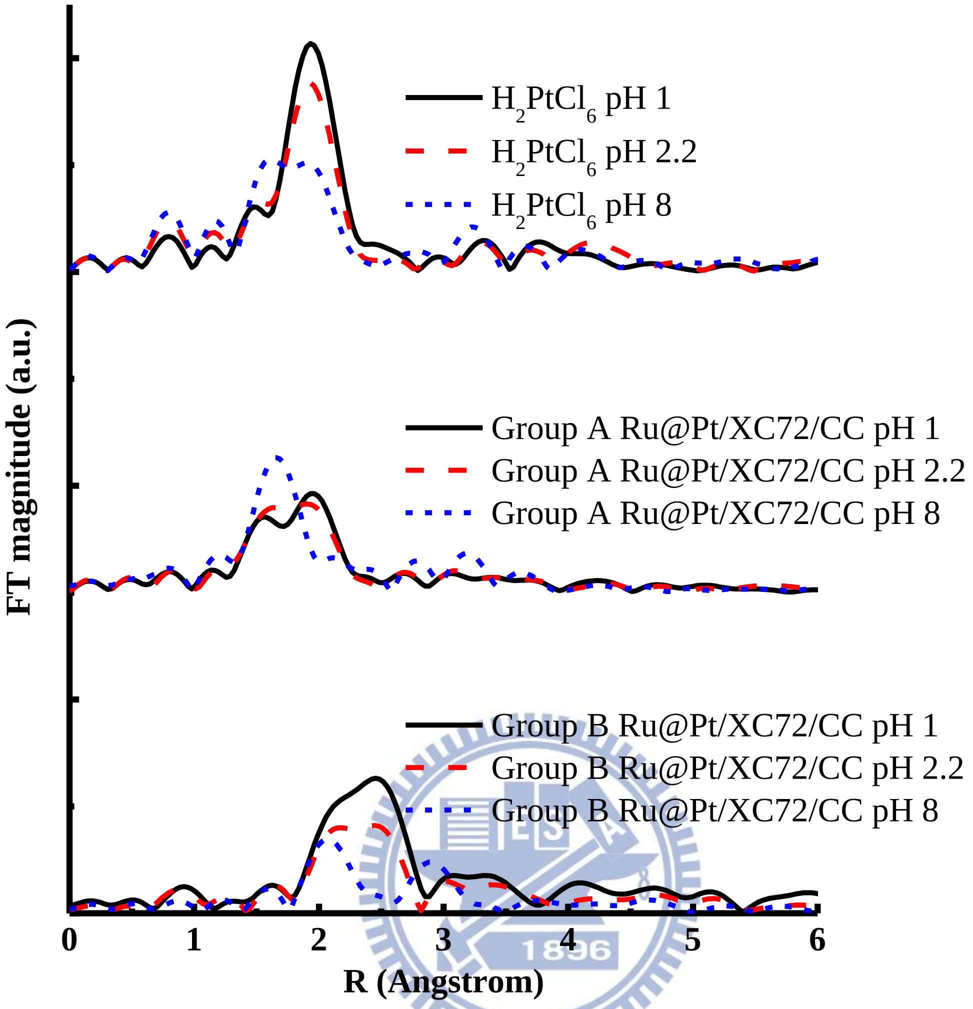

Figure 4.10. The Pt L_{III}-edge Fourier-transformed EXAFS spectra from Figs. 4.8 and 4.9.

For group A, the sum of coordination number for Pt-O and Pt-Cl was decreased after the deposition/attachment to the Ru. This indicated that some of the ligands were removed from the Pt complexes when the Pt cations were anchored to Ru. Nevertheless, a direct Pt-Ru bond was not established which was consistent with what we found in Table 4.4. Therefore, the bridged oxygen structure was believed to be the linkage between the Pt and Ru. For samples in group B, the coordination environment was changed dramatically with the disappearance of Pt-O and Pt-Cl. Instead, we witnessed the formation of Pt-Ru and Pt-Pt. The coordination number for Pt-Ru was 5.75, 4.23, and 3.21 for pH 1, pH 2.2, and pH 8 bath. These results suggested that at low pH value, the Pt atoms were embedded in the Ru core occupying lattice sites vacated by dissolving Ru atoms. At a high pH value, the Pt cations were merely adsorbed physically on the Ru surface which led to a decrease in the Pt-Ru coordination number after the hydrogen reduction treatment. On the other hand, the coordination number for Pt-Pt was 1.71, 2.43, and 4.24 for pH 1, pH 2.2, and pH 8 bath, respectively. At a low pH value, the Pt atoms were assumed to mix with Ru forming a quasi-alloying state that resulted in a small Pt-Pt coordination number. On the contrary, the Pt clusters on the Ru surface were expected to exist for the pH 8 bath. These results were consistent with XRD data in Fig. 4.3, leading to a larger Pt-Pt coordination number.

Table 4.4. EXAFS fitting parameters at the Pt L_{III}-edge for Ru/XC72/CC and Ru@Pt/XC72/CC under various conditions.

		Path	Coordination number, N	Bond distance, R ($\AA$)	Inner potential shift, ΔE_0 (eV)	Debye-Waller factor, $\Delta\sigma_j^2$ ($\times 10^{-3}$ $\AA^2$)
H_2PtCl_6 Solution	pH 1	Pt-O	1.31	1.99	-2.14	2.79
		Pt-Cl	4.69	2.31	10.16	2.79
	pH 2.2	Pt-O	1.65	1.99	-1.95	3.77
		Pt-Cl	4.35	2.31	10.34	3.77
	pH 8	Pt-O	3.58	1.99	1.44	4.21
		Pt-Cl	2.42	2.31	13.83	4.21
Group A	pH 1	Pt-O	1.95	1.99	7.26	1.78
		Pt-Cl	1.69	2.30	9.16	1.57
	pH 2.2	Pt-O	1.83	2.00	7.79	1.79
		Pt-Cl	2.41	2.30	8.80	4.47
	pH 8	Pt-O	3.66	1.99	3.73	2.42
		Pt-Cl	1.83	2.32	18.35	11.17
Group B	pH 1	Pt-Ru	5.75	2.71	8.66	5.61
		Pt-Pt	1.71	2.76	7.52	2.96
	pH 2.2	Pt-Ru	4.23	2.71	7.69	5.60
		Pt-Pt	2.43	2.76	8.65	4.82
	pH 8	Pt-Ru	3.21	2.71	6.69	6.25
		Pt-Pt	4.24	2.75	7.26	4.66

We have also examined the oxidation state of Ru ions after galvanic displacement reaction by XAS. During the displacement reaction, the metallic Ru atoms were oxidized by the $PtCl_6^{2-}$ ions, and became Ru ions. The carbon-supported Ru nanoparticles, with additional treatment of hydrogen reduction at 100 ˚C for the removal of surface oxide, were immersed in the aqueous 80 mM H_2PtCl_6 solution at 30 ˚C for 24 hours, followed by filtering of the suspension. The electrolyte contained dissolved Ru ions and excess H_2PtCl_6 were studied by XAS measurements. As shown in Fig. 4.11, by comparing the Ru K-edge XANES spectra of Ru ions, with those of Ru metal, Ru/C, $RuCl_3$(aq) and RuO_2(s), it is noted that the inflection point of absorption curve for the Ru ions was very close to that of $RuCl_3$(aq) but not of RuO_2(s). This suggested that the valence of Ru ions is smaller than +4 . Also it is known that Ru^{2+} ions are not able to exist in a stable state in aqueous solution. We determine that the valence of Ru ions after displacement reaction is +3. And therefore the PtRu galvanic displacement reaction for Ru nanoparticles in aqueous H_2PtCl_6 solutions can be expressed as

$$3PtCl_6^{2-}+4Ru^0 \rightarrow 3\ Pt^0+ 4Ru^{3+} + 18\ Cl^- \qquad (4.5)$$

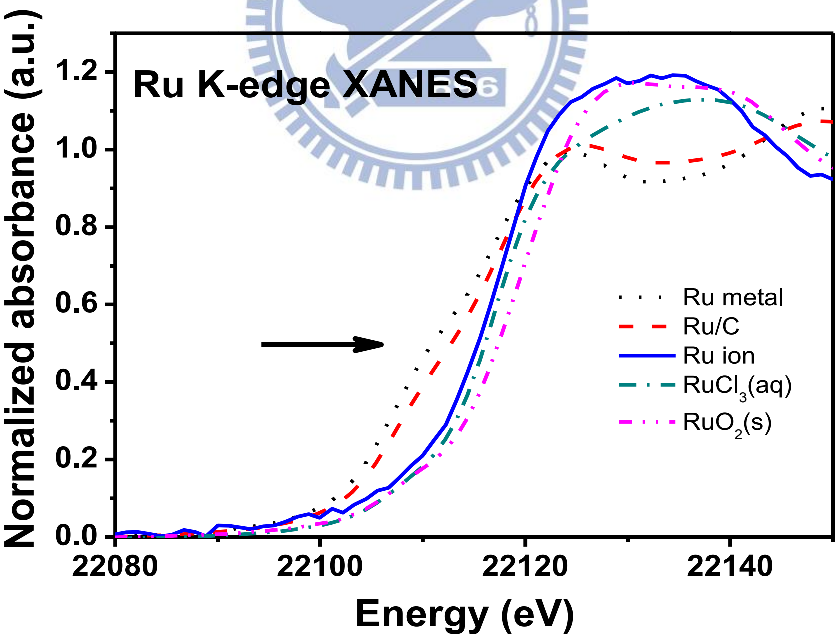

Figure 4.11 The Ru K-edge XANES spectra of Ru ions after displacement reaction, along with Ru metal, Ru/C, $RuCl_3$(aq) and RuO_2(s) serving as references.

By summarizing the analytical results from XRD, ICP-MS, TEM, EDX, and XAS spectra, a mechanism for the Pt displacement reaction on the Ru nanoparticles is provided in the schematic diagrams shown in Fig. 4.12. Fig. 4.12(a) depicts the scenario for pH 1 and pH 2 in which the Pt cations were partially reduced accompanied by the oxidative dissolution of Ru on the surface. The dissolution of Ru was likely resulted from Pt reduction. Meanwhile, the formation of Ru oxide layer on the surface took place slowly during the immersion into aqueous baths which eventually terminated the displacement reaction as the surface oxide layer prevented the underneath Ru from further dissolving and consequently inhibiting the reduction of Pt ions. Fig. 4.12(b) illustrates the mechanism of PtRu displacement reaction in pH 8 scenario. The Pt cations were physically adsorbed on the Ru surface mostly, and after the hydrogen reduction treatment, the Pt cations were reduced and agglomerated as clusters on the Ru surface. In short, the pH values of H_2PtCl_6 acid played a critical role for the extent of displacement reaction between the Pt and Ru and its resulting alloy state. Furthermore, two factors should also be considered. They were the various ligands around the Pt complexes and extent of Ru dissolution in acidic/basic aqueous solvents. The deposition for Pt on the Ru was formed through the bridged oxygen instead of direct Pt-Ru bonding.

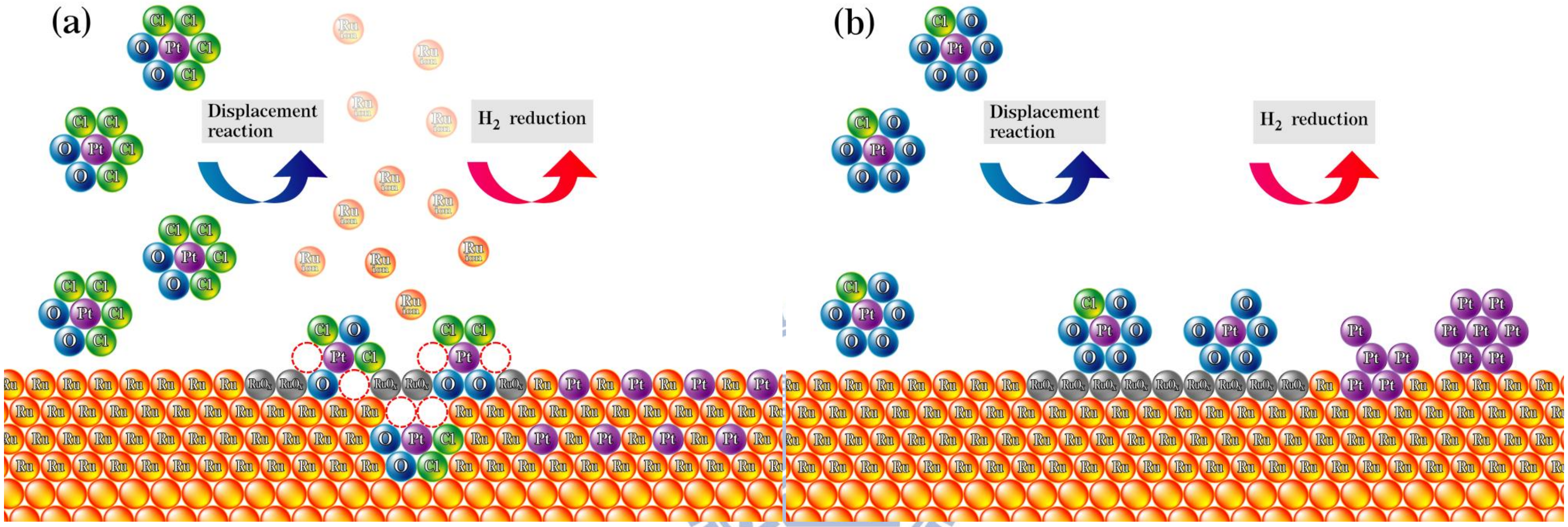

Figure 4.12. Schematic diagrams for PtRu displacement reaction occurring at (a) low pH and (b) high pH conditions.

4.3.3 Electrochemical analysis of Ru@Pt/XC72/CC

An alternative route to confirm the core-shell structure for the Ru@Pt nanoparticles is to carry out CO stripping experiments on the samples after hydrogen reduction treatment (group B). Since the CO is known to form a strong chemical bonding with Pt that deactivates the Pt from subsequent electrochemical actions, the modification of Pt by underlying Ru has been reported to alleviate the CO poisoning effect via a mechanism of electronic modification.[66, 67] As a result, the Ru@Pt nanoparticles are expected to reveal superior performances for CO oxidation and this can be easily seen by the negative shift of the onset potential in CO stripping measurements. To carry out the CO stripping experiments, we saturated 0.5 M H_2SO_4 solution with gases of 3 vol% CO and 97 vol.% N_2 for 30 min at -0.15 V (vs. Ag/AgCl) to ensure adequate adsorption of CO on the Ru@Pt/XC72/CC. Afterward, cyclic voltammetric scans (CV) were imposed on the samples for -0.2~0.9 V to obtain current responses associated with CO oxidation. The resulting CV profiles are displayed in Fig. 4.13. Also shown for comparison is the commercial PtRu from E-TEK. Apparently, the E-TEK PtRu exhibited an onset potential of 0.23 V, while the Ru@Pt nanoparticles of pH 1, pH 2.2, and pH 8 displayed an onset potential of 0, 0.02, and 0.04 V, respectively. The improvements in the onset potentials for the CO stripping provided additional evidences of core-shell formation in our samples. In addition, the sample of pH 1 revealed the lowest onset potential because its surface structure was between alloyed and core-shell arrangement that revealed the largest ligand effect.

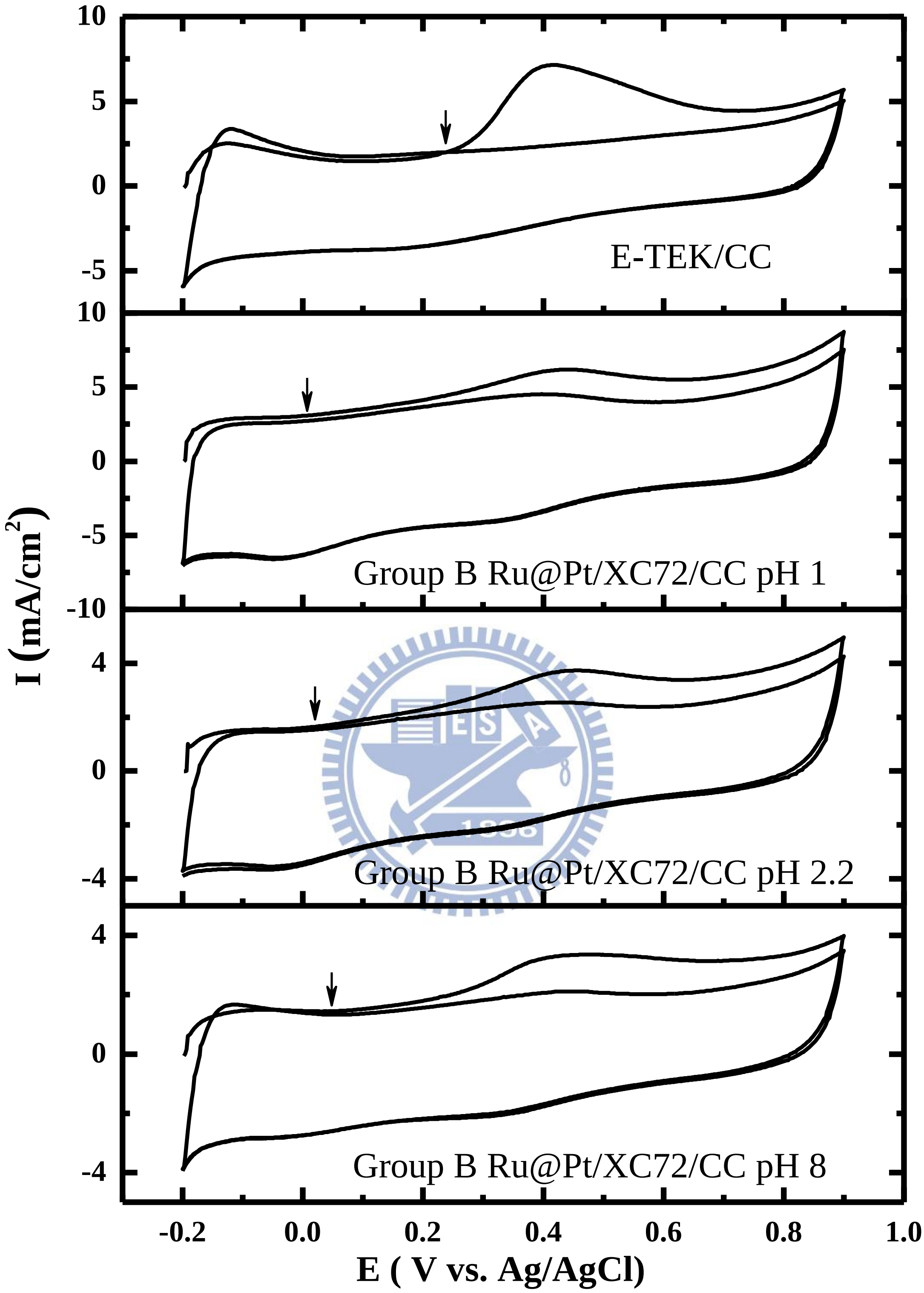

Figure 4.13. The cyclic voltammetric curves for CO oxidation on E-TEK/CC and Ru@Pt/XC72/CC from group B of pH 1, pH 2.2, and pH 8.

Tolerance for CO poisoning can also be confirmed by subjecting the Ru@Pt nanoparticles (group B) in mixed gas of $H_2/N_2/CO$ (200/9.7/0.3 in vol. ratio) for H_2 oxidation reaction. The experiments were performed at 0.05V (vs. Ag/AgCl) in 0.5M H_2SO_4 solution for 1 h to record the resulting current responses. Fig. 4.14 demonstrates the H_2 oxidation curves for both apparent current density and mass activities in which identical trends were observed. In general, the obtained current revealed moderate instability which was caused by gas bubble adsorption and desorption. These undesirable current fluctuations were also observed by Brankovic et al. and Adzic et al..[12, 34] For the E-TEK PtRu, there appeared a gradual loss in the H_2 oxidation ability which agreed with earlier results.[34] They attributed this degradation behavior to the CO poisoning of Pt. A similar pattern was also witnessed for Ru@Pt nanoparticles of pH 8 which was possibly due to the formation of Pt clusters on the Ru surface that exposed unalloyed Pt for Pt-CO bonding. In contrast, the Ru@Pt nanoparticles of pH1 demon strated an increasing catalytic ability for H_2 oxidation initially but stabilized after 1000 s with negligible performance degradation. This notable improvement further substantiated the formation of desirable core–shell structure that enabled facile CO removal as evidenced in Fig. 4.13. It is noted that the in situ XAS would be very insightful to detect any changeup in Pt or Ru during fuel cell operation when the electrode is under polarization. In a recent article by Zhou et al., they carried out the in situ XAS on Pd_2Co-supported Pt monolayer for the oxygen reduction reaction and observed that the white line intensity of the Pt L_{III}-edge did not show any noticeable change until the applied potential was positive of 0.9V.[15] In our case, the potential for the hydrogen oxidation reaction occurred at 0.25V so it is likely that the in situ XAS for the hydrogen oxidation reaction might not pick up sufficient variation in the white line intensity of Pt L_{III}-edge. However, there is also possibility that the Ru would become Ru oxide or hydroxide at 0.25V and hence alters the electronic structure of Pt nearby. In such scenario, the Pt L_{III} white line might be slightly affected.

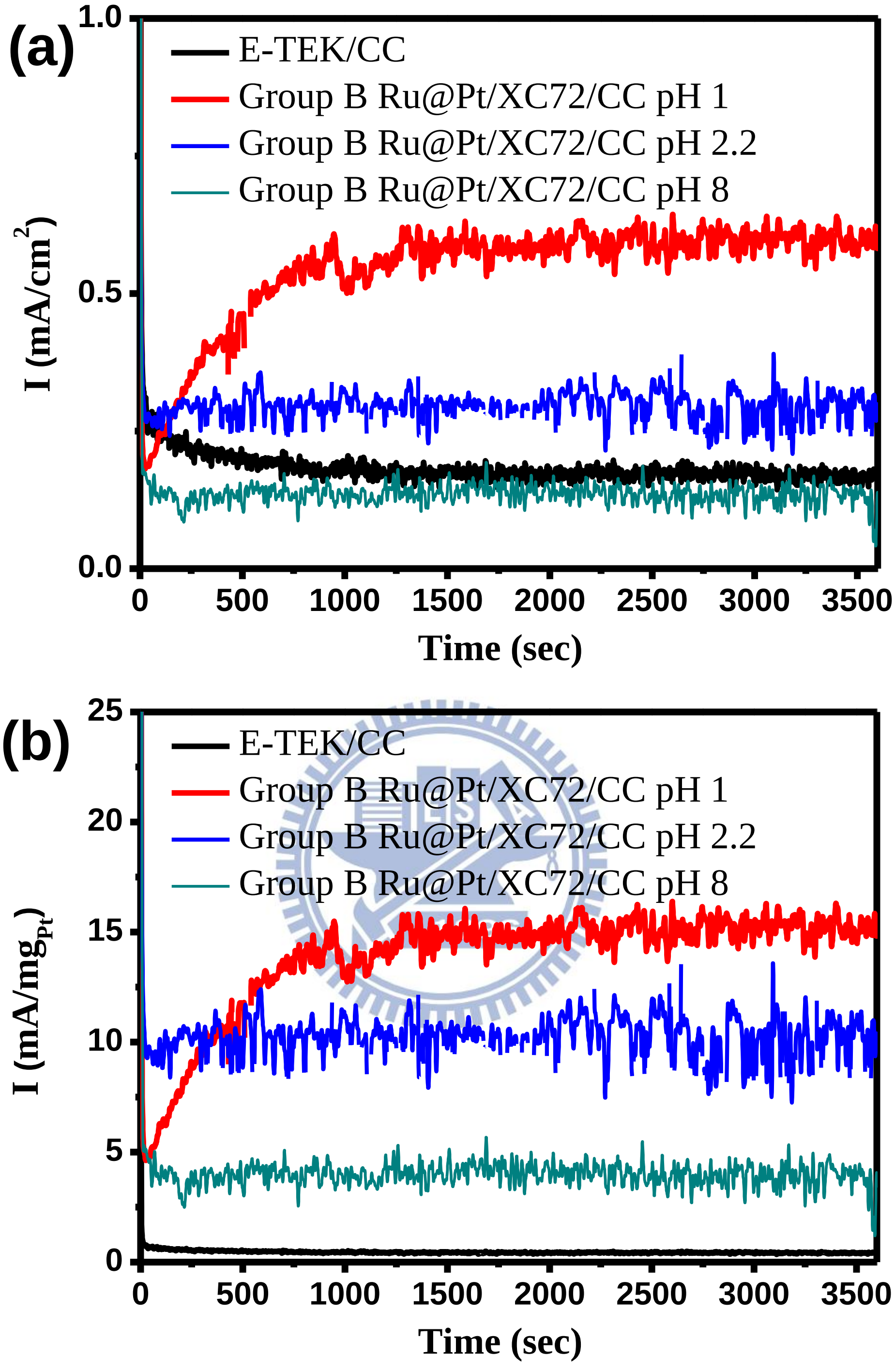

Figure 4.14. The H_2 oxidation curves in (a) apparent current density and (b) mass activity on E-TEK/CC and Ru@Pt/XC72/CC from group B of pH 1, pH 2.2, and pH 8.

4.3.4 EQCM analysis

Electrochemical quartz crystal microbalance (EQCM) measurements were performed to further investigate mass variation occurring during PtRu galvanic displacement reaction. The quartz crystal, with an Au film on surface for electrical conductivity, was immersed in the Pt or PtRu plating baths. The Pt bath was 10 mM H_2PtCl_6 + 100 mM H_2SO_4 aqueous solution, and the PtRu bath was 5 mM H_2PtCl_6 + 5 mM $Ru(NO)(NO_2)_4(OH)^{2-}$ + 100 mM H_2SO_4 aqueous solution. Periodic pulse currents were imposed at repeated sequences of 50 mA/cm^2 for 1 sec and rested for 50 sec. The plot of current density vs. time is shown in Fig. 4.15(a) and Fig. 4.15(d). The mass of electrodeposited species on the Au surface as a function of time was recorded for Pt and PtRu baths, respectively (shown in Fig. 4.15(b) and Fig. 4.15(e)). At a fixed pulse current, the mass increment in each pulse for the Pt bath was nearly identical (Fig. 4.15(b)). In contrast, the mass increment in each pulse for the PtRu bath was notably different (Fig. 4.15(e)). The open circuit potential for the metal deposited on the Au surface as a function of time was also recorded. As shown in Fig. 4.15(c), during the pulse current deposition in Pt bath, the potential remained unchanged during resting time of 50 sec, indicating that the surface state for the deposited Pt was rather stable. In contrast, as shown in Fig. 4.15(f), during the pulse current deposition in PtRu bath, the potential changed significantly during resting time, suggesting that a continuous surface rearrangement was taking place. This surface rearrangement was attributed to the displacement reaction between the freshly deposited Ru metal and Pt cations during resting time of 50 sec.

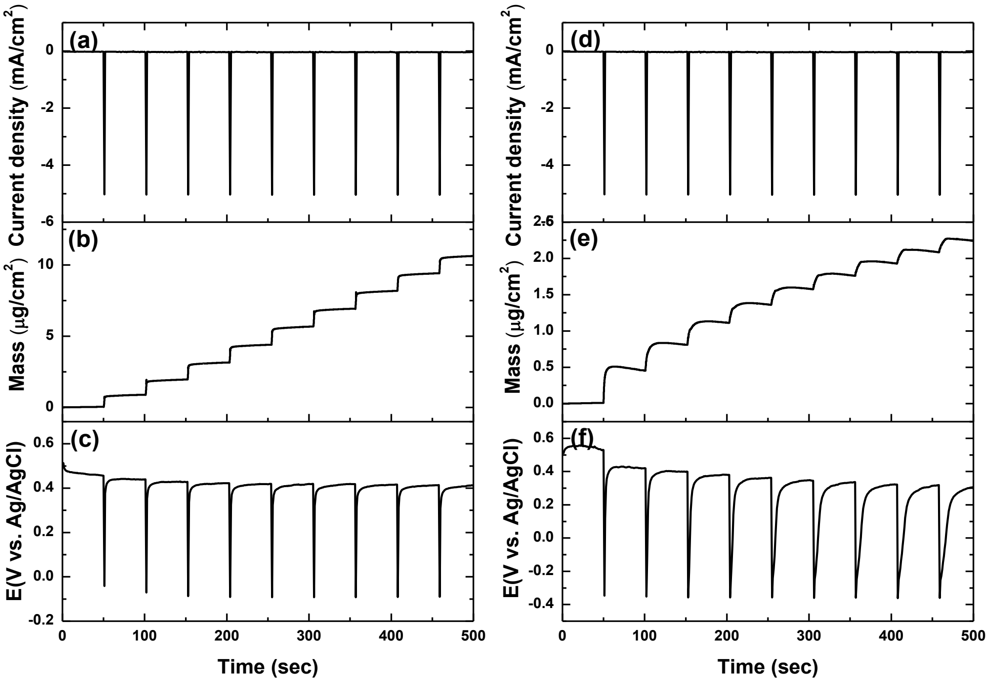

Figure 4.15 EQCM measurements using Pt plating bath; (a), (b), and (c), as well as PtRu plating bath; (d), (e), and (f). The (a) and (d) are the current profile during pulse deposition. The (b) and (e) are their respective mass variation in each pulse. The (c) and (f) are the voltage reading during plating time and open circuit voltage during resting time.

The enlarged EQCM profiles for a single pulse are presented in Fig. 4.16 in which the blue vertical line defines both the ending point of the pulse current of 50 mA/cm^2 and the starting point of resting time. As shown in Fig. 4.16(b), in the Pt bath the mass change at the blue vertical line was associated entirely with pulse current electrodeposition, designated as the “electrodeposition mass change”, while the mass change after the blue vertical line was significantly smaller as compared to the “electrodeposition mass change”. This reduced amount was attributed to the Pt surface oxidation, which is designated as the “surface oxide mass change”. Also the potential for the deposited Pt after the blue line, as shown in Fig. 4.16(c), stabilized rapidly and arrived at a value that is rather close to the thermodynamic potential of oxide formation on the Pt surface (E^0 = 0.43 V vs. Ag/AgCl)[30]. In contrary, in PtRu bath, the mass change after the blue line was considerably larger than the “electrodeposition mass change” before the blue line, as shown in Fig. 4.16(e). Also the potential for the deposited PtRu after the blue line shown in Fig. 4.16(f) stabilized slowly as compared to that shown in Fig. 4.16(c). We attribute such notable mass and potential variations on the samples from PtRu bath to galvanic displacement reaction. When the current was resting, a severe displacement reaction took place between the metallic Ru atoms electrodeposited on the Au surface and the Pt ions in the plating bath, resulting in the observed changes in both mass and potential.

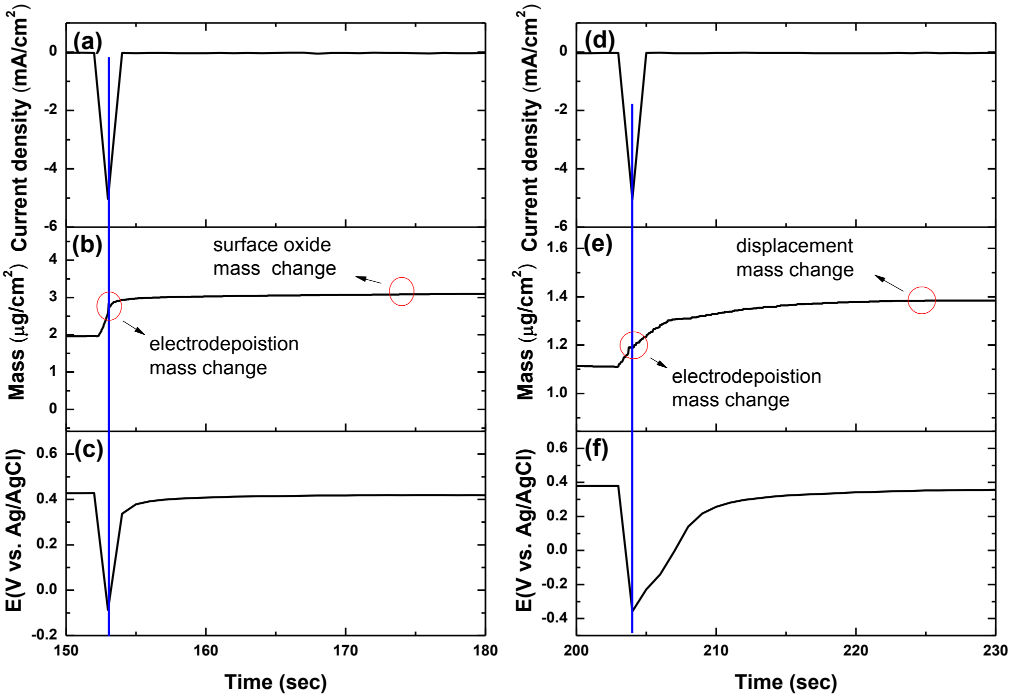

Figure 4.16 EQCM profiles in a single pulse; (a), (b), and (c) for Pt plating bath, and (d), (e), and (f) for PtRu plating bath. The (a) and (d) are the current profile during pulse deposition. The (b) and (e) are their respective mass variation in each pulse. The (c) and (f) are the voltage reading during plating time and open circuit voltage during resting time.

Fig. 4.17 provides the ratio for the surface oxide mass change (for the sample from Pt bath) or the displacement mass change (for the sample from PtRu bath) to the electrodeposition mass change, i.e. the ratio of mass change when the current was resting to that when the current was on. As shown in Fig. 4.17(a), in Pt bath, the ratio of mass change was merely 30-40 %. In contrast, in PtRu bath, as shown in Fig. 4.17(b), the mass change when the current was resting was 50-400 %, suggesting that a substantial amount of mass increment was resulted from the galvanic displacement reaction when the current was turned off.

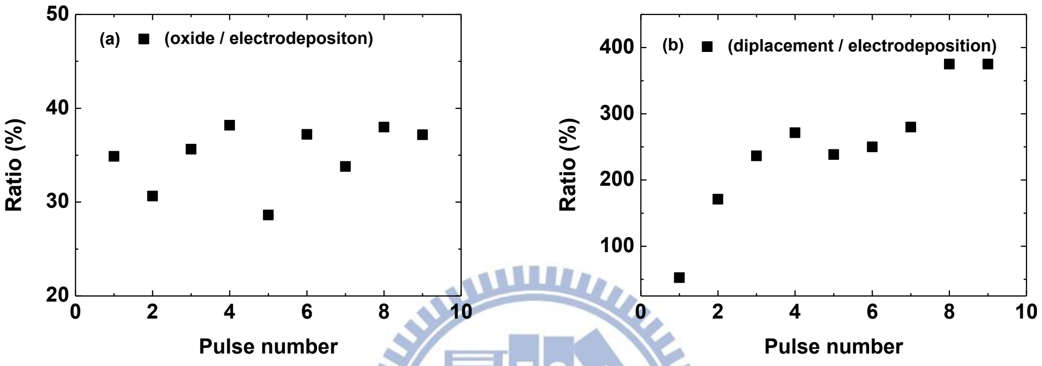

Figure 4.17 Ratio of (a) the surface oxide mass change (for the sample in Pt bath) or (b) the displacement mass change (for the sample in PtRu bath) to the electrodeposition mass change. These data were obtained for the first ten pulses from EQCM measurements in Fig. 4.15.

4.4 Conclusions

The mechanism of Pt displacement reaction on the Ru to form Ru@Pt nanoparticles was investigated by immersing the carbon-supported Ru nanoparticles in hexachloroplatinic acids with various pH values, followed by hydrogen reduction. XRD patterns demonstrated that the Ru hcp lattice was expanded slightly after Pt incorporation. Results from ICP-MS suggested that the dissolution of Ru was mostly caused by the reduction of Pt cations. TEM images demonstrated a uniform distribution of Ru@Pt in size of 3–5 nm. Analysis from XANES and EXAFS indicated that the pH value of hexachloroplatinic acids determined the type of ligands around the Pt cations that led to different stages of displacement reaction. The oxidation state of Ru ions after displacement was determined to be +3 by Ru K-edge XANES. After hydrogen reduction, samples from pH=1 bath revealed a desirable core–shell structure that displayed a reduced onset potential in CO stripping measurements and stable catalytic performances for H_2 oxidation with negligible performance degradation. The further exploration on the displacement reaction mechanism was carried out by EQCM. The unusual magnificent mass increment could not be explained unless it was ascribed to the galvanic displacement reaction.

Chapter 5 Enhancement of Methanol Electro-oxidation via Functionalization of Carbon Supports by the Electrochemical Degradation of Nafion Ionomer

5.1 Introduction

Carbonaceous materials have been widely used as the substrates for catalyst impregnations in room tempeaturare fuel cells like polymer membrane fuel cells and direct methanol fuel cells.[7, 128-136] It is because with the selection of carbons as supports, nanoparticulate catalysts such as Pt and PtRu are able to distribute uniformly, leading to reduced loading and better catalyst utilization. To date, carbons in a rich variety of forms including carbon blacks, carbon nanotubes (CNTs), mesoporous carbons, carbon nanocapsules, activated carbons, and carbon xerogels have been investigated as the catalyst supports with impressive results.[137-142] The interactions between the carbon and catalyst are critical because a lack of sufficient bonding between them causes possible detachments and colaescence, which results in undesirable performance degradation.[6] Unfortunately, untreated carbons are often hydrophobic in nature that allow poor adsorption of catalyst precursors and catalysts. Therefore, it is necessary to carry out additional functionalization treatments on the carbons to render a hydrophilic surface instead. After proper surface functionalizations, the carbons are expected to adsorb more catalyst precursors for a larger amount of catalyst deposition.

Earlier studies on the carbon functionalizations are concerned with carbon corrosions because under the operation conditions of phosphoric acid fuel cells, the carbon is prone to oxidation loss by the formation of surface oxidized groups.[143-147] In general, the functionalization of carbon involves anodization treatments in concentrated acids at moderate temperature.[148, 149] For example, Kangasniemi et al. imposed potentiostatic treatments on the Vulcan XC72 (XC72) in 1 M H_2SO_4 solution, and determined that at room termperature, a signficant oxidation was occurring for the anodizing voltage of 1.2 V for 16 h but 0.8 V was sufficent at 65°C to produce the same effect.[150] A similar anodization treatment of 2 V was employed by Stevanovic et al. to introduce selective functional groups on the glassy carbons.[151] The degree of surface functionalization also depends on the type of carbon materials because their surface area and microstructure differ considerably. For instance, the CNTs reveal notable oxidation resistance over the XC72 while the BP2000, with a larger specific surface area (m^2g^{-1}), experiences more oxidation loss as opposed to the XC72 with a smaller specific surface area.[152] So far, after functionalization, surface oxidized groups such as phenols, carbonyls, carboxylic acids, ethers, quinones, and lactones have been identified. The exact mechanism responsible for the formation of selective functional groups is contingent on the processing steps involved and the type of carbon materials. Since the carbon is relatively inert in corrosive electrolytes, typical surface functionalization steps are rather time-consuming. Therefore, it is of particular interest to develop a simple and efficient process for functionalization purpose.

An alternative approach to functionalize the carbon materials is by chemical alteration of polymeric binders. In electrode fabrications, Nafion ionomer is often added in mixture with carbons, serving simultaneously as a binder and conductive path for proton transports. Therefore, it is possible that the Nafion ionomer would suffer from structural damage and loss of sulfonic acid side chains if deliberate electrochemical treatments are applied. Previously, extensive efforts have been devoted to understand the responsible mechanism for Nafion membrane degradation in different environments and factors including humidity, temperature, and oxygen concentration are found to be relevant.[18, 153] According to literature, hydroxyl (•OH) and peroxy (•OOH) radicals formed during fuel cell operations are able to react with polymer end groups that still contain residual terminal H-groups.[20, 154, 155] Further studies indicate that the sulfonic acid side chains are also susceptible to radicals[21, 153, 156]. In addition, the degraded species of Nafion contain free radicals that have been reported to attack carbons and chemically bond to their surface.[22, 157, 158] Moreover, it is suggested that the presence of functionalized groups on the carbon surface is possible to engender additional oxidized groups.[159-161] In light of this information, we realize that the intentional degradation of Nafion ionomer might provide an effective route for carbon functionalization.

In this work, we conducted multiple cyclic voltammetric scans (CV) to introduce functional groups on the electrode structure, followed by Pt cation adsorption and electrochemical reduction to produce nanoparticulate Pt impregrenated on the functionalized support. Electrocatalytic analysis on the methnaol electro-oxidation was performed to elucidate the effect of functionalized support for catalytic actions.

5.2 Experimental

Carbon surface functionalization by Nafion ionomer

The electrode for surface functionalization was fabricated by depositing a carbon/Nafion mixture onto a commercially available carbon cloth (E-TEK). First, 10 mg Nafion ionomer solution (5 wt%) and 8 mg carbon powders (Vulcan XC-72R) were mixed in 5 mL 99.5 wt% ethanol for 60 min under sonication to form an ink dispersion. The dispersion was deposited repeatedly on a 4 cm^2

carbon cloth which was kept at 80°C atop a hotplate to evaporate residual solvent. The loadings for the XC-72R and Nafion ionomer on the carbon cloth were 2 and 0.05 mgcm^{-2}, respectively. Subsequently, the surface functionalization was performed by imposing CV scans on the electrode (active area of 0.785 cm^{2}) for 20 cycles between −0.2 and 1.1 V (vs. Ag/AgCl) at 50 mVs^{-1} in an aqueous electrolyte of 0.5 M H_2SO_4. A Pt foil of 10 cm^{2} was used as the counter electrode. The duration for the CV scans was 17 min. In order to introduce oxygen during the CV scans, the backside for the electrode was pressed against a stainless steel foil that was partially exposed to the ambient oxygen. A schematic for the cell design is illustrated in Fig. 5.1. For comparison purpose, we also immersed the as-prepared electrodes in 0.5 M H_2SO_4 or 0.5 M HCl aqueous solution with concentrated residues from Nafion ionomer decomposition to analyze their surface functional groups. The functionalized electrode was immersed in a 5 mM H_2PtCl_6 aqueous solution (pH adjusted to 8) at 40°C. The immersion lasted for 48 h to ensure sufficient adsorption of $PtCl_6^{2-}$. To reduce the adsorbed Pt ions, CV scans were carried out between −0.2 and 0.2 V in 0.5 M H_2SO_4 at 50 mVs^{-1}.

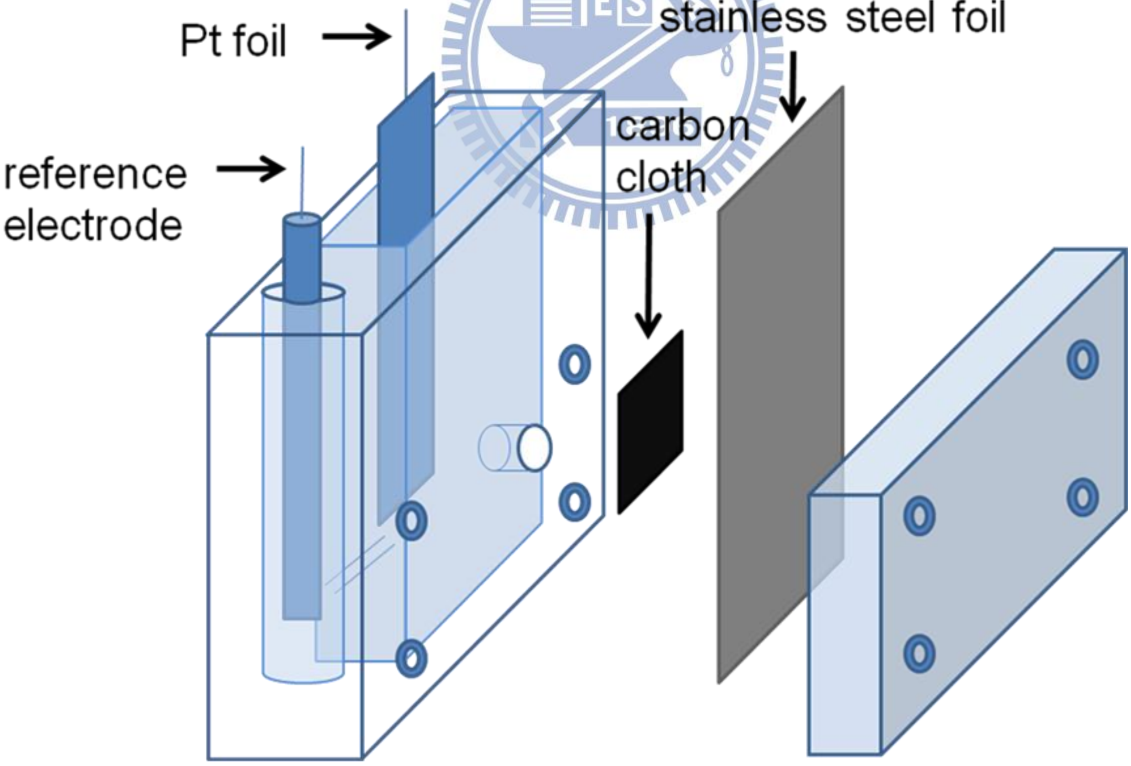

Figure 5.1. A schematic of the electrochemical cell for CV scans in 0.5 M H_2SO_4 aqueous solution. The carbon cloth is partially exposed to ambient oxygen.

Electrochemical analysis

The functionalized electrode was immersed in a 5 mM H_2PtCl_6 aqueous solution (pH adjusted to 8) at 40℃. The immersion lasted for 48 h to ensure sufficient adsorption of $PtCl_6^{2-}$. To reduce the adsorbed Pt ions, CV scans were carried out between −0.2 and 0.2 V in 0.5 M H_2SO_4 at 50 mVs^{-1}. To evaluate the electrochemical surface area (ECSA) for the deposited Pt, we conducted CV scans between −0.2 and 0.9 V in 0.5 M H_2SO_4 at 50 mVs^{-1}. The ECSA was estimated by the integrated charge in the hydrogen desorption region. For methanol electro-oxidation, multiple CV scans were performed between −0.2 and 0.9 V at 50 mVs^{-1} in 500 ml of 0.5 M H_2SO_4 and 1 M CH_3OH. The area for the working electrode was 0.785 cm^2. The Ag/AgCl and Pt foil (10 cm^2) were used as the reference and counter electrodes, respectively. Surface functionalization, $PtCl_6^{2-}$ reduction, ESCA determination, and methanol electro-oxidation were carried out at 26°C in a three-electrode arrangement using a EG&G 263Apotentiostat.

Materials characterizations

X-ray Photoelectron Spectroscopy (XPS; Thermo Microlab 350) was adopted to evaluate the oxygenated functional groups on the functionalized electrodes. Raman Spectroscopy (LabRAM HR800) was conducted to detect the microstructure variation on the XC-72R after CV scans. Ion chromatography (Dionex DX120) was utilized to analyze the concentration of dissolved SO_4^{2-} and fluoro carbons from the decomposition of Nafion ionomer. Transmission Electron Microscope (TEM; Philips Tecnai-20) was used to observe the morphologies and distributions for the Pt nanoparticles. The average Pt size was obtained by TEM image analysis (Image-Pro Plus 6.0).The amount of Pt loadings was determined by an Inductively Coupled Plasma Mass Spectrometry (ICP-MS; SCIEX ELAN 5000) where the samples were dissolved in a solution containing HCl, HNO_3, and HF at a 2:2:1volume ratio.

5.3 Results and discussion

5.3.1 Electrochemical degradation of Nafion ionomer

Fig. 5.2 provides the CV profiles at various cycles for the electrodes containing carbon cloth, Nafion ionomer, and XC-72R with the supply of ambient oxygen. As shown, the CV profiles exhibited a characteristic behavior for capacitors with symmetric responses in which considerable anodic and cathodic currents were observed above 0.9 V and below −0.1 V, respectively. Notably, the current from the anodic scan for the first cycle was negligible until 0.9 V when a sharp rise occurred. After that, there appeared obvious currents for the cathodic scan, suggesting surface activation at an oxidative potential above 0.9 V in the first cycle. Interestingly, both the anodic and cathodic currents demonstrated steady increments with increasing CV cycles. We understood that the recorded currents were mostly from the XC-72R as the carbon cloth contributed an insignificant amount with its relatively reduced surface area. However, in our observation, samples of XC-72R deposited on the carbon cloth revealed CV curves that were insensitive to increasing cycles, a generic behavior for electrochemical double-layer capacitors. Therefore, we realized that there was chemical degradation of Nafion ionomer that led to the increasing currents.

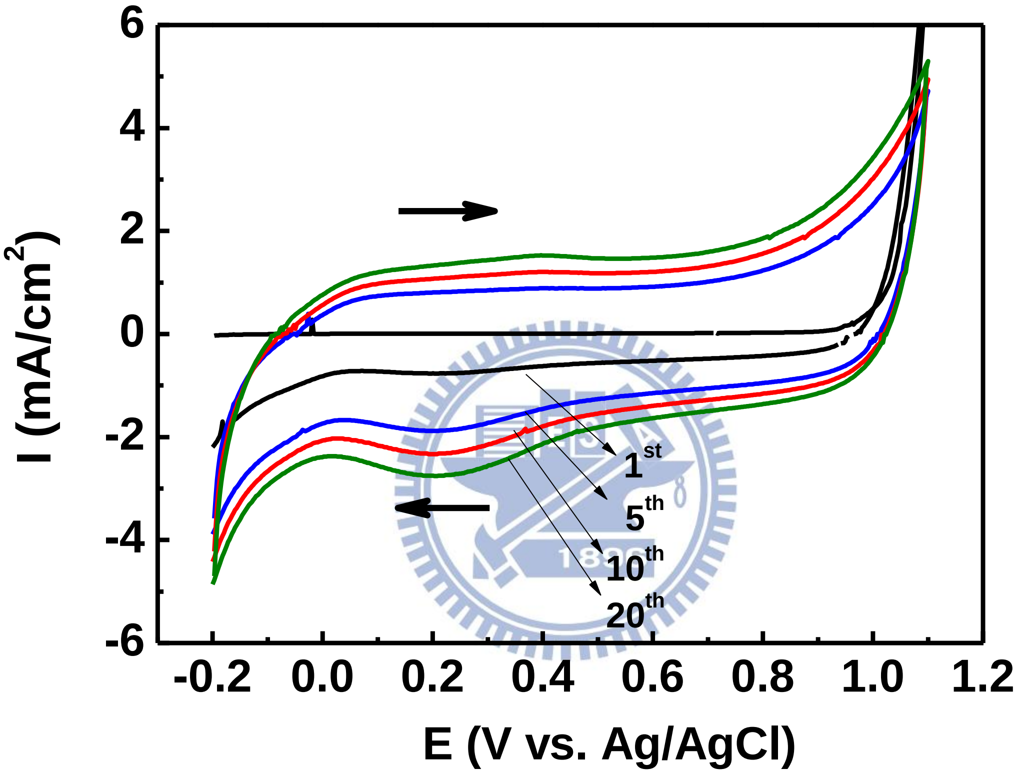

Figure 5.2. Profiles from multiple CV scans with ambient oxygen for electrodes containing carbon cloth, XC-72R, and Nafion ionomer.

In order to observe the effect of Nafion ionomer degradation more clearly, we need to remove the capacitive currents from the XC-72R. Therefore, we carried out additional experiments with the electrodes containing carbon cloth and Nafion ionomer only. Fig. 5.3(a) exhibits the CV profiles for the samples with the supply of ambient oxygen. As shown, there appeared obvious oxidation and reduction peaks centering around 0.55 and 0.34 V, respectively. In addition, these signals increased steadily with increasing cycles. According to literature, these peaks were attributed to hydroquinone-quinone redox couple on the carbon substrates, suggesting the formation of oxygenated functional groups on the surface.[150-152] Also shown is the carbon cloth without the addition of Nafion ionomer but with the oxygen supplied from ambient. Obviously, there was negligible current in the CV scans, indicating that without Nafion ionomer, oxygenated functional groups on the carbon surface were not formed at noticeable amount.

Earlier studies on the Nafion membrane degradation have identified the hydroxyl (・OH) and peroxy (・OOH) radicals to be the active species to attack the chemical structure of Nafion. It was suggested that the dissolved oxygen diffuses to the anode side reacting with the hydrogen to form hydrogen peroxide.[20, 153] In our case, with sufficient supply of ambient oxygen, the CV scans in an acidic environment on the carbon electrodes were likely to initiate the oxygen reduction reaction by a two-electron route which led to the formation of hydrogen peroxide.[60, 162] This hydrogen peroxide subsequently engendered the decomposition of Nafion ionomer that further accelerated the oxidation of carbon. To verify the significance of oxygen in this process, we repeated the experiments with the electrodes containing carbon cloth and Nafion ionomer but without the supply of ambient oxygen. The elimination of oxygen was achieved by immersing the working electrode to the electrolyte completely in a sealed three-electrode cell in conjunction with sufficient argon purging to remove any dissolved oxygen. The resulting CV profiles are displayed in Fig. 5.3(b). Interestingly, there was negligible difference for the CV responses between the first and 20th cycle, and the absence of the hydroquinone-quinone redox couple was obvious. This behavior indicated that without the simultaneous presence of oxygen and Nafion ionomer, the formation of oxygenated functional groups on the carbon surface was rather unlikely. An alternative approach to produce the hydroxyl radical (・OH) is the direct oxidation of water.[20] This is a scenario that is possible in the CV scans without the supply of ambient oxygen. However, from Fig. 5.3(b) we concluded that the direct oxidation of water was unable to produce sufficient hydroxyl radicals (・OH) for Nafion iomomer degradation. Therefore, the principal cause for the formation of oxygenated functionalized groups on the carbon surface was the oxygen reduction route that engendered the decomposition of Nafion ionomer.

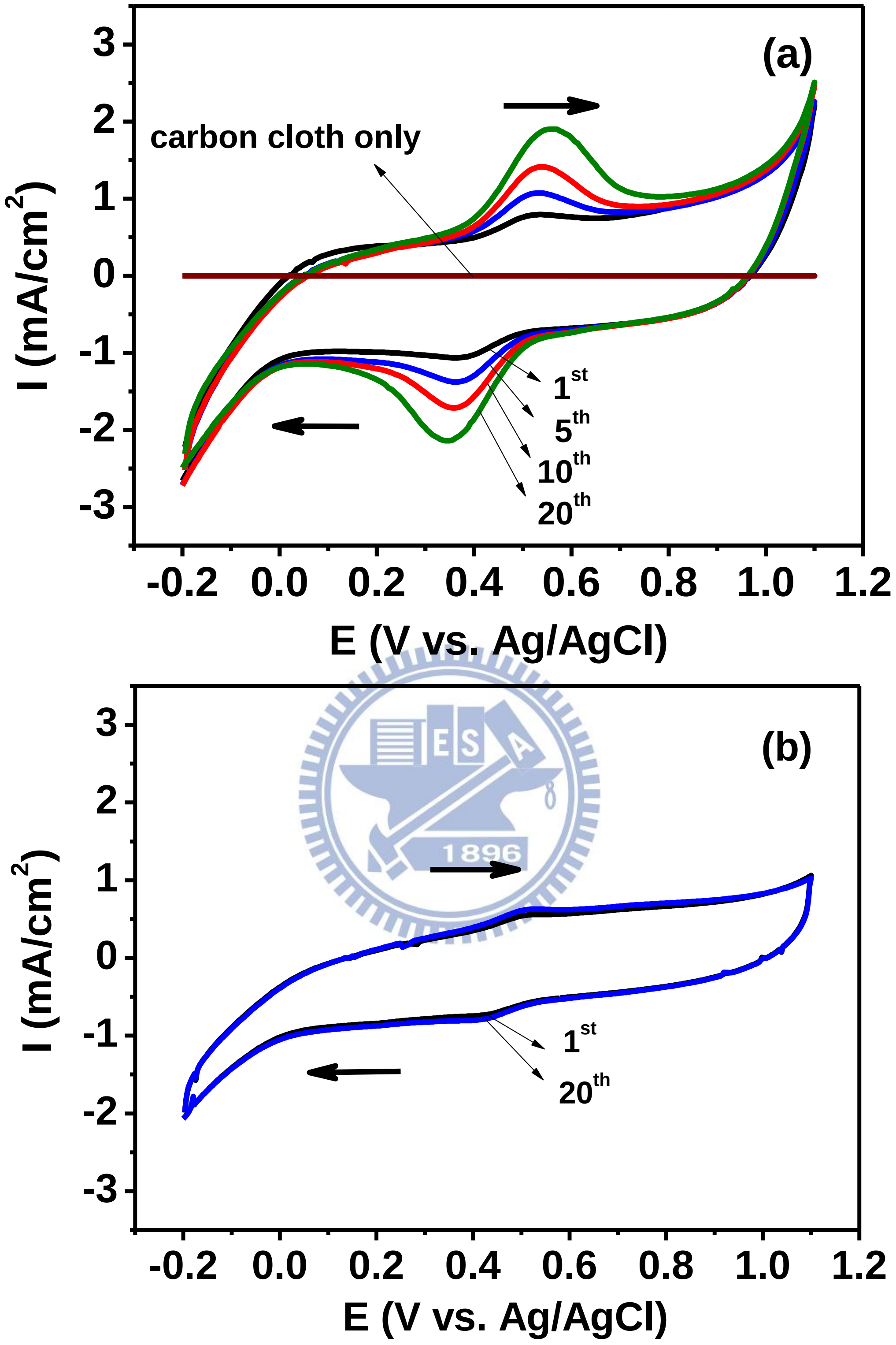

Figure 5.3. Profiles from multiple CV scans (a) with ambient oxygen and (b) without ambient oxygen for electrodes containing carbon cloth and Nafion ionomer. Also shown in (a) is the electrode with carbon cloth only.

To further validate the contributory role of Nafion ionomer and oxygen for carbon functionalizations, additional experiments on the carbon cloth and Nafion ionomer were carried out. We performed the CV scans with and without the supply of ambient oxygen, and recorded their anodic currents at the 20th cycle. Fig. 5.4 exhibits the comparison for the anodic current at 0.5 V for both samples, as well as data from Fig. 5.2 and Fig. 5.3(a), respectively. Apparently, without the supply of ambient oxygen, the anodic current became relatively subdued for every sample. In general, the presence of oxygen promoted the oxidation of carbon and hence resulted in a larger oxidation current. However, with the addition of Nafion ionomer, the effect of oxygen became more pronounced. It is therefore concluded that the degradation of Nafion ionomer, promoted by the presence of oxygen, led to accelerated carbon functionalization.

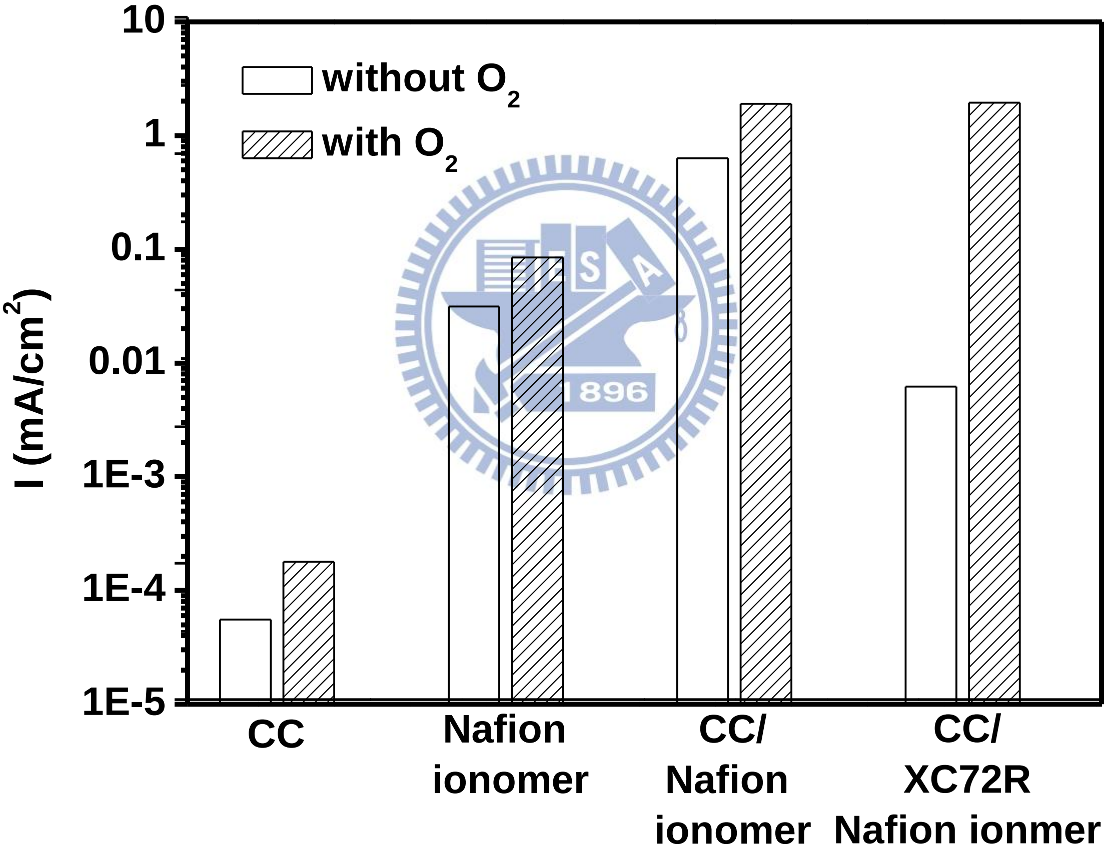

Figure 5.4 Comparison in the current value obtained at 0.5 V from the 20th CV cycle for electrodes containing carbon cloth (CC), Nafion ionomer, CC/Nafion ionomer,and CC/XC-72R/Nafion ionomer. These CV experiments are performed with ambient oxygen and without ambient oxygen, respectively.

5.3.2 Carbon functionalization

Fig. 5.5 demonstrates the Raman spectra for the electrodes after CV scans and H_2SO_4 immersion. As shown, both samples revealed characteristic peaks which were defined as D-band (1310 cm^{-1}) and G-band (1596 cm^{-1}), respectively. The D-band represented the presence of defects and disorder in the carbon structure while the G-band reflected the graphitic in-plane vibrations with E_{2g} symmetry.[6] Hence, the ratio of D/G signals suggested the degree of crystallinity in the carbon structure. As mentioned earlier, the electrode undergoing the H_2SO_4 immersion was selected for comparison purpose and it exhibited a D/G value of 2.57. In contrast, the sample after CV scans revealed a D/G value of 2.67. This moderate variation in the D/G ratio inferred that the carbon structure was reasonably maintained after CV treatments. The XPS was adopted to obtain variations on the signals from carbon, oxygen, and fluorine for the electrodes under CV scans with and without the supply of ambient oxygen. We also performed the XPS analysis on the as-prepared electrode without CV scans for comparison. As shown in Fig. 5.6, relevant peaks on the XPS profiles (resolution in 1 eV) were labeled properly and they were identified as F1s, F_{kll}, O1s, and C1s, respectively. Table 5.1 lists their respective atomic ratios. It can be seen that there was negligible difference in the atomic ratios between samples in the as-prepared state and after CV scans without the supply of ambient oxygen. However, the sample after CV scans with the supply of ambient oxygen revealed a similar carbon amount but its atomic ratio for the oxygen was increased considerably in conjunction with a notable reduction in the fluorine content. These results suggested that the CV scans coupled with the supply of ambient oxygen were able to produce oxygen-rich functional groups on the electrode surface while the Nafion ionomer was partially decomposed.

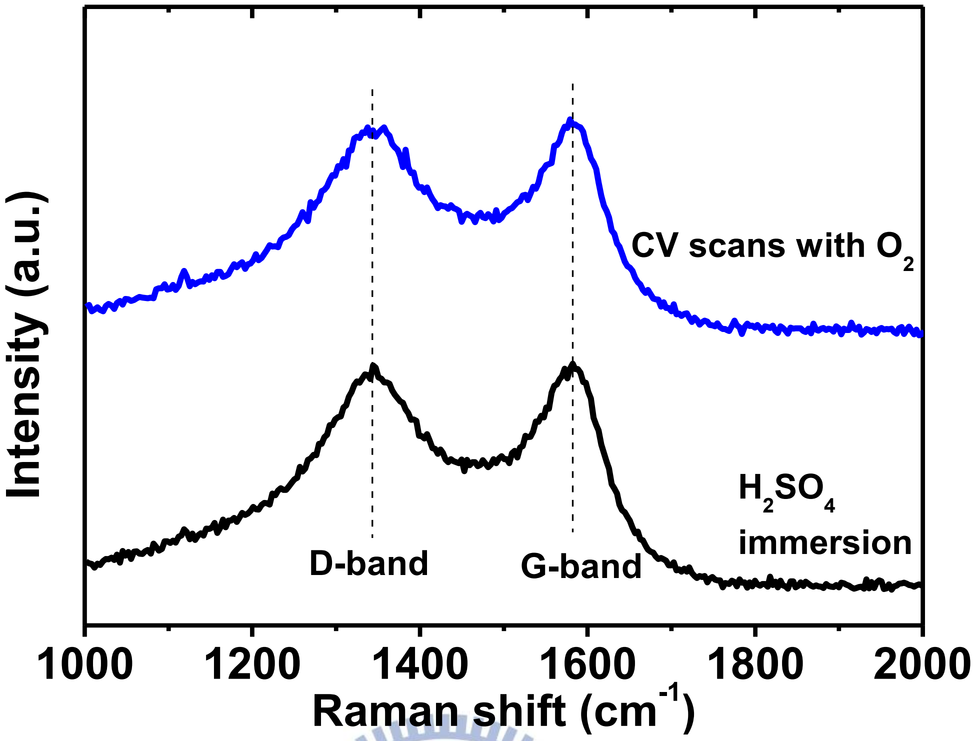

Figure 5.5. Raman spectra for electrodes after CV scans with ambient oxygen and H_2SO_4 immersion only. These electrodes contain carbon cloth, XC-72R, and Nafion ionomer.

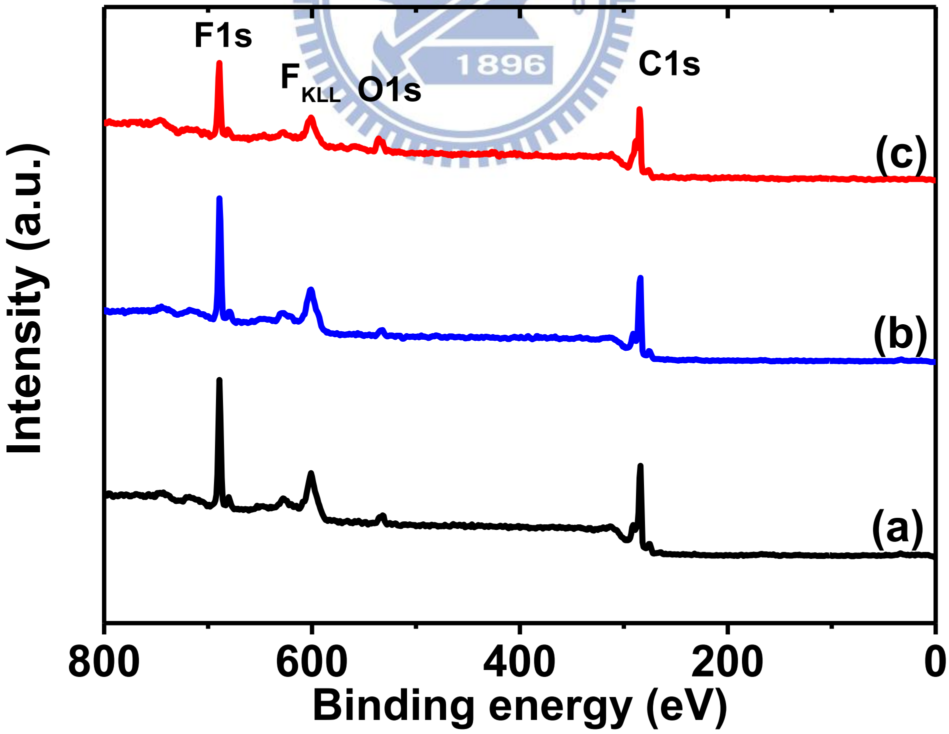

Figure 5.6. XPS surveys for (a) as-prepared electrode, as well as electrodes after CV scans (b) without ambient oxygen and (c) with ambient oxygen. These electrodes contain carbon cloth, XC-72R, and Nafion ionomer.

Table 5.1. The atomic ratios for carbon, oxygen, and fluorine from XPS profiles for as-prepared electrode, as well as electrodes after CV scans with and without the supply of ambient oxygen.

	C (at%)	O (at%)	F (at%)
as-prepared	61	4.3	34.7
CV scans without O_2	62	3.5	34.5
CV scans with O_2	61.6	10.5	27.9

Fig. 5.7(a) presents the C1s XPS profiles (resolution in 0.1 eV) for the as-prepared electrode and electrodes after CV scans with and without the supply of ambient oxygen, respectively. Apparently, the as-prepared sample and the one after CV scans without the supply of ambient oxygen displayed similar patterns as expected. In contrast, the sample after CV scans with the supply of ambient oxygen demonstrated a notable peak around 286-288 eV in addition to the typical C1s signal at 284.5 eV. To understand its nature, this C1s profile was subjected to curve-fitting with known functional groups to determine their relative amounts. Fig. 5.7(b) illustrates the curve-fitting results and the atomic ratios for individual functional groups are listed in Table 5.2. These functional groups were selected from earlier literature reports and were presumed to be present in the functionalized electrodes.[148, 150-152] From Table 5.2, the sample after CV scans with the supply of ambient oxygen revealed a notable reduction in the amount for C−F group. In addition, the oxidized −C=O and –COOH groups were substantially increased along with considerable reduction in the C−C backbone.

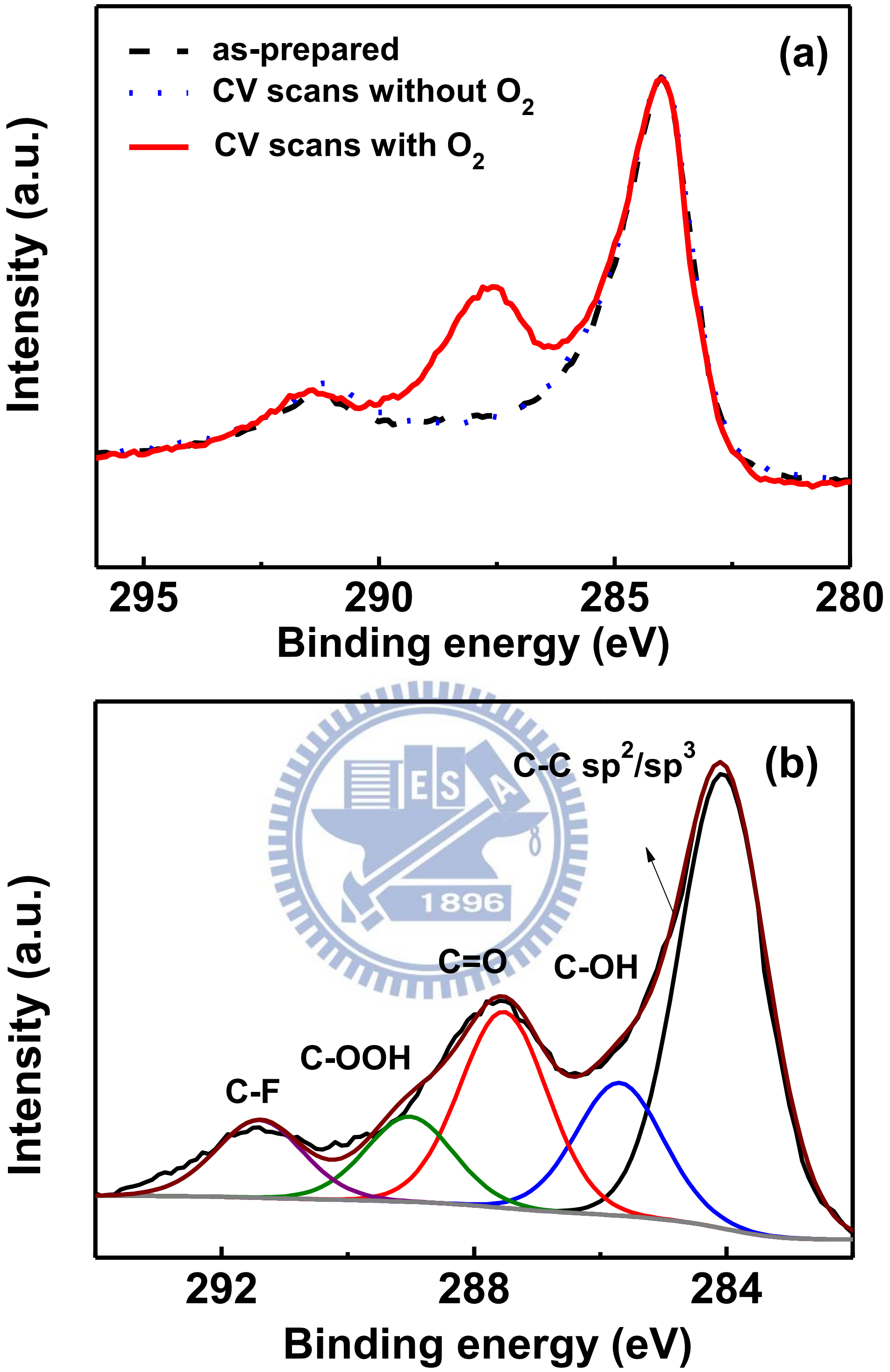

Figure 5.7. (a) C1s XPS profiles for as-prepared electrode, as well as electrodes after CV scans without ambient oxygen and with ambient oxygen. (b) Curve fitting for the C 1s XPS profile from electrode after CV scans with ambient oxygen. These electrodes contain carbon cloth, XC-72R, and Nafion ionomer.

Table 5.2. The atomic ratios for the C−C, −OH, −C=O, −COOH, and C−F from XPS curve fitting for as-prepared electrode, as well as electrodes after CV scans with ambient oxygen and without ambient oxygen.

	C−C (at%) (backbone)	−OH (at%) (a)	−C=O (at%) (b)	−COOH (at%) (c)	C−F (at%)	(a+b+c)/C−C
as-prepared	63.7	14	6.3	5.7	10.3	40.8 %
CV scans without O_2	63.7	14	6.3	5	11	39.7 %
CV scans with O_2	48	14	20.6	9.1	8.1	91 %

So far, our results indicated that the decomposition of Nafion ionomer was initiated by the ambient oxygen and this process resulted in the formation of oxygenated functional groups on the carbon surface. To validate our premise, we attempted to obtain the S2p signal but the 0.5 M H_2SO_4 aqueous solution provided unnecessary background noises. Hence, we prepared several electrodes (carbon cloth/XC-72R/Nafion ionomer) and subjected them to CVs in 0.1 M HCl aqueous solution instead. The purpose for these CV scans was to decompose the Nafion ionomer so the HCl solution with concentrated residues was formed. According to Teranishi et al., the degradation of Nafion produced F^-, SO_3^{2-}, CO_2, SO_2, and some fluoro carbons.[163] Subsequently, we immersed the electrode made of XC-72R and carbon cloth in the HCl solution containing concentrated Nafion ionomer residues to allow sufficient adsorption of the decomposed species. As shown in Fig. 5.8, signals from the ion chromatography were attributed to SO_4^{2-} and F^- in different intensities. Similar constituents were observed in earlier work by Chen and Fuller for Nafion membrane degradation.[61] In their work, a rather strong CF_3COO^- peak was identified on the cathode side associated with the oxygen reduction reaction. Unfortunately, in our case the amount of CF_3COO^- was below the detection limit. This notable absence of CF_3COO^- was possibly due to its immediate readsorption onto the carbon surface after detachment from the Nafion backbone.

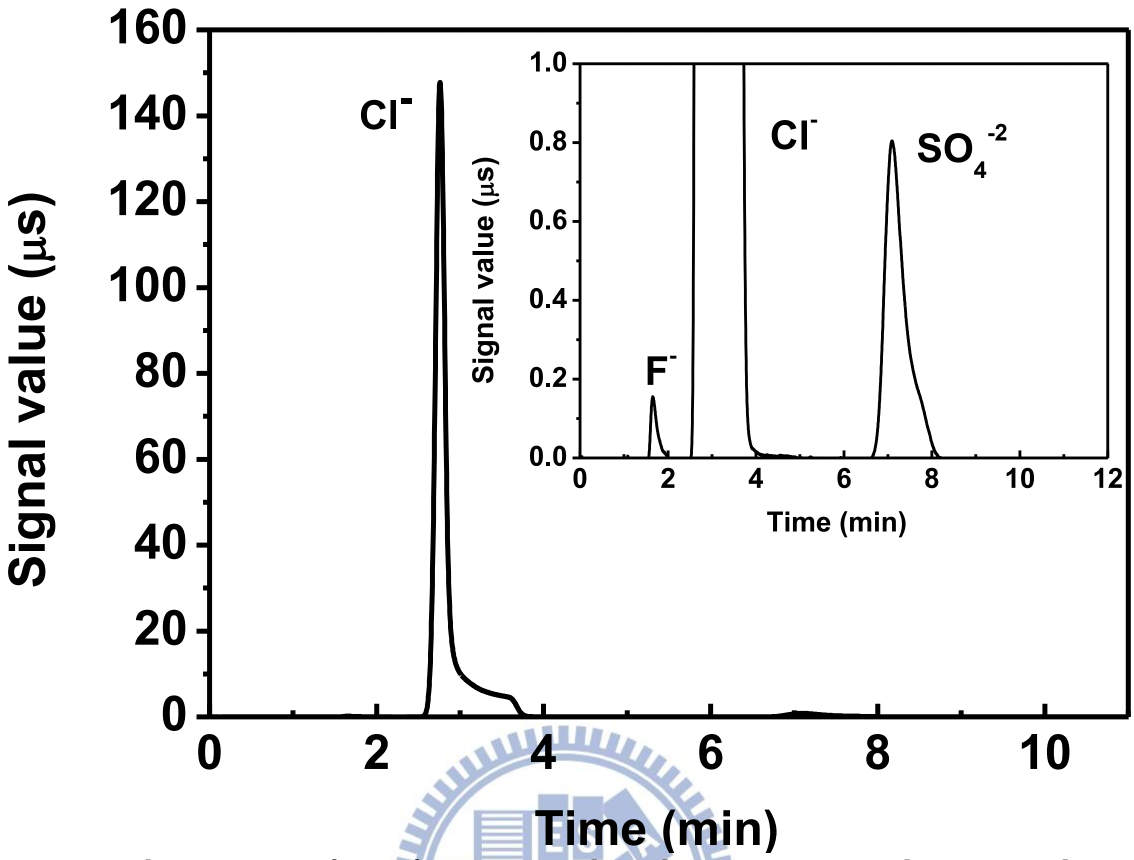

Figure 5.8. Ion chromatogram for Nafion ionomer degradation in 0.1 M HCl aqueous solution.

To monitor the extent of Nafion ionomer degradation, we recorded the signal for SO_4^{2-} upon CV cycles and the resulting data are displayed in Fig. 5.9. The value for the 0 cycle was obtained from the sample with immersion in the 0.1 M HCl aqueous solution for 17 min, which served as the reference because the sample of 20 CV cycles experienced the same amount of time in the 0.5 M H_2SO_4 aqueous solution. As shown, the reference sample revealed sulfate concentration of 0.35 ppm. This reduced amount was not unexpected as the Nafion ionomer likely maintained reasonable chemical stability against the 0.1 M HCl aqueous solution at 25℃. However, once CV scans were applied, the sulfate anion concentrations became larger considerably reaching a plateau after 20 cycles at 4.3 ppm. Apparently, within the first 20 cycles, there appeared a linear increase in the sulfate concentration with cycling number. This indicated that a desirable amount of Nafion decomposition and its subsequent carbon functionalization was possible by selecting appropriate CV scans.

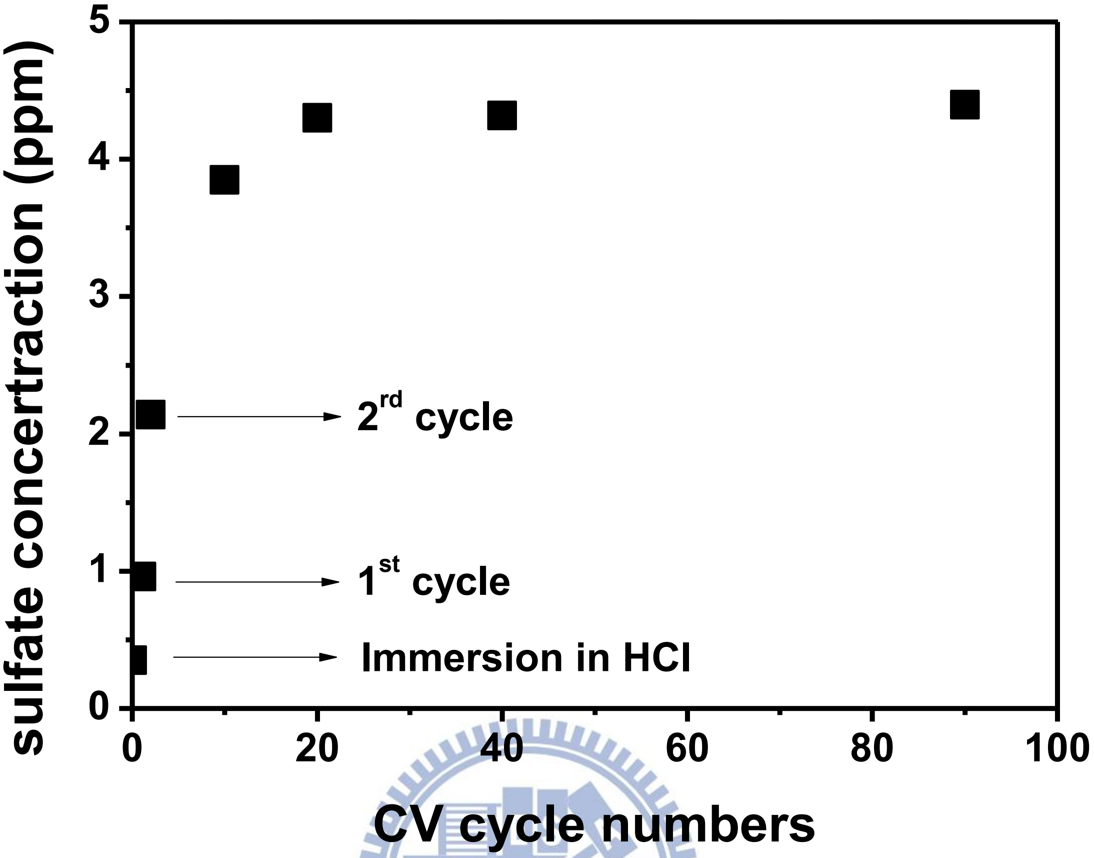

Figure 5.9. Variation of sulfate concentration as a function of CV scans with ambient oxygen. The data at 0th cycle is obtained from the electrode immersed in 0.1 M HCl aqueous solution.

Fig. 5.10 provides the C1s XPS profiles (resolution in 0.1 eV) for the as-prepared electrode (carbon cloth/XC-72R/Nafion ionomer) as well as electrodes (carbon cloth/XC-72R) with and without immersion in the HCl solution containing concentrated residues from Nafion ionomer decomposition. Apparently, the electrode of XC-72R/carbon cloth demonstrated a single C1s peak at 284 eV while the as-prepared electrode exhibited an additional C−F peak around 291 eV. However, the electrode of XC-72R/carbon cloth immersed in the HCl solution with concentrated decomposed Nafion ionomer residues revealed a strong signal around 289 eV which was attributed to the oxygenated groups on the carbon surface. Table 5.3 lists the atomic ratios for the individual functional groups from the curve-fitting results of Fig. 5.10. Apparently, the sample after immersing in the HCl solution showed a large amount of oxygenated functional groups. We surmised that the Nafion ionomer residue in the HCl solution was likely present as CF_3COO^-. After chemical adsorption, these residues were transformed to the oxygenated functional groups on the carbon surface.

The chemical adsorption of Nafion ionomer residues can also be confirmed from the S2p XPS profile (resolution in 0.1 eV) displayed in Fig. 5.11. The electrode of XC-72R/carbon cloth revealed a characteristic S2p signal near 164 eV which was attributed to the impurity intrinsic to the carbon material. However, the electrode of XC-72R/carbon cloth/Nafion ionomer demonstrated an additional peak around 168 eV which was caused by the HSO_3 from the Nafion ionomer. Interestingly, the XC-72R/carbon cloth sample immersed in the HCl solution with concentrated Nafion ionomer decomposed residues also exhibited the HSO_3 signal in addition to the S2p from impurity. This further supported our premise that the decomposed Nafion ionomer residues were able to chemically adsorb onto the carbon surface.

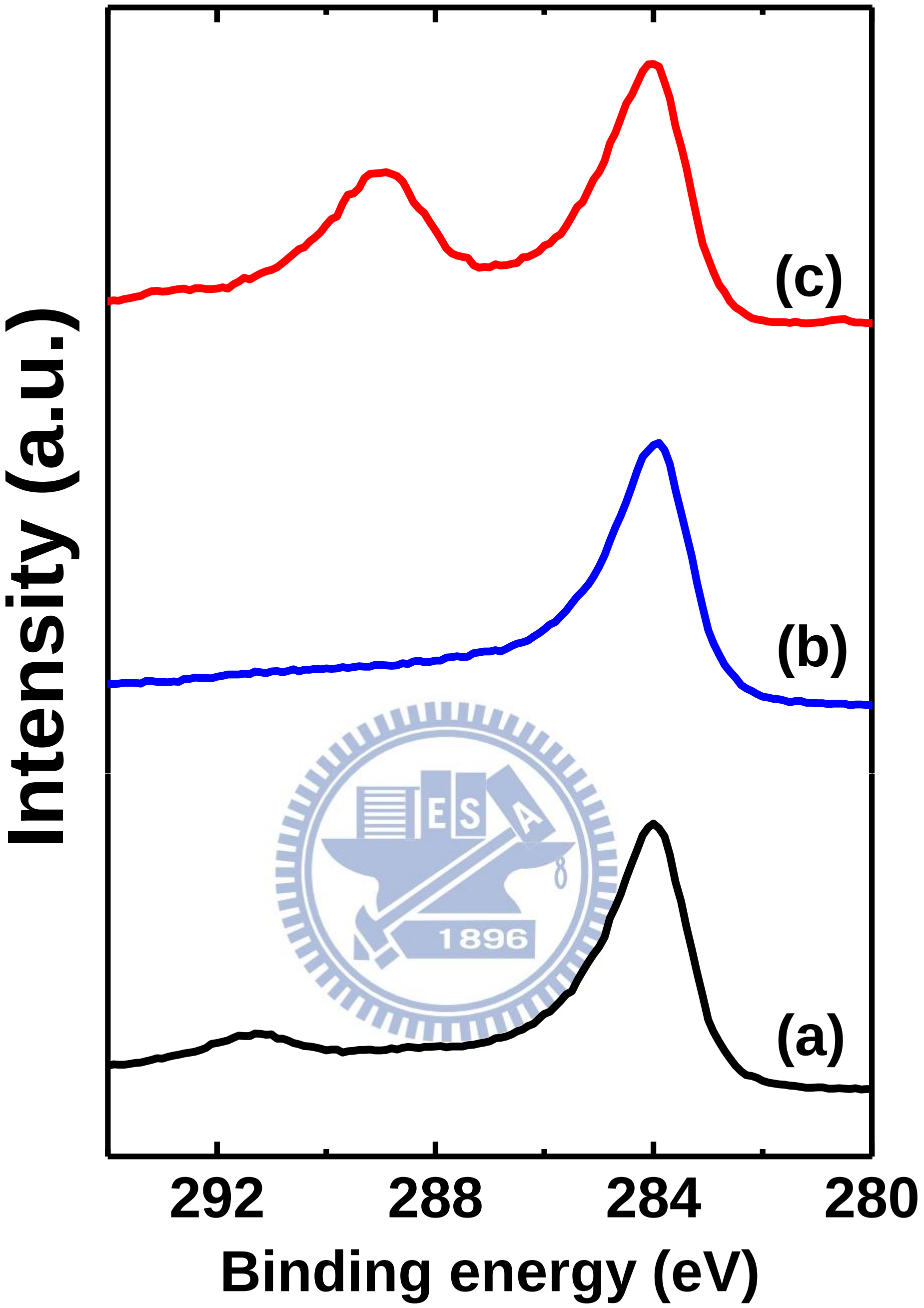

Figure 5.10. C1s XPS profiles for (a) as-prepared electrode (carbon cloth/XC-72R/Nafion ionomer), as well as electrodes (carbon cloth/XC-72R) (b) before and (c) after immersion in HCl solution ontaining concentrated residues from Nafion ionomer decomposition.

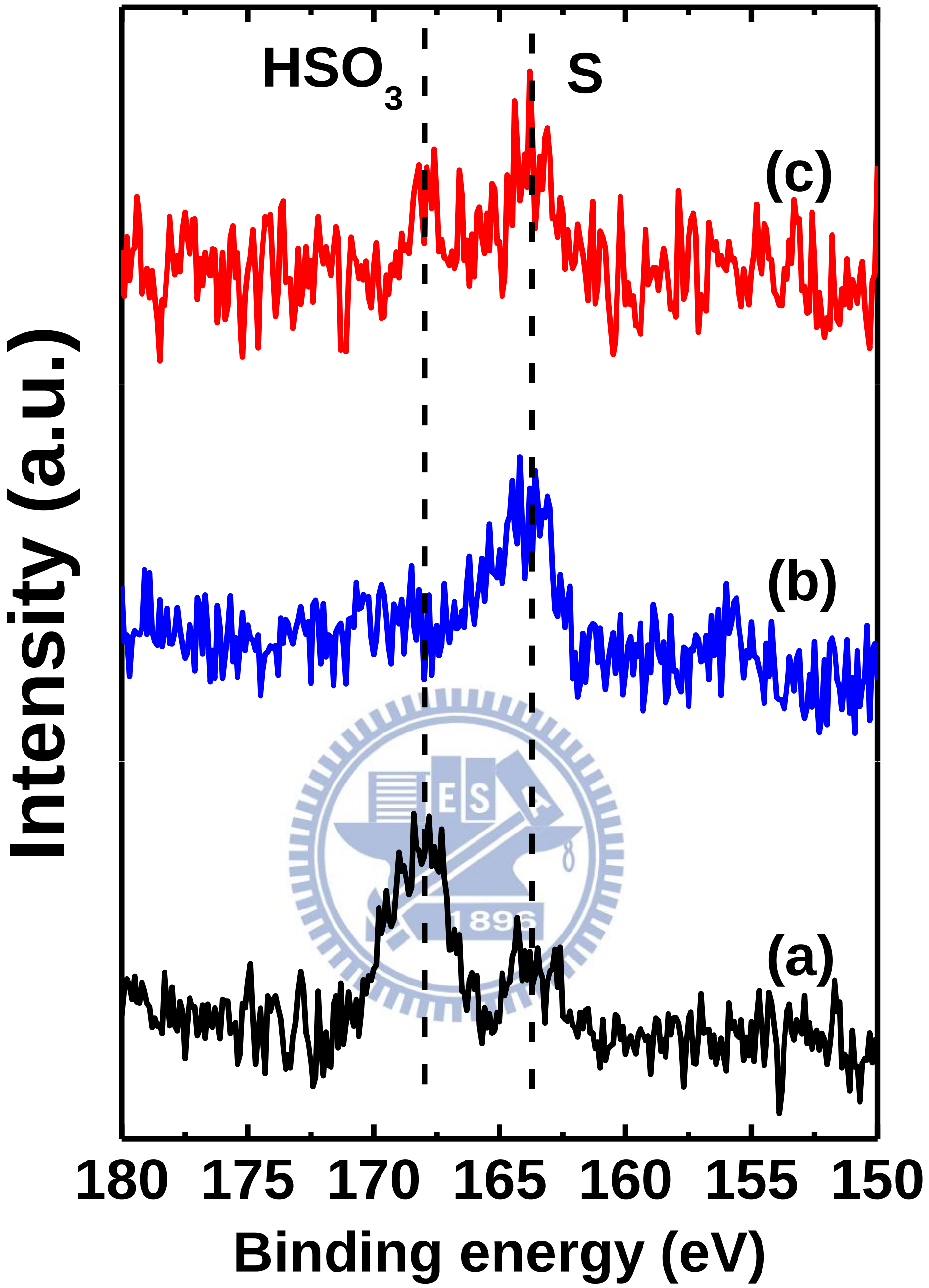

Figure 5.11. S2p XPS profiles for (a) as-prepared electrode (carbon cloth/XC-72R/Nafion ionomer), as well as electrodes (carbon cloth/XC-72R) (b) before and (c) after immersion in HCl solution containing concentrated residues from Nafion ionomer decomposition.

Table 5.3. The atomic ratios for C−C, −OH, −C=O, −COOH, and C−F from C1s XPS curve fitting for as-prepared electrode, as well as electrodes made of XC-72R/carbon cloth with and without immersion in HCl solution containing concentrated residues from Nafion ionomer decomposition.

	C−C (at%) (backbone)	−OH (at%) (a)	−C=O (at%) (b)	−COOH (at%) (c)	C−F (at%)	(a+b+c)/C−C
as-prepared	63.7	14	6.3	5.7	10.3	40.8 %
XC-72R/carbon cloth without immersion	63.7	17.2	8.3	7	3.8	51 %
XC-72R/carbon cloth with immersion	46.5	11.6	8.2	27.9	5.8	102.5 %

5.3.3 Methanol electro-oxidation

Fig. 5.12(a) demonstrates the TEM image for Pt nanoparticles deposited on the functionalized electrode followed by electrochemical reduction. As shown, there were plenty Pt nanoparticles uniformly distributed with notable aggregations. The primary particle size from the image analysis software was 2.68±1.62 nm. The TEM image on the reference sample (simple H_2SO_4 immersion followed by electrochemical reduction) is presented in Fig. 5.12(b). Apparently, the amount of Pt nanoparticles was substantially reduced, a fact consistent with earlier findings from ICP-MS. In addition, their size was slightly smaller at 2.20±1.45 nm. These results confirmed that the functionalized electrode enabled a larger amount of Pt deposits, albeit with moderate coalescence.

Fig. 5.13 presents the CV profiles of hydrogen desorption and adsorption for the functionalized and reference electrodes, respectively. As expected, there appeared stronger responses in hydrogen desorption and adsorption for the functionalized electrode because of its relatively larger amount of Pt deposit. Estimation on the ECSA was conducted by the integral area for hydrogen desorption in the anodic scan and the resulting ECSA values were 82.2 and 60.9 cm^2 for the functionalized and reference electrodes, respectively. This ratio of 1.35 was smaller to that of 1.70 for the Pt loading from ICP-MS. We attributed the reduced ESCA ratio to the observed Pt aggregation on the functionalized electrode.

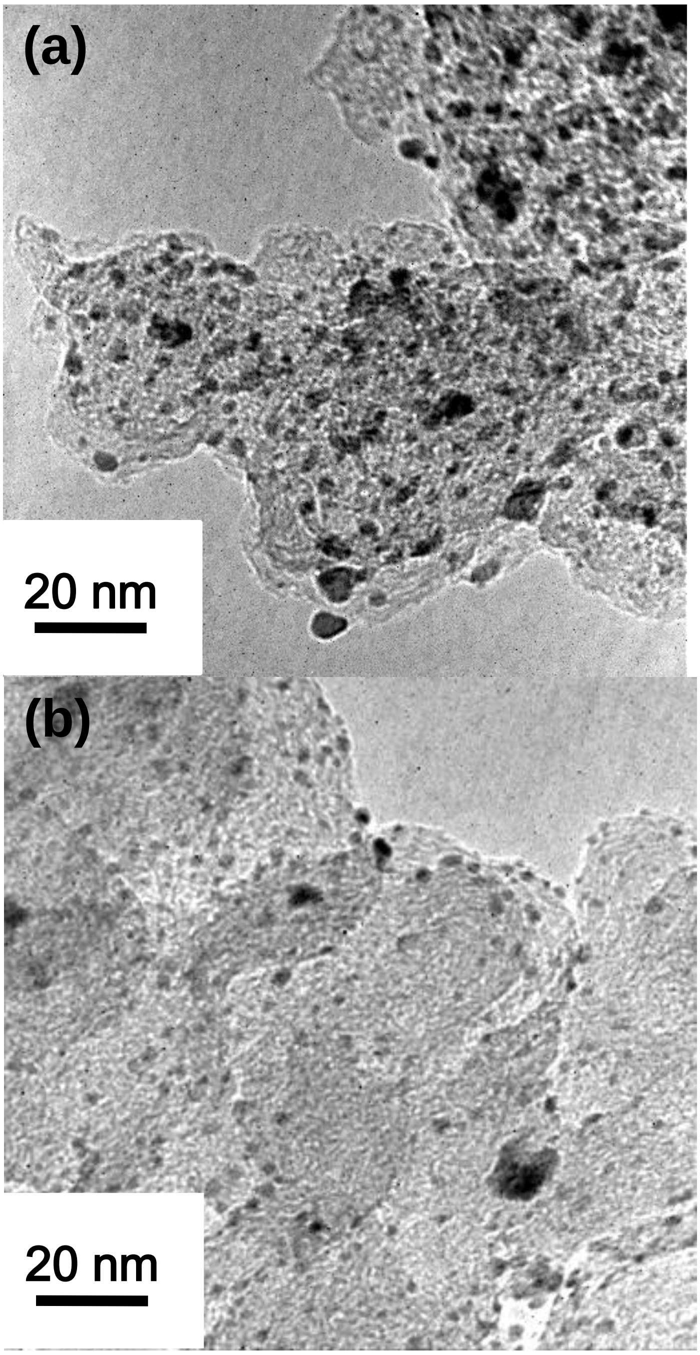

Figure 5.12. TEM images for deposited Pt nanoparticles on (a) functionalized and (b) baseline electrodes.

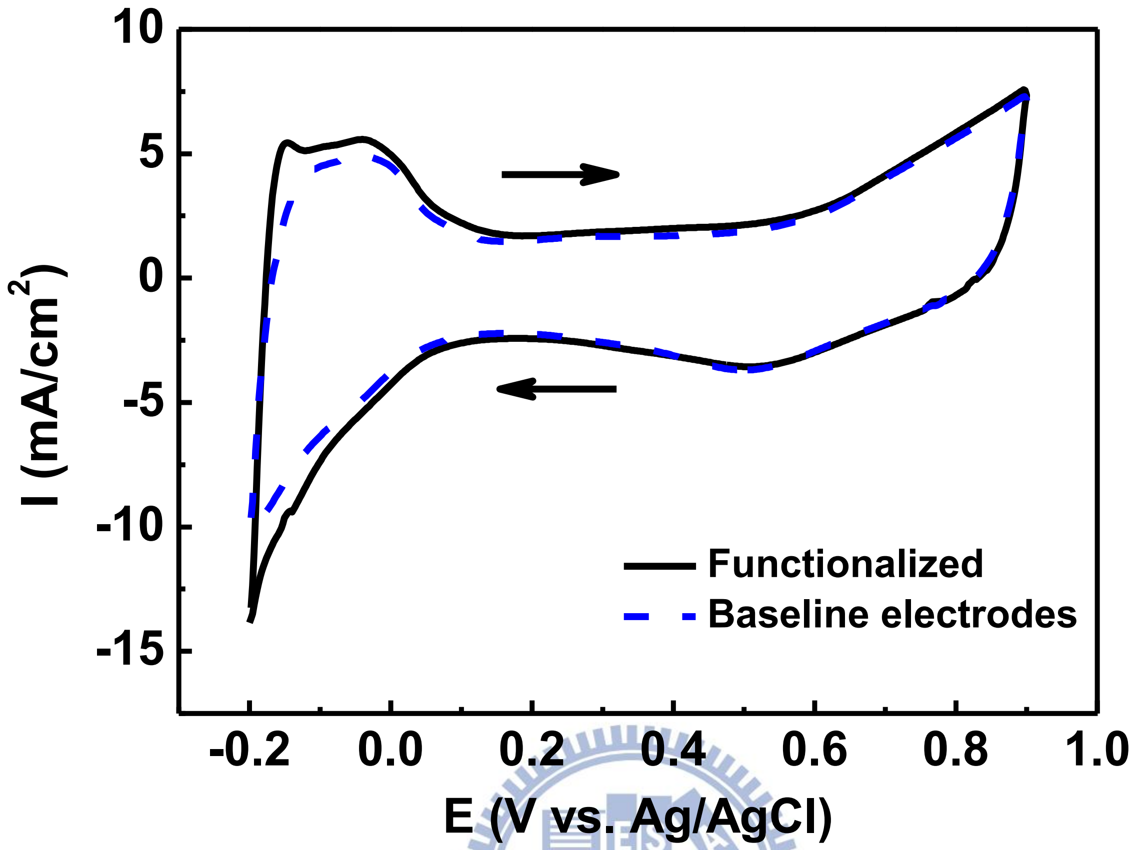

Figure 5.13. ECSA profiles for functionalized and baseline electrodes.

Fig. 5.14(a) provides the CV profiles for methanol electro-oxidation in apparent current density for the functionalized and reference electrodes, respectively. Relevant electrochemical parameters from these curves are listed in Table 5.4. According to literature, in these profiles the anodic peak (i_a) is attributed to the oxidation of methanol while the cathodic peak (i_c) corresponds to the oxidation of carbonaceous species produced from earlier methanol oxidation.[41, 86, 164] In addition, the ratio (i_a/i_c) indicates the electrocatalytic ability to remove CO. Hence, an electrode with a higher apparent current and a larger i_a/i_c ratio is always desirable. Notably, the functionalized electrode demonstrated a substantial current increment over that of reference electrode. This notable improvement was partially caused by a larger Pt deposits which lead to higher nominal current. Therefore, to compare fairly it is necessary to replot the CV profiles in mass activity and unit Pt ECSA, as shown in Fig. 5.14(b) and Fig. 5.14(c). Apparently, there appeared a consistent trend in which the functionalized electrode revealed significant enhancements over that of reference sample but their i_a/i_c ratios remained relatively unchanged. These results suggested that the oxygenated functional groups were likely contributing to the methanol electro-oxidation. Similar phenomena were also reported previously in which the oxidized functional groups were believed to provide oxygen-rich species to facilitate CO oxidation on Pt surface.[151, 165, 166]

After confirming enhancements in CVs for the functionalized electrode, it is necessary to evaluate its chronoamperogram for lifetime determination. Fig. 5.15 provides the chronoamperograms for the functionalized and baseline electrodes at 0.5 V for 30 min in mass activity. Apparently, both electrodes displayed a notable current decay in the first 20 min. However, the amount of current decay was relatively constant for both electrodes and the functionalized electrode was consistently better than the baseline electrode. Since the Pt was used in our study, these performance degradations were not unexpected as poisonous intermediates were able to adsorb on the Pt surface compromising its catalytic ability for methanol oxidation. It is noted that similar behaviors were also observed by Ma et al. in their study of Pt–Ru$(O_xH_y)_m$ electrocatalysts.[167]

Table 5.4. Electrochemical parameters obtained from CV profiles on functionalized and reference electrodes for methanol electro-oxidation.

		Anodic scan				Cathodic scan			
	Pt[a] Loading µg/cm^2	V_a[b]	i_a[c]	i_a[d]	i_a[e]	V_c[f]	i_c[g]	i_c[h]	i_c[i]
		mV	mA/cm^2	mA/ mg$_{Pt}$	mA/cm$^2_{Pt}$	mV	mA/cm^2	mA/ mg$_{Pt}$	mA/cm$^2_{Pt}$
Functionalized electrode	511	729	38.9	76.1	0.47	502	43.7	85.5	0.53
Reference electrode	301	677	20.4	67.7	0.33	428	19.7	65.4	0.32

[a] total weight of Pt as determined by ICP-MS

[b] peak potential in anodic scan

[c] peak apparent current density in anodic scan

[d] peak mass activity in anodic scan

[e] peak Pt surface activity in anodic scan

[f] peak potential in cathodic scan

[g] peak apparent current density in cathodic scan

[h] peak mass activity in cathodic scan

[i] peak Pt surface activity in cathodic scan

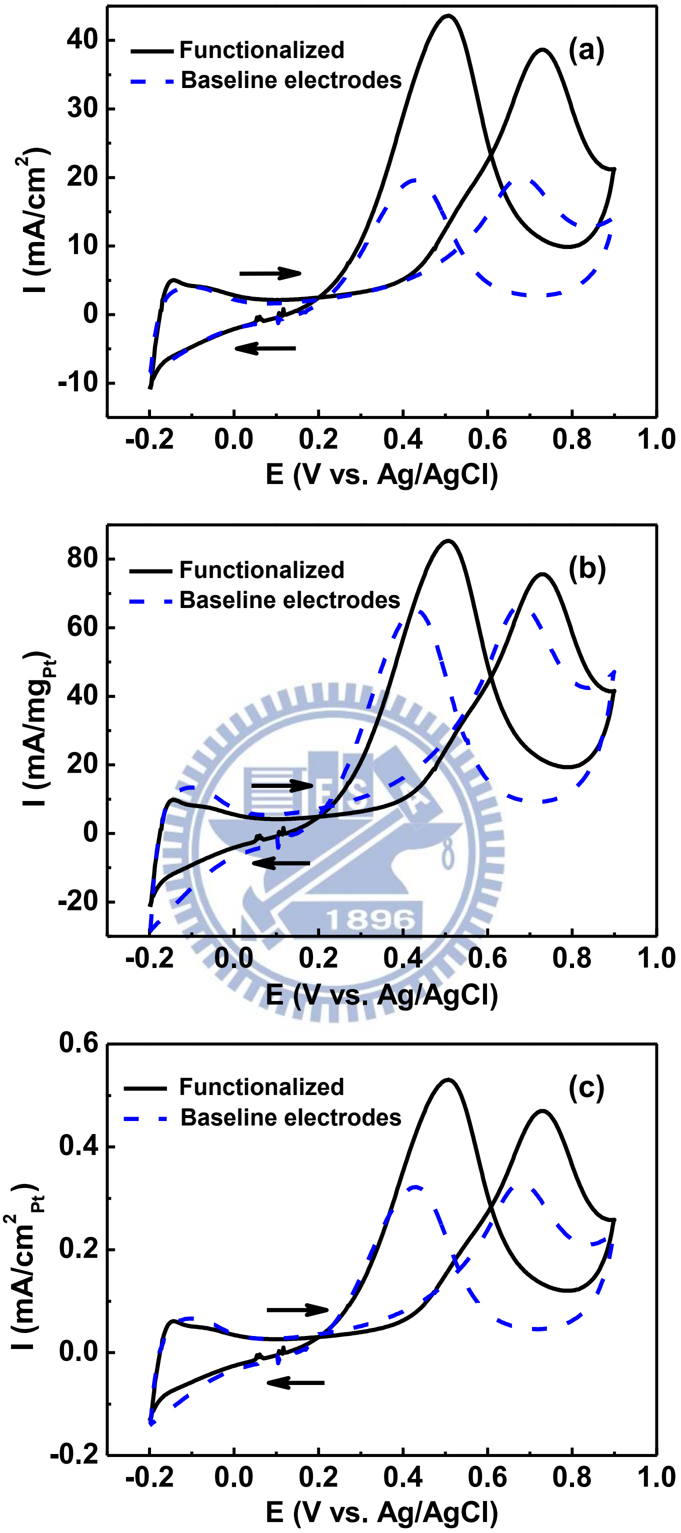

Figure 5.14. CV profiles for functionalized and baseline electrodes on methanol electrooxidation in (a) apparent current density, (b) mass activity, and (c) unit Pt electrochemical surface area.

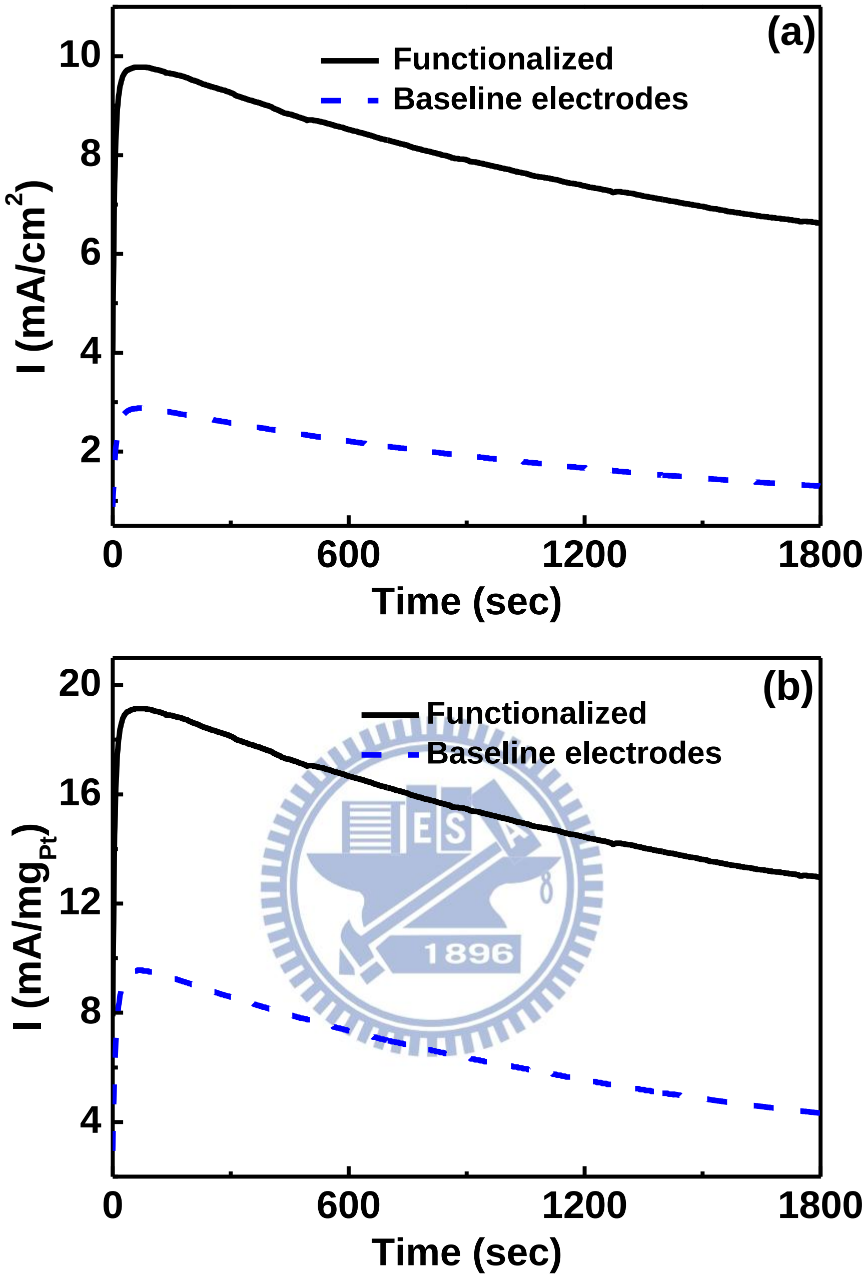

Figure 5.15. Chronoamperograms for functionalized and baseline electrodes on methanol electro-oxidation at 0.5 V for 30 min in mass activity.

So far, our work demonstrates a facile approach to functionalize catalyst supports without involving high temperature and large anodic potentials. Since the Nafion ionomer itself is often used as a binder in electrode fabrication, a simple CV with dissolved oxygen nearby could decompose the Nafion ionomer partially resulting in the formation of oxygenated functional groups. These functional groups are active in assisting the Pt for methanol electro-oxidation. It is noted that the enhancement effect observed in this work is different from conventional approaches in which the role of Nafion ionomer is to extend the interfacial area between the Nafion ionomer and electrocatalyst.[168] Moreover, the functional groups could potentially enable a larger electrocatalyst impregnation leading to an improved stability.[169] Further studies are under way to explore the anchoring effect for the functionalized groups and life time performances of supported Pt electrocatalyst.

5.4 Conclusions

We conducted multiple CV scans in an acidic electrolyte on the electrodes containing carbon cloth, XC-72R, and Nafion ionomer. With the supply of ambient oxygen, the Nafion ionomer experienced chemical attacks leaving decomposed residues which were able to adsorb onto the carbon surface leading to an accelerated formation of oxygenated functional groups. The decomposition of Nafion ionomer was attributed to the hydrogen peroxide produced from the oxygen reduction reaction during CV scans. Raman analysis on the carbon electrodes revealed minor structural modification after CV scans. Results from XPS surveys indicated a substantial significant increase of the oxygenated functional groups on the carbon surface in conjunction with a notable reduction in fluorine content. The functionalized electrode was determined to allow a larger amount of Pt ion adsorption as compared to the reference sample. After electrochemical reduction, the Pt nanoparticles were evenly formed on the carbon supports. Electrochemical analysis on the methanol electro-oxidation was performed and we observed significant increments in apparent current density, mass activity, as well as unit Pt ESCA for the functionalized electrode.

Chapter 6 Conclusion and Future Work

6.1 Conclusions

We have enhanced performances for the methanol electro-oxidation reaction (MOR) via the optimized PtRu nanostructured electrocatalysts with the desired atomic structure and surface composition controllable through the galvanic displacement reaction between Ru atoms and Pt ions. PtRu nanoparticles were prepared on carbon cloths by pulse current deposition in the aqueous electrolyte bath containing $RuCl_3$, H_2PtCl_6 and $NaNO_2$. During the time of current on (T_{on}), PtRu alloy nanoparticles were deposited on carbon cloths with a uniform size distribution; while during the time of current off (T_{off}), Ru atoms on particle surface were galvanically displaced by the excess $PtCl_6^{2-}$ ions in the electrolyte to yield the nanoparticle with a Pt-rich shell. The total metal loading, the surface composition and atomic distribution of Pt and Ru can be adjusted by the balance between T_{on} and T_{off}, i.e. by the duty cycle defined as $T_{on}/(T_{on}+ T_{off})$, in order to attain the optimized core-shell PtRu nanocatalysts for the enhanced MOR performances.

In addition, by the advanced mechanism investigation of galvanic displacement reaction between Ru atoms and Pt ions to form Ru-core Pt-shell nanoparticles, we have proven that the surface composition and the alloying degree of PtRu nanoparticles can be simply controlled and modified by the pH value of aqueous H_2PtCl_6 solutions in which Ru nanoparticles are immersed. The analyses from X-ray absorption near edge structure (XANES) and extended X-ray absorption fine structure (EXAFS) revealed that the pH value of H_2PtCl_6 solutions determined the type of ligands complexing the Pt cations and consequently led to different reaction stage of PtRu upon the galvanic displacement. The sample of Ru nanoparticles immersed in the pH=1 H_2PtCl_6 solution, with additional post treatment of hydrogen reduction, exhibited the desired Ru-core Pt-shell structure displaying a reduced onset potential in CO stripping measurements and stable catalytic activities for H_2 oxidation with a high CO-tolerance.

Furthermore, the MOR performances can be improved by the functionalization of carbon supports. Upon cyclic voltammetric scans in acidic electrolytes, carbon black (the common catalyst support) bound by Nafion ionomer (the common proton conductor used in fuel cells) acquires extra oxygen-containing (oxygenated) functional groups on its surface. This is attributed to the electrochemical degradation of Nafion ionomer. The functionalized carbon supports had a stronger adsorption and anchoring effect of metal precursors leading to a higher metal loading. Pt nanoparticles formed on the functionalized carbon supports were uniformly dispersed and exhibit significantly enhanced MOR performances.

In conclusion, we have demonstrated a promising way to enhance the MOR performances with a high CO-tolerance via both the atomic-level engineering of PtRu nanostructured electrocatalysts and the surface functionalization of carbon supports.

6.2 Future work

In this study, we have successfully employed the atomic-level structural engineering technique to develop core-shell PtRu nanocatalysts for the enhancement of methanol oxidation performances along with high CO tolerance. For the future work, we will continue employing this technique to control and optimize electrocatalysts’ structures and compositions toward the further enhancement of their catalytic performances toward various electrochemical reactions.

6.2.1 Development of electrocatalysts with different nanostructures by the advanced pulse electroplating

In the current study, we have employed only the simplest rectangular pulses in electroplating to fabricate core-shell structured nanoparticles. For the future work, we will use different types of pulse electroplating, such as the reversible pulse plating and the multi-step pulse plating. Also in this study, we have employed the same electrolyte as the electroplating bath. For the future work, we will change the composition and concentration of electrolytes as the electroplating bath.

By employing the advanced pulse electroplating, we will be capable to fabricate electrocatalysts with different core-shell nanostructures, such as the one-to-two monolayer shell, the island-like clusters as the shell, the inner shell and the outmost shell composed of different metals, and etc..

6.2.2 Development of electrocatalysts with different compositions for other catalytic reactions

In the current study, we have only synthesized the PtRu bimetallic electrocatalysts for the methanol oxidation reaction (MOR). However, many core-shell structured electrocatalysts composed of other metals have also been shown to exhibit improved catalytic activities for many other reactions. For example, Pt monolayer electrocatalysts supported on Pd nanoparticles displayed good catalytic activities for the oxygen reduction reaction (ORR).

For our future work, the pulse electroplating technique is suitable to develop electrocatalysts with various bimetallic or multi-metallic compositions for other electrocatalytic reactions, such as the oxygen reduction reaction (ORR), hydrogen oxidation reaction (HOR), hydrogen evolution reaction (HER), and so on.

In summary, we will further develop the advanced electroplating technique to synthesize various electrocatalysts with the expanded options of nanostructures, compositions and catalytic reactions.

Reference

[1] Steele BCH, Heinzel A. Materials for fuel-cell technologies. Nature. 2001;414(6861):345-52.

[2] Acres GJK. Recent advances in fuel cell technology and its applications. Journal of Power Sources. 2001;100(1-2):60-6.

[3] Alayoglu S, Nilekar AU, Mavrikakis M, Eichhorn B. Ru-Pt core-shell nanoparticles for preferential oxidation of carbon monoxide in hydrogen. Nat Mater. 2008;7(4):333-8.

[4] Sasaki K, Wang JX, Balasubramanian M, McBreen J, Uribe F, Adzic RR. Ultra-low platinum content fuel cell anode electrocatalyst with a long-term performance stability. Electrochimica Acta. 2004;49(22-23):3873-7.

[5] Ando Y, Sasaki K, Adzic R. Electrocatalysts for methanol oxidation with ultra low content of Pt and Ru. Electrochemistry Communications. 2009;11(6):1135-8.

[6] Zhang G, Sun S, Yang D, Dodelet J-P, Sacher E. The surface analytical characterization of carbon fibers functionalized by H2SO4/HNO3 treatment. Carbon. 2008;46(2):196-205.

[7] Kim JH, Fang B, Yoon SB, Yu J-S. Hollow core/mesoporous shell carbon capsule as an unique cathode catalyst support in direct methanol fuel cell. Appl Catal B-Environ. 2009;88(3-4):368-75.

[8] Oh SH, Sinkevitch RM. Carbon-Monoxide Removal from Hydrogen-Rich Fuel-Cell Feedstreams by Selective Catalytic-Oxidation. Journal of Catalysis. 1993;142(1):254-62.

[9] Nitani H, Nakagawa T, Daimon H, Kurobe Y, Ono T, Honda Y, et al. Methanol oxidation catalysis and substructure of PtRu bimetallic nanoparticles. Applied Catalysis A: General. 2007;326(2):194-201.

[10] Huang S-y, Chang S-m, Lin C-l, Chen C-h, Yeh C-t. Promotion of the electrochemical activity of a bimetallic platinum-ruthenium catalyst by oxidation-induced segregation. Journal of Physical Chemistry B. 2006;110(46):23300-5.

[11] Tsai M-C, Yeh T-K, Juang Z-Y, Tsai C-H. Physical and electrochemical characterization of platinum and platinum–ruthenium treated carbon nanotubes directly grown on carbon cloth. Carbon. 2007;45(2):383-9.

[12] Adzic RR, Zhang J, Sasaki K, Vukmirovic MB, Shao M, Wang JX, et al. Platinum monolayer fuel cell electrocatalysts. Topics in Catalysis. 2007;46(3-4):249-62.

[13] Hwang B-J, Sarma LS, Chen C-H, Bock C, Lai F-J, Chang S-H, et al. Controlled Synthesis and Characterization of Rucore−Ptshell Bimetallic Nanoparticles. The Journal of Physical Chemistry C. 2008;112(50):19922-9.

[14] Li M, Kowal A, Sasaki K, Marinkovic N, Su D, Korach E, et al. Ethanol oxidation on the ternary Pt–Rh–SnO2/C electrocatalysts with varied Pt:Rh:Sn ratios. Electrochimica Acta. 2010;55(14):4331-8.

[15] Zhou W-P, Sasaki K, Su D, Zhu Y, Wang JX, Adzic RR. Gram-Scale-Synthesized Pd2Co-Supported Pt Monolayer Electrocatalysts for Oxygen Reduction Reaction. Journal of Physical Chemistry C. 2010;114(19):8950-7.

[16] Che G, Lakshmi BB, Fisher ER, Martin CR. Carbon nanotubule membranes for electrochemical energy storage and production. Nature. 1998;393(6683):346-9.

[17] Guha A, Lu W, Zawodzinski Jr TA, Schiraldi DA. Surface-modified carbons as platinum catalyst support for PEM fuel cells. Carbon. 2007;45(7):1506-17.

[18] Chen C, Fuller TF. XPS Analysis of Polymer Membrane Degradation in PEMFCs. Journal of The Electrochemical Society. 2009;156(10):B1218-B24.

[19] Chen C, Levitin G, Hess DW, Fuller TF. XPS investigation of Nafion® membrane degradation. Journal of Power Sources. 2007;169(2):288-95.

[20] de Bruijn FA, Dam VAT, Janssen GJM. Durability and degradation issues of PEM fuel cell components. Fuel Cells. 2008;8(1):3-22.

[21] Hubner G, Roduner E. EPR investigation of HO. radical initiated degradation reactions of sulfonated aromatics as model compounds for fuel cell proton conducting membranes. Journal of Materials Chemistry. 1999;9(2):409-18.

[22] Boehm HP. Some Aspects of the Surface-Chemistry of Carbon-Blacks and Other Carbons. Carbon. 1994;32(5):759-69.

[23] Magagnin L, Maboudian R, Carraro C. Gold deposition by galvanic displacement on semiconductor surfaces: Effect of substrate on adhesion. Journal of Physical Chemistry B. 2002;106(2):401-7.

[24] Manandhar S, Kelber JA. Spontaneous deposition of Pt and Ir on Ru: Reduction to intermediate oxidation states. Electrochimica Acta. 2007;52(15):5010-7.

[25] Hwang B-J, Sarma LS, Chen C-H, Bock C, Lai F-J, Chang S-H, et al. Controlled Synthesis and Characterization of Ru-core-Pt-shell Bimetallic Nanoparticles. Journal of Physical Chemistry C. 2008;112(50):19922-9.

[26] Ren X, Zelenay P, Thomas S, Davey J, Gottesfeld S. Recent advances in direct methanol fuel cells at Los Alamos National Laboratory. Journal of Power Sources. 2000;86(1–2):111-6.

[27] Liu HS, Song CJ, Zhang L, Zhang JJ, Wang HJ, Wilkinson DP. A review of anode catalysis in the direct methanol fuel cell. Journal of Power Sources. 2006;155(2):95-110.

[28] Lamy C, Léger J-M, Srinivasan S. Direct Methanol Fuel Cells: From a Twentieth Century Electrochemist's Dream to a Twenty-first Century Emerging Technology
Modern Aspects of Electrochemistry. In: Bockris JOM, Conway BE, White RE, eds.: Springer US 2002, p. 53-118.

[29] Jusys Z, Massong H, Baltruschat H. A New Approach for Simultaneous DEMS and EQCM: Electro-oxidation of Adsorbed CO on Pt and Pt-Ru. Journal of The Electrochemical Society. 1999;146(3):1093-8.

[30] Zhu Y, Uchida H, Yajima T, Watanabe M. Attenuated Total Reflection−Fourier Transform Infrared Study of Methanol Oxidation on Sputtered Pt Film Electrode. Langmuir. 2000;17(1):146-54.

[31] Frelink T, Visscher W, Vanveen JAR. On the Role of Ru and Sn as Promoters of Methanol Electrooxidation over Pt. Surface Science. 1995;335(1-3):353-60.

[32] Richarz F, Wohlmann B, Vogel U, Hoffschulz H, Wandelt K. Surface and Electrochemical Characterization of Electrodeposited Ptru Alloys. Surface Science. 1995;335(1-3):361-71.

[33] Nashner MS, Frenkel AI, Somerville D, Hills CW, Shapley JR, Nuzzo RG. Core shell inversion during nucleation and growth of bimetallic Pt/Ru nanoparticles. Journal of the American Chemical Society. 1998;120(32):8093-101.

[34] Brankovic SR, Wang JX, Adzic RR. Pt submonolayers on Ru nanoparticles - A novel low Pt loading, high CO tolerance fuel cell electrocatalyst. Electrochemical and Solid State Letters. 2001;4(12):A217-A20.

[35] Green CL, Kucernak A. Determination of the platinum and ruthenium surface areas in platinum-ruthenium electrocatalysts by underpotential deposition of copper. 2. Effect of surface composition on activity. Journal of Physical Chemistry B. 2002;106(44):11446-56.

[36] Maillard F, Gloaguen F, Leger JM. Preparation of methanol oxidation electrocatalysts: ruthenium deposition on carbon-supported platinum nanoparticles. Journal of Applied Electrochemistry. 2003;33(1):1-8.

[37] Sasaki K, Mo Y, Wang JX, Balasubramanian M, Uribe F, McBreen J, et al. Pt submonolayers on metal nanoparticles—novel electrocatalysts for H2 oxidation and O2 reduction. Electrochimica Acta. 2003;48(25–26):3841-9.

[38] Coutanceau C, Rakotondrainibe AF, Lima A, Garnier E, Pronier S, Leger JM, et al.

Preparation of Pt-Ru bimetallic anodes by galvanostatic pulse electrodeposition: characterization and application to the direct methanol fuel cell. Journal of Applied Electrochemistry. 2004;34(1):61-6.
[39] Spinace E, Neto AO, Linardi M. Electro-oxidation of methanol and ethanol using PtRu/C electrocatalysts prepared by spontaneous deposition of platinum on carbon-supported ruthenium nanoparticles. Journal of Power Sources. 2004;129(2):121-6.
[40] Wei ZD, Chan SH. Electrochemical deposition of PtRu on an uncatalyzed carbon electrode for methanol electrooxidation. Journal of Electroanalytical Chemistry. 2004;569(1):23-33.
[41] Deivaraj TC, Lee JY. Preparation of carbon-supported PtRu nanoparticles for direct methanol fuel cell applications - a comparative study. Journal of Power Sources. 2005;142(1-2):43-9.
[42] Huang SY, Chang SM, Yeh CT. Characterization of surface composition of platinum and ruthenium nanoalloys dispersed on active carbon. Journal of Physical Chemistry B. 2006;110(1):234-9.
[43] Nitani H, Nakagawa T, Daimon H, Kurobe Y, Ono T, Honda Y, et al. Methanol oxidation catalysis and substructure of PtRu bimetallic nanoparticles. Applied Catalysis a-General. 2007;326(2):194-201.
[44] Yajima T, Uchida H, Watanabe M. In-Situ ATR-FTIR Spectroscopic Study of Electro-oxidation of Methanol and Adsorbed CO at Pt−Ru Alloy. The Journal of Physical Chemistry B. 2004;108(8):2654-9.
[45] Frelink T, Visscher W, van Veen JAR. On the role of Ru and Sn as promotors of methanol electro-oxidation over Pt. Surface Science. 1995;335(0):353-60.
[46] Huang S-H, Susanti D, Tsai D-S, Hsieh Y-C, Huang Y-S, Chung W-H. Structures and Catalytic Properties of PtRu Electrocatalysts Prepared via the Reduced RuO2 Nanorods Array. Langmuir. 2008;24(6):2785-91.
[47] Chen CH, Sarma LS, Wang DY, Lai FJ, Al Andra CC, Chang SH, et al. Platinum-Decorated Ruthenium Nanoparticles for Enhanced Methanol Electrooxidation. Chemcatchem. 2010;2(2):159-66.
[48] Zhang J, Mo Y, Vukmirovic MB, Klie R, Sasaki K, Adzic RR. Platinum monolayer electrocatalysts for O-2 reduction: Pt monolayer on Pd(111) and on carbon-supported Pd nanoparticles. J Phys Chem B. 2004;108(30):10955-64.
[49] Herrero E, Buller LJ, Abruña HD. Underpotential Deposition at Single Crystal Surfaces of Au, Pt, Ag and Other Materials. Chemical Reviews. 2001;101(7):1897-930.
[50] Lee JRI, O'Malley RL, O'Connell TJ, Vollmer A, Rayment T. X-ray Absorption Spectroscopy Characterization of Cu Underpotential Deposition on Au(111) and Organothiol-Self-Assembled-Monolayer-Modified Au(111) Electrodes from Sulfate Supporting Electrolyte. The Journal of Physical Chemistry C. 2009;113(28):12260-71.
[51] Sasaki K, Wang JX, Naohara H, Marinkovic N, More K, Inada H, et al. Recent advances in platinum monolayer electrocatalysts for oxygen reduction reaction: Scale-up synthesis, structure and activity of Pt shells on Pd cores. Electrochim Acta. 2010;55(8):2645-52.
[52] Sasaki K, Naohara H, Cai Y, Choi YM, Liu P, Vukmirovic MB, et al. Core-Protected Platinum Monolayer Shell High-Stability Electrocatalysts for Fuel-Cell Cathodes. Angew Chem Int Ed. 2010;49(46):8602-7.
[53] Zhang JL, Vukmirovic MB, Xu Y, Mavrikakis M, Adzic RR. Controlling the catalytic activity of platinum-monolayer electrocatalysts for oxygen reduction with different substrates. Angew Chem Int Edit. 2005;44(14):2132-5.
[54] Nilekar AU, Xu Y, Zhang JL, Vukmirovic MB, Sasaki K, Adzic RR, et al. Bimetallic and ternary alloys for improved oxygen reduction catalysis. Top Catal. 2007;46(3-4):276-84.
[55] Sasaki K, Mo Y, Wang JX, Balasubramanian M, Uribe F, McBreen J, et al. Pt submonolayers on metal nanoparticles - novel electrocatalysts for H-2 oxidation and O-2 reduction. Electrochim

Acta. 2003;48(25-26):3841-9.

[56] Tsai M-C, Yeh T-K, Tsai C-H. An improved electrodeposition technique for preparing platinum and platinum–ruthenium nanoparticles on carbon nanotubes directly grown on carbon cloth for methanol oxidation. Electrochemistry Communications. 2006;8(9):1445-52.

[57] Yu R, Chen L, Liu Q, Lin J, Tan K-L, Ng SC, et al. Platinum Deposition on Carbon Nanotubes via Chemical Modification. Chemistry of Materials. 1998;10(3):718-22.

[58] Chen J, Wang M, Liu B, Fan Z, Cui K, Kuang Y. Platinum Catalysts Prepared with Functional Carbon Nanotube Defects and Its Improved Catalytic Performance for Methanol Oxidation. The Journal of Physical Chemistry B. 2006;110(24):11775-9.

[59] Choi HC, Shim M, Bangsaruntip S, Dai H. Spontaneous Reduction of Metal Ions on the Sidewalls of Carbon Nanotubes. Journal of the American Chemical Society. 2002;124(31):9058-9.

[60] Chen C, Fuller TF. Modeling of H2O2 formation in PEMFCs. Electrochimica Acta. 2009;54(16):3984-95.

[61] Chen C, Fuller TF. The effect of humidity on the degradation of Nafion (R) membrane. Polymer Degradation and Stability. 2009;94(9):1436-47.

[62] Igarashi H, Fujino T, Zhu YM, Uchida H, Watanabe M. CO Tolerance of Pt alloy electrocatalysts for polymer electrolyte fuel cells and the detoxification mechanism. Physical Chemistry Chemical Physics. 2001;3(3):306-14.

[63] Strasser P, Fan Q, Devenney M, Weinberg WH, Liu P, Norskov JK. High throughput experimental and theoretical predictive screening of materials - A comparative study of search strategies for new fuel cell anode catalysts. Journal of Physical Chemistry B. 2003;107(40):11013-21.

[64] Whitacre JF, Valdez T, Narayanan SR. Investigation of Direct Methanol Fuel Cell Electrocatalysts Using a Robust Combinatorial Technique. Journal of The Electrochemical Society. 2005;152(9):A1780-A9.

[65] Petrii OA. Pt-Ru electrocatalysts for fuel cells: a representative review. Journal of Solid State Electrochemistry. 2008;12(5):609-42.

[66] Waszczuk P, Lu GQ, Wieckowski A, Lu C, Rice C, Masel RI. UHV and electrochemical studies of CO and methanol adsorbed at platinum/ruthenium surfaces, and reference to fuel cell catalysis. Electrochimica Acta. 2002;47(22-23):3637-52.

[67] Yajima T, Uchida H, Watanabe M. In-situ ATR-FTIR spectroscopic study of electro-oxidation of methanol and adsorbed CO at Pt-Ru alloy. Journal of Physical Chemistry B. 2004;108(8):2654-9.

[68] Choi JH, Park KW, Kwon BK, Sung YE. Methanol oxidation on Pt/Ru, Pt/Ni, and Pt/Ru/Ni anode electrocatalysts at different temperatures for DMFCs. Journal of The Electrochemical Society. 2003;150(7):A973-A8.

[69] Sieben JM, Duarte MME, Mayer CE. Supported Pt and Pt-Ru catalysts prepared by potentiostatic electrodeposition for methanol electrooxidation. Journal of Applied Electrochemistry. 2008;38(4):483-90.

[70] Alcaide F, Miguel Ó, Grande H-J. New approach to prepare Pt-based hydrogen diffusion anodes tolerant to CO for polymer electrolyte membrane fuel cells. Catalysis Today. 2006;116(3):408-14.

[71] Bauer A, Gyenge EL, Oloman CW. Direct methanol fuel cell with extended reaction zone anode: PtRu and PtRuMo supported on graphite felt. Journal of Power Sources. 2007;167(2):281-7.

[72] Kim SS, Nah YC, Noh YY, Jo J, Kim DY. Electrodeposited Pt for cost-efficient and flexible dye-sensitized solar cells. Electrochimica Acta. 2006;51(18):3814-9.

[73] Choi KH, Kim HS, Lee TH. Electrode fabrication for proton exchange membrane fuel cells by pulse electrodeposition. Journal of Power Sources. 1998;75(2):230-5.

[74] Lee J, Seo J, Han K, Kim H. Preparation of low Pt loading electrodes on Nafion (Na+)-bonded carbon layer with galvanostatic pulses for PEMFC application. Journal of Power Sources.

2006;163(1):349-56.

[75] Wei ZD, Chen SG, Liu Y, Sun CX, Shao ZG, Shen PK. Electrodepositing Pt by modulated pulse current on a nafion-bonded carbon substrate as an electrode for PEMFC. Journal of Physical Chemistry C. 2007;111(42):15456-63.

[76] Roy S, Matlosz M, Landolt D. Effect of Corrosion on the Composition of Pulse-Plated Cu-Ni Alloys. Journal of The Electrochemical Society. 1994;141(6):1509-17.

[77] Roy S, Landolt D. Effect of Off-Time on the Composition of Pulse-Plated Cu-Ni Alloys. Journal of The Electrochemical Society. 1995;142(9):3021-7.

[78] Zhu Q, Hussey CL. Galvanostatic pulse plating of Cu-Al alloy in a room-temperature chloroaluminate molten salt - Rotating ring-disk electrode studies. Journal of The Electrochemical Society. 2001;148(5):C395-C402.

[79] Porter LA, Choi HC, Ribbe AE, Buriak JM. Controlled electroless deposition of noble metal nanoparticle films on germanium surfaces. Nano Letters. 2002;2(10):1067-71.

[80] Zhang J, Lima FHB, Shao MH, Sasaki K, Wang JX, Hanson J, et al. Platinum monolayer on nonnoble metal-noble metal core-shell nanoparticle electrocatalysts for O-2 reduction. Journal of Physical Chemistry B. 2005;109(48):22701-4.

[81] Vukmirovic MB, Zhang J, Sasaki K, Nilekar AU, Uribe F, Mavrikakis M, et al. Platinum monolayer electrocatalysts for oxygen reduction. Electrochimica Acta. 2007;52(6):2257-63.

[82] Thambidurai C, Kim Y-G, Stickney JL. Electrodeposition of Ru by atomic layer deposition (ALD). Electrochimica Acta. 2008;53(21):6157-64.

[83] Brankovic SR, McBreen J, Adzic RR. Spontaneous deposition of Pt on the Ru(0001) surface. Journal of Electroanalytical Chemistry. 2001;503(1-2):99-104.

[84] Brankovic SR, Wang JX, Zhu Y, Sabatini R, McBreen J, Adzic RR. Electrosorption and catalytic properties of bare and Pt modified single crystal and nanostructured Ru surfaces. Journal of Electroanalytical Chemistry. 2002;524:231-41.

[85] Woods R. Hydrogen adsorption on platinum, iridium and rhodium electrodes at reduced temperatures and the determination of real surface area. Journal of Electroanalytical Chemistry and Interfacial Electrochemistry. 1974;49(2):217-26.

[86] Liu Z, Ling XY, Guo B, Hong L, Lee JY. Pt and PtRu nanoparticles deposited on single-wall carbon nanotubes for methanol electro-oxidation. Journal of Power Sources. 2007;167(2):272-80.

[87] Vigier F, Gloaguen F, Leger JM, Lamy C. Electrochemical and spontaneous deposition of ruthenium at platinum electrodes for methanol oxidation: an electrochemical quartz crystal microbalance study. Electrochimica Acta. 2001;46(28):4331-7.

[88] Gavrilov AN, Petrii OA, Mukovnin AA, Smirnova NV, Levchenko TV, Tsirlina GA. Pt-Ru electrodeposited on gold from chloride electrolytes. Electrochimica Acta. 2007;52(8):2775-84.

[89] Avtokratova TD. Analytical chemistry of ruthenium. Ann Arbor, MI Ann Arbor-Humphrey Science Publishers; 1963.

[90] Blake AJ, Gould RO, Johnson BFG, Parisini E. Na2[Ru(No2)4(No)(Oh)].2h2o - a Redetermination. Acta Crystallographica Section C-Crystal Structure Communications. 1992;48:982-4.

[91] Bennett JA, Show Y, Wang SH, Swain GM. Pulsed galvanostatic deposition of Pt particles on microcrystalline and nanocrystalline diamond thin-film electrodes I. Characterization of As-deposited metal/diamond surfaces. Journal of The Electrochemical Society. 2005;152(5):E184-E92.

[92] Antolini E, Cardellini F. Formation of carbon supported PtRu alloys: an XRD analysis. Journal of Alloys and Compounds. 2001;315(1-2):118-22.

[93] Spendelow JS, Wieckowski A. Noble metal decoration of single crystal platinum surfaces to create well-defined bimetallic electrocatalysts. Physical Chemistry Chemical Physics. 2004;6(22):5094-118.

[94] NIST X-ray Photoelectron Spectroscopy Database. Gaithersburg, MD: U.S. National Institute of Standards and Technology 2008.
[95] Lewera A, Zhou WP, Hunger R, Jaegermann W, Wieckowski A, Yockel S, et al. Core-level binding energy shifts in Pt-Ru nanoparticles: A puzzle resolved. Chemical Physics Letters. 2007;447(1-3):39-43.
[96] Chang KH, Hu CC. Oxidative synthesis of RuOx center dot nH(2)O with ideal capacitive characteristics for supercapacitors. Journal of The Electrochemical Society. 2004;151(7):A958-A64.
[97] Chen C-H, Sarma LS, Wang D-Y, Lai F-J, Al Andra C-C, Chang S-H, et al. Platinum-Decorated Ruthenium Nanoparticles for Enhanced Methanol Electrooxidation. Chemcatchem. 2010;2(2):159-66.
[98] Alayoglu S, Zavalij P, Eichhorn B, Wang Q, Frenkel AI, Chupas P. Structural and Architectural Evaluation of Bimetallic Nanoparticles: A Case Study of Pt−Ru Core−Shell and Alloy Nanoparticles. ACS Nano. 2009;3(10):3127-37.
[99] Hwang B-J, Sarma LS, Chen J-M, Chen C-H, Shih S-C, Wang G-R, et al. Structural Models and Atomic Distribution of Bimetallic Nanoparticles as Investigated by X-ray Absorption Spectroscopy. Journal of the American Chemical Society. 2005;127(31):11140-5.
[100] Lima FHB, Gonzalez ER. Electrocatalysis of ethanol oxidation on Pt monolayers deposited on carbon-supported Ru and Rh nanoparticles. Appl Catal B-Environ. 2008;79(4):341-6.
[101] Lee KR, Jeon MK, Woo SI. Composition optimization of PtRuM/C (M = Fe and Mo) catalysts for methanol electro-oxidation via combinatorial method. Appl Catal B-Environ. 2009;91(1-2):428-33.
[102] Manasilp A, Gulari E. Selective CO oxidation over Pt/alumina catalysts for fuel cell applications. Appl Catal B-Environ. 2002;37(1):17-25.
[103] Garcia-Rodriguez S, Somodi F, Borbath I, Margitfalvi JL, Antonio Pena M, Fierro JLG, et al. Controlled synthesis of Pt-Sn/C fuel cell catalysts with exclusive Sn-Pt interaction Application in CO and ethanol electrooxidation reactions. Appl Catal B-Environ. 2009;91(1-2):83-91.
[104] Lim D-H, Choi D-H, Lee W-D, Lee H-I. A new synthesis of a highly dispersed and CO tolerant PtSn/C electrocatalyst for low-temperature fuel cell; its electrocatalytic activity and long-term durability. Appl Catal B-Environ. 2009;89(3-4):484-93.
[105] Justin P, Charan PHK, Rao GR. High performance Pt-Nb2O5C electrocatalysts for methanol electrooxidation in acidic media. Appl Catal B-Environ. 2010;100(3-4):510-5.
[106] Kim HJ, Choi SM, Green S, Tompsett GA, Lee SH, Huber GW, et al. Highly active and stable PtRuSn/C catalyst for electrooxidations of ethylene glycol and glycerol. Appl Catal B-Environ. 2011;101(3-4):366-75.
[107] Desai S, Neurock M. A first principles analysis of CO oxidation over Pt and Pt66.7%Ru33.3% (111) surfaces. Electrochimica Acta. 2003;48(25-26):3759-73.
[108] Alayoglu S, Nilekar AU, Mavrikakis M, Eichhorn B. Ru-Pt core-shell nanoparticles for preferential oxidation of carbon monoxide in hydrogen. Nature Materials. 2008;7(4):333-8.
[109] McNicol BD, Short RT. The influence of activation conditions on the performance of platinum/ruthenium methanol electro-oxidation catalysts surface enrichment phenomena. Journal of Electroanalytical Chemistry and Interfacial Electrochemistry. 1977;81(2):249-60.
[110] Wang R, Li H, Feng H, Wang H, Lei Z. Preparation of carbon-supported core@shell PdCu@PtRu nanoparticles for methanol oxidation. Journal of Power Sources. 2010;195(4):1099-102.
[111] Zhao H, Li L, Yang J, Zhang Y. Co@Pt-Ru core-shell nanoparticles supported on multiwalled carbon nanotube for methanol oxidation. Electrochemistry Communications. 2008;10(10):1527-9.
[112] Kuk ST, Wieckowski A. Methanol electrooxidation on platinum spontaneously deposited on

unsupported and carbon-supported ruthenium nanoparticles. Journal of Power Sources. 2005;141(1):1-7.

[113] Hsieh Y-C, Wu P-W, Lu Y-J, Chang Y-M. Displacement Reaction in Pulse Current Deposition of PtRu for Methanol Electro-Oxidation. Journal of The Electrochemical Society. 2009;156(6):B735-B42.

[114] Spieker WA, Liu J, Miller JT, Kropf AJ, Regalbuto JR. An EXAFS study of the co-ordination chemistry of hydrogen hexachloroplatinate(IV) 1. Speciation in aqueous solution. Applied Catalysis a-General. 2002;232(1-2):219-35.

[115] Newville M. IFEFFIT: interactive XAFS analysis and FEFF fitting. Journal of Synchrotron Radiation. 2001;8:322-4.

[116] Ravel B, Newville M. ATHENA, ARTEMIS, HEPHAESTUS: data analysis for X-ray absorption spectroscopy using IFEFFIT. Journal of Synchrotron Radiation. 2005;12:537-41.

[117] Lee HY, Wu TB, Lee JF. X-ray absorption spectroscopic studies of sputter-deposited LaNiO3 thin films on Si substrate. Journal of Applied Physics. 1996;80(4):2175-80.

[118] Rehr JJ, Albers RC. Theoretical approaches to x-ray absorption fine structure. Reviews of Modern Physics. 2000;72(3):621-54.

[119] Park KW, Sung YE, Han S, Yun Y, Hyeon T. Origin of the enhanced catalytic activity of carbon nanocoil-supported PtRu alloy electrocatalysts. Journal of Physical Chemistry B. 2004;108(3):939-44.

[120] Yuan D, Tan S, Liu Y, Zeng J, Hu F, Wang X, et al. Pt supported on highly graphitized lace-like carbon for methanol electrooxidation. Carbon. 2008;46(3):531-6.

[121] Antolini E. Carbon supports for low-temperature fuel cell catalysts. Appl Catal B-Environ. 2009;88(1-2):1-24.

[122] Song S, Liang Y, Li Z, Wang Y, Fu R, Wu D, et al. Effect of pore morphology of mesoporous carbons on the electrocatalytic activity of Pt nanoparticles for fuel cell reactions. Appl Catal B-Environ. 2010;98(3-4):132-7.

[123] Michell D, Rand DAJ, Woods R. Study of Ruthenium Electrodes by Cyclic Voltammetry and X-Ray-Emission Spectroscopy. Journal of Electroanalytical Chemistry. 1978;89(1):11-27.

[124] Sugawara Y, Yadav AP, Nishikata A, Tsuru T. EQCM study on dissolution of ruthenium in sulfuric acid. Journal of The Electrochemical Society. 2008;155(9):B897-B902.

[125] Hu CC, Chiang HR, Wang CC. Electrochemical and structural investigations of oxide films anodically formed on ruthenium-plated titanium electrodes in sulfuric acid. Journal of Solid State Electrochemistry. 2003;7(8):477-84.

[126] Citrin PH, Wertheim GK. Photoemission from Surface-Atom Core Levels, Surface Densities of States, and Metal-Atom Clusters - a Unified Picture. Physical Review B. 1983;27(6):3176-200.

[127] Meitzner G, Via GH, Lytle FW, Sinfelt JH. Analysis of X-Ray Absorption-Edge Data on Metal-Catalysts. Journal of Physical Chemistry. 1992;96(12):4960-4.

[128] Dicks AL. The role of carbon in fuel cells. Journal of Power Sources. 2006;156(2):128-41.

[129] Baglio V, Di Blasi A, D'Urso C, Antonucci V, Arico AS, Ornelas R, et al. Development of Pt and Pt-Fe catalysts supported on multiwalled carbon nanotubes for oxygen reduction in direct methanol fuel cells. Journal of The Electrochemical Society. 2008;155(8):B829-B33.

[130]Hsu N-Y, Chien C-C, Jeng K-T. Characterization and enhancement of carbon nanotube-supported PtRu electrocatalyst for direct methanol fuel cell applications. Appl Catal B-Environ. 2008;84(1-2):196-203.

[131] Maass S, Finsterwalder F, Frank G, Hartmann R, Merten C. Carbon support oxidation in PEM fuel cell cathodes. Journal of Power Sources. 2008;176(2):444-51.

[132] Spataru N, Zhang X, Spataru T, Tryk DA, Fujishima A. Platinum electrodeposition on conductive diamond powder and its application to methanol oxidation in acidic media. Journal of The Electrochemical Society. 2008;155(3):B264-B9.

[133] Drillet J-F, Bueb H, Dittmeyer R, Dettlaff-Weglikowska U, Roth S. Efficient SWCNT-Based Anode for DMFC Applications. Journal of The Electrochemical Society. 2009;156(10):F137-F44.
[134] Guha A, Zawodzinski TA, Jr., Schiraldi DA. Influence of carbon support microstructure on the polarization behavior of a polymer electrolyte membrane fuel cell membrane electrode assemblies. Journal of Power Sources. 2010;195(16):5167-75.
[135] Lin JF, Kamavaram V, Kannan AM. Synthesis and characterization of carbon nanotubes supported platinum nanocatalyst for proton exchange membrane fuel cells. Journal of Power Sources. 2010;195(2):466-70.
[136] Saha MS, Kundu A. Functionalizing carbon nanotubes for proton exchange membrane fuel cells electrode. Journal of Power Sources. 2010;195(19):6255-61.
[137] Chang YM, Hsieh YC, Wu RW. Improved electrochemical performances by carbon nanocapsules as an electrocatalyst support for direct methanol fuel cells. Diamond and Related Materials. 2009;18(2-3):501-4.
[138] Hsieh Y-F, Hsieh Y-C, Wu P-W, Liao C-H, Chang Y-M. Pulse Electrodepositions of PtRu on Large-Area Carbon Nanotubes for Enhancement of Methanol Electro-Oxidation. Journal of The Electrochemical Society. 2010;157(1):B39-B44.
[139] Jafri RI, Arockiados T, Rajalakshmi N, Ramaprabhu S. Nanostructured Pt Dispersed on Graphene-Multiwalled Carbon Nanotube Hybrid Nanomaterials as Electrocatalyst for PEMFC. Journal of The Electrochemical Society. 2010;157(6):B874-B9.
[140] Liu B, Creager S. Carbon xerogels as Pt catalyst supports for polymer electrolyte membrane fuel-cell applications. Journal of Power Sources. 2010;195(7):1812-20.
[141] Salgado JRC, Alcaide F, Alvarez G, Calvillo L, Lazaro MJ, Pastor E. Pt-Ru electrocatalysts supported on ordered mesoporous carbon for direct methanol fuel cell. Journal of Power Sources. 2010;195(13):4022-9.
[142] Phompan W, Hansupalak N. Improvement of proton-exchange membrane fuel cell performance using platinum-loaded carbon black entrapped in crosslinked chitosan. Journal of Power Sources. 2011;196(1):147-52.
[143] Antonucci PL, Romeo F, Minutoli M, Alderucci E, Giordano N. Electrochemical Corrosion Behavior of Carbon-Black in Phosphoric-Acid. Carbon. 1988;26(2):197-203.
[144] Giordano N, Antonucci PL, Passalacqua E, Pino L, Arico AS, Kinoshita K. Relationship between Physicochemical Properties and Electrooxidation Behavior of Carbon Materials. Electrochimica Acta. 1991;36(13):1931-5.
[145] Passalacqua E, Antonucci PL, Vivaldi M, Patti A, Antonucci V, Giordano N, et al. The influence of Pt on the electrooxidation behaviour of carbon in phosphoric acid. Electrochimica Acta. 1992;37(15):2725-30.
[146] Pyun SI, Lee EJ, Kim TY, Lee SJ, Ryu YG, Kim CS. Role of Surface Oxides in Corrosion of Carbon-Black in Phosphoric-Acid Solution at Elevated-Temperature. Carbon. 1994;32(1):155-9.
[147] Puziy AM, Poddubnaya OI, Zaitsev VN, Konoplitska OP. Modeling of heavy metal ion binding by phosphoric acid activated carbon. Applied Surface Science. 2004;221(1-4):421-9.
[148] Yue ZR, Jiang W, Wang L, Gardner SD, Pittman CU. Surface characterization of electrochemically oxidized carbon fibers. Carbon. 1999;37(11):1785-96.
[149] Berenquer R, Marco-Lozar JP, Quijada C, Cazorla-Amoros D, Morallon E. Effect of electrochemical treatments on the surface chemistry of activated carbon. Carbon. 2009;47(4):1018-27.
[150] Kangasniemi KH, Condit DA, Jarvi TD. Characterization of vulcan electrochemically oxidized under simulated PEM fuel cell conditions. Journal of The Electrochemical Society. 2004;151(4):E125-E32.
[151] Stevanovic S, Panic V, Tripkovic D, Jovanovic VM. Promoting effect of carbon functional groups in methanol oxidation on supported Pt catalyst. Electrochemistry Communications.

2009;11(1):18-21.

[152] Wang J, Yin G, Shao Y, Zhang S, Wang Z, Gao Y. Effect of carbon black support corrosion on the durability of Pt/C catalyst. Journal of Power Sources. 2007;171(2):331-9.

[153] Chen C, Levitin G, Hess DW, Fuller TF. XPS investigation of Nafion (R) membrane degradation. Journal of Power Sources. 2007;169(2):288-95.

[154] Curtin DE, Lousenberg RD, Henry TJ, Tangeman PC, Tisack ME. Advanced materials for improved PEMFC performance and life. Journal of Power Sources. 2004;131(1-2):41-8.

[155] Schiraldi DA. Perfluorinated polymer electrolyte membrane durability. Polymer Reviews. 2006;46(3):315-27.

[156] Xie T, Hayden CA. A kinetic model for the chemical degradation of perfluorinated sulfonic acid ionomers: Weak end groups versus side chain cleavage. Polymer. 2007;48(19):5497-506.

[157] Bravo A, Bjorsvik HR, Fontana F, Liguori L, Mele A, Minisci F. New methods of free-radical perfluoroalkylation of aromatics and alkenes. Absolute rate constants and partial rate factors for the homolytic aromatic substitution by n-perfluorobutyl radical. Journal of Organic Chemistry. 1997;62(21):7128-36.

[158] Sansotera M, Bianchi CL, Lecardi G, Marchionni G, Metrangolo P, Resnati G, et al. Highly Hydrophobic Carbon Black Obtained by Covalent Linkage of Perfluorocarbon and Perfluoropolyether Chains on the Carbon Surface. Chemistry of Materials. 2009;21(19):4498-504.

[159] Morimoto T, Hiratsuka K, Sanada Y, Kurihara K. Electric double-layer capacitor using organic electrolyte. Journal of Power Sources. 1996;60(2):239-47.

[160] Hsieh CT, Teng H. Influence of oxygen treatment on electric double-layer capacitance of activated carbon fabrics. Carbon. 2002;40(5):667-74.

[161] Xie J, Wood DL, More KL, Atanassov P, Borup RL. Microstructural changes of membrane electrode assemblies during PEFC durability testing at high humidity conditions. Journal of The Electrochemical Society. 2005;152(5):A1011-A20.

[162] K. K. Oxygen electrochemistry. Electrochemical Oxygen Technology. New York: John Wiley & Sons 1992, p. 21–6.

[163] Teranishi K, Kawata K, Tsushima S, Hirai S. Degradation mechanism of PEMFC under open circuit operation. Electrochemical and Solid State Letters. 2006;9(10):A475-A7.

[164] Wang ZB, Yin GP, Zhang J, Sun YC, Shi PF. Co-catalytic effect of Ni in the methanol electro-oxidation on Pt-Ru/C catalyst for direct methanol fuel cell. Electrochimica Acta. 2006;51(26):5691-7.

[165] Chen JH, Wang MY, Liu B, Fan Z, Cui KZ, Kuang Y. Platinum Catalysts Prepared with Functional Carbon Nanotube Defects and Its Improved Catalytic Performance for Methanol Oxidation. Journal of Physical Chemistry B. 2006;110(24):11775-9.

[166] Scibioh MA, Oh I-H, Lim T-H, Hong S-A, Ha HY. Investigation of various ionomer-coated carbon supports for direct methanol fuel cell applications. Appl Catal B-Environ. 2008;77(3-4):373-85.

[167] Ma J-H, Feng Y-Y, Yu J, Zhao D, Wang A-J, Xu B-Q. Promotion by hydrous ruthenium oxide of platinum for methanol electro-oxidation. Journal of Catalysis. 2010;275(1):34-44.

[168] Park CH, Scibioh MA, Kim H-J, Oh I-H, Hong S-A, Ha HY. Modification of carbon support to enhance performance of direct methanol fuel cell. Journal of Power Sources. 2006;162(2):1023-8.

[169] Chen W, Xin Q, Sun G, Wang Q, Mao Q, Su H. The effect of carbon support treatment on the stability of Pt/C electrocatalysts. Journal of Power Sources. 2008;180(1):199-204.